MODIFICATION OF TURBULENT STRUCTURE IN CHANNEL FLOWS BY MICROBUBBLE INJECTION CLOSE TO THE WALL

A Dissertation

by

CLAUDIA DEL CARMEN GUTIERREZ TORRES

Submitted to the Office of Graduate Studies of
Texas A&M University
in partial fulfillment of the requirements for the degree of

DOCTOR OF PHILOSOPHY

August 2004

Major Subject: Mechanical Engineering

MODIFICATION OF TURBULENT STRUCTURE IN CHANNEL FLOWS BY MICROBUBBLE INJECTION CLOSE TO THE WALL

A Dissertation

by

CLAUDIA DEL CARMEN GUTIERREZ TORRES

Submitted to Texas A&M University
in partial fulfillment of the requirements
for the degree of

DOCTOR OF PHILOSOPHY

Approved as to style and content by:

Yassin A. Hassan (Co-Chair of Committee)	Nagamangala K. Anand (Co-Chair of Committee)
Denis Phares (Member)	Stuart L. Scott (Member)
Dennis L. O'Neal (Interim Head of Department)	

August 2004

Major Subject: Mechanical Engineering

ABSTRACT

Modification of Turbulent Structure in Channel Flows by Microbubble Injection Close to the Wall. (August 2004)

Claudia del Carmen Gutiérrez Torres, B.S., Acapulco Institute of Technology (Mexico);

M.S., National Polytechnic Institute (Mexico)

Co-Chairs of Advisory Committee: Dr. Yassin A. Hassan
Dr. Nagamangala K. Anand

An investigation of turbulent structure modification of a boundary layer for a fully developed channel flow by microbubble injection close to the upper wall was carried out using Particle Image Velocimetry (PIV). Two-dimensional velocity components in an x-y plane at Reynolds number of 5128 based on the half height of the channel and bulk velocity were measured. Microbubbles, with an average diameter of 30 μm were produced by electrolysis and injected in the buffer layer. Different values of the void fraction were attained and used to evaluate the effects of the presence of microbubbles and their concentration within the boundary layer.

A reduction in drag was observed due to the injection of microbubbles. Drag reduction augments as the value of the void fraction increases. Furthermore, increases in both the non-dimensional values of streamwise and normal turbulent intensities, normalized by the friction velocity were observed with the void fraction growth.

A gradual decrease in the Reynolds shear stresses was achieved as the void fraction increases. This effect is due to a “decorrelation” or “decoupling” between the streamwise and normal fluctuating velocities.

Modifications in the length and time scales due to the presence of microbubbles were detected by calculating two-point correlation coefficients in one and two dimensions and the autocorrelation coefficient at various locations within the measurement zone. Streamline length and time scales were increased. On the contrary, the normal length and time scales were decreased.

The vorticity and strain rate values decreased with the injection of microbubbles. Turbulent energy production was also decreased within the boundary layer.

Quadrant analysis was used to find out the contribution of the u’ and v’ fluctuating velocity components to the Reynolds stress. The presence of microbubbles reduces the contribution to the Reynolds stresses by Q_4 events (sweeps), which are responsible for the production of skin friction. Vortical structure detection in the measurement area was pursued. The structure with and without the microbubble injection is compared.

In this study the presence of microbubbles within the boundary layer has produced several modifications in the flow structure as well as reduction in the drag.

ACKNOWLEDGMENTS

I wish to express my gratitude to my advisor, committee Co-Chair, Dr. Yassin A. Hassan for his guidance, patience, knowledge and time throughout this entire project and to Dr. N. K. Anand, committee Co-Chair. I would also like to thank the committee members, Dr. Denis Phares and Dr. Stuart L. Scott.

Thanks to my friends and co-workers, Elvis E. Dominguez Ontiveros, Carlos E. Estrada Perez, Ling Zhen, and to my friend, Juan Gabriel Barbosa Saldaña.

Special thanks are due to my husband and fellow graduate student, Jose Alfredo Jimenez Bernal for his love, support, motivation and patience.

Thanks to my mother, Ma. Concepcion Torres Garcia, for her love and motivation during my whole life.

To my mother and my father in law, Ma. Asuncion Bernal Ortega and Tomas Jimenez Vazquez, thank you for your support.

Thanks to the National Polytechnic Institute of Mexico (Instituto Politécnico Nacional) for its support during my studies.

My doctoral studies were sponsored by the National Council of Science and Technology of Mexico (Consejo Nacional de Ciencia y Tecnología, CONACyT); without its support this would not have been possible.

NOMENCLATURE

A	Quantity being averaged
B	Universal constant
b	Point where the correlation coefficient becomes zero
C_f	Skin friction coefficient
C_f	Skin friction coefficient.
C_{fo}	Skin friction coefficient for pure water
d	Diameter of microbubbles
$\underline{\underline{D}}^{2-D}$	Two dimensional form of the velocity tensor
D_b	Bubble diameter
dP	Pressure drop
DR	Drag reduction
f	Fraction of the mean velocity
F	blowing rates
f	Forcing frequency
f^+	Forcing frequency in wall units
Fr	Froude number
g	Acceleration due to gravity
H	Threshold parameter for quadrant analysis
h	Half height of the channel
h_j	Conditioning function for quadrant analysis

I	Electrical current
I_I	Intensity
ℓ	Wall layer thickness or viscous length scale
L_{ij}	Integral length scale
$\dot{m}_H$	Hydrogen mass production
N	Total number of realizations
N_T	Number of velocity fields
P	Turbulent energy production
P	Pressure
Q_a	Air flow rate
Q_w	Water flow rate
$R(s)$	Autocorrelation of I(X)
R_b	Bubble radius
Re	Reynolds number
Re_τ	Reynolds number based of friction velocity
Re_θ	Reynolds number based on the free stream velocity and momentum thickness
Re_h	Reynolds number based on half height of the channel.
Re_i	Reynolds number associated with the injection velocity of the gas through the porous section
Re_x	Reynolds number based on the free stream velocity and distance x

$R_{ij}(\Delta r)$	Two-point correlation coefficient
$R_{ij}(\Delta t)$	Autocorrelation coefficient
s	Riblet spacing
s^+	Riblet spacing in wall units
S_{ij}	Average rate of strain
s_{ij}	Fluctuating rate of strain
S_j	Conditioning function for quadrant analysis using threshold parameter
t_τ	Viscous time scale
T_L	Integral time scale
U	Bulk velocity
u	Instantaneous streamwise velocity
U	Average or mean velocity
u_τ	Friction velocity
u’	Streamwise fluctuating velocity component
u’	Streamwise velocity fluctuation
u'_s	Fluctuating velocity from spatial decomposition
U_b	Bulk velocity
u_c	Velocity deviation
Uc	Convection velocity
U_e	Velocity at the free stream
u_{rms}	Streamwise turbulence intensity

U_s	Mean velocity obtained by spatial averaging
$-\overline{u'v'}$	Reynolds stresses
v’	Normal fluctuating velocity component
V_g	Gas volume
V_l	Liquid volume
v_{rms}	Normal turbulence intensity
V_w	Injection velocity at the wall
w	Atomic weight of the gas being liberated
We	Weber number
x	Distance
X_I	Center of the spot
$\overline{X}$	Position vector
x_j	Spatial coordinate in the jth direction
y+	Position in wall units
z	Valence number of the gas

Greek letters

ω	Vorticity
ν	Kinematic viscosity
λ	Eigen value

θ	Momentum thickness
α	Void fraction
σ	Surface tension
κ	Kármán constant
$\Delta\rho$	$\left(\rho_w - \rho_g\right)$
$\tau(X)$	Intensity transmissivity of the image
δ^*	Displacement thickness
δ_{99}	Boundary layer thickness
λ_{ci}	Swirling strength
τ_t	Total shear stress
τ_w	Wall shear stress

Superscript

‘	Fluctuation
-	Average or mean
+	Wall units

Subscript

g	Gas

i	Component
j	Component
l	Liquid
b	Bubble
z	Spanwise direction

TABLE OF CONTENTS

CHAPTER Page

LIST OF FIGURES

FIGURE Page

FIGURE Page

FIGURE Page

FIGURE Page

FIGURE Page

FIGURE Page

FIGURE Page

FIGURE Page

LIST OF TABLES

TABLE Page

CHAPTER I

INTRODUCTION

1.1 Motivation

An intensive investigation of methods to produce drag reduction in turbulent flows has been carried out for the past several decades. However, a consensus about the mechanism that governs this phenomenon has not been reached in spite of the efforts of several research groups.

A reduction in drag can decrease the energy consumption necessary for moving liquids or gases over solid walls (Fernholz *et al*. 1996). This effect can produce a broaden in range or increase in speed in almost any transportation system (commercial aircrafts, cargo ships, etc.) (Kim 2003); it can also augment the pipeline capacities (Larson 2003). All these outcomes will, in the end, result in fuel and energy savings resulting in less impact on environment and money savings.

From the research point of view, a close observation of the modifications that the different drag reduction methods produce within the boundary layer can help to shed some light on the mechanism that governs this phenomenon, and it is in itself an interesting scientific endeavor.

This dissertation follows the style and format of the *Journal of Fluid Mechanics.*

1.2 Drag Reduction Methods

Drag reduction in turbulent flows is a complex phenomenon which cannot simply be explained by mere suppression of turbulence (Gasljevic and Matthys 1999). An extensive research on several different techniques has been carried out in order to not only obtain better drag reduction results, but also gain a better understanding of the effects of these methods have on the boundary layer. A review of several studies on drag reduction by polymers, suction and blowing, transverse motions and microbubbles injection within the boundary layer is presented below.

1.2.1 Polymers

Drag reduction by polymer injection was discovered accidentally by Toms in 1946 (Toms 1977). The study was done with dilute solutions of high molecular weight polymethyl methacrylate in monochlorobenzene. The flow apparatus consisted of a horizontal tube with a reservoir at each end which could be immersed in a water bath kept at constant temperature. Two liters of polymer solution were used and each reservoir was about half-full when the air pressure was the same in both. Movement of the solution through the flow tube was achieved pneumatically by reducing the air pressure in one jar while the pressure in the other remained atmospheric. The time required for one liter of solution to pass through the tube under a known pressure (showed by a mercury U-tube manometer) was measured. It was observed that a

polymer solution offered less resistance to flow under constant pressure than the solvent itself.

An analysis of drag reduction in turbulent flow of viscoelastic polymer solution that utilizes only the viscous properties of the fluid in a pipe was performed by Kozicki and Tiu (1968). They concluded that drag reduction observed with viscoelastic non-Newtonian fluids can be attributed mainly to an increased laminar sub-layer thickness at the wall. It was suggested that this increased thickness was a manifestation of eddy suppression due to the mechanical resistance associated with preferred orientations and alignment of the polymer molecules in high shear fields.

The influence of drag-reducing polymers on the time-averaged velocity gradient and two components of the fluctuating velocity gradient at the wall were studied for turbulent flow in a 1 in. pipe by Fortuna and Hanratty (1972). They found that the changes in the intensity of the axial velocity fluctuations and the changes in the shape of the spectral density functions are not as great as the decrease of the skin friction coefficient. The transverse velocity fluctuations showed a significant decrease with increased drag reduction but the most significant change in turbulence structure appeared to be associated with the transverse (z-direction) correlation coefficient, where an increase can be observed as the drag reduction is increased.

Virk (1975) presented an extensive review about drag reduction by additives. Some of the most important remarks presented in this work are related to the physical mechanism of the drag reduction phenomenon. It was pointed out that the polymer-turbulence interaction responsible for drag reduction appears to commence in the

vicinity $y^+ \cong 15$ of the plane of peak turbulence production. This suggests that the polymer molecules interfere with the turbulent bursting process.

Some effects of the polymer addition in a fluid were discussed by Lumley (1977). It was suggested that the addition of polymers affects only the dissipative scales of the turbulence, suppressing the dissipative eddies, and increasing the scale of dissipation. This seems to be especially important in the buffer layer, where the scales of the dissipative and energy containing eddies are roughly the same, the energy containing eddies will be suppressed, resulting in reduced momentum transport, and effectively thickened viscous sublayer and a reduction of drag.

The effects of the addition of dilute polymer solutions were reported by Gyr (1977) for two visualization experiments carried out using water and dilute polymer solutions. A thickening of the viscous sublayer and of the buffer layer was observed. An increase in the formation of transverse vortices caused a stabilization of the shear waves in the direction of the flow. It was proposed that the drag reduction is the result of a higher alignment of the wall near separation vortices. Such stabilization of the local pattern would produce a higher number of enrolled vortices, which means more elements of larger coherent motion. At the same time, it causes a reduction of the chaotic redistribution in the velocity field. This hypothesis is said to be in good agreement with the observation of higher turbulent intensity of the streamwise velocity in the buffer zone.

Hanratty et al (1977) carried out experiments in two different loops designed to provide a fully developed flow in a pipe. One loop had a test section with a diameter of

19.34 cm, the other one had a diameter of 2.54 cm. They used an electrochemical technique which is the mass transfer analog of the hot film anemometer. Their results showed that drag reduction is accompanied by a decrease in the frequency and magnitude and an increase in the scale of the velocity fluctuations. Another change observed with the addition of drag reducing polymers was in the spatial correlation coefficients and turbulent scales. There is an increase in the ratio of the lateral scales of drag reduction and Newtonial fluids with increasing drag reduction.

High-resolution measurements made in turbulent channel flows with drag-reducing polymer additives are reported by Wei and Willmarth in 1992. Experiments were carried out in a fully developed channel flow with and without the injection of polyethylene oxide using two-component LDA measurement technique. The concentration of the polymer solution was 10 p.p.m. The experiments were performed at a Reynolds number of 12,000. It was found a dramatic attenuation of the v-velocity fluctuation as well as of the Reynolds stresses throughout the channel. There is a notorious change in the u-velocity spectra and the Reynolds stresses in the region near the wall when the same amount of polymer in a solution of three different concentrations is injected into the flow before it enters the channel.

Den Toonder *et al*. (1997) conducted a Direct Numerical Simulation (DNS) study of turbulent pipe flow. The effect of polymer additives was modeled with a simplified constitutive equation that introduces a viscous anisotropic stress. For computational purposes, the polymers are represented as elongated particles aligned with the instantaneous flow vector. DNS results showed a significant drag reduction, which

increased as the non-Newtonian parameter of the proposed model increased. The peak of the turbulent intensities for the axial (streamwise) velocity is increased and shifted away from the wall as drag reduction increases. On the other hand, the turbulent intensities for the other directions are decreased. All these effects were attributed to a purely viscous anisotropic stress introduced by extended polymers. It was also suggested that polymers elastic behavior reduces the drag-reducing effectiveness of the addition of polymers.

Gaslevic and Matthys (1999) compared the use of the usual drag and heat transfer reduction parameters with turbulence reduction parameters for drag-reducing flows using surfactants. They argued that the turbulence reduction parameters quantify the relative degree of turbulent effects reduction or “laminarization” exhibited by the drag-reducing fluid, rather than the “absolute” friction or heat transfer reduction. The advantage of the method proposed relied on the independence of the turbulence reduction parameters in relation with the Reynolds number. It was also pointed out the importance of the use of an appropriate apparent viscosity when calculating the Reynolds and Prandtl numbers for drag-reducing solutions.

Particle Image Velocimetry was used by Warholic *et al*. in 2001 to study the effect of drag-reducing polymers on the structure of turbulence in a channel flow. Measurements were carried out in the x-y plane and in the x-z plane. The experiments were performed for fully developed flow in a channel with a cross section of 5.08 cm x 61.0 cm. A solution of a copolymer of polyacylamide and sodium acrylate (Percol 727) was used. Drag reduction was defined as the ratio of the wall shear stress (determined by measuring the pressure drop and using a force balance in the streamwise direction) to

that obtained for water flowing at the same volumetric flow rate. The concentration used for the polymer solution was 500 ppm. It was observed an increase in the turbulent intensity for the streamwise component of the velocity. On the other hand, dramatic decreases in the velocity fluctuations normal to the wall and in the Reynolds shear stresses were found. A notable difference between turbulence structures of Newtonian fluids and of polymer solutions with high drag reduction is the reduction of small scale fluctuations, evidenced by decreases in swirling motions and the contributions of high wave numbers to the spectral functions. There is a decrease in the activity of the wall in creating turbulence at high drag reduction cases manifested by a decrease of ejections (bursts) from the wall.

A double pulse PIV system was used by Kawaguchi and Feng (2001) to clarify the spatial velocity distribution of surfactant solution flow in a two-dimensional channel of height 40 mm, width 500 mm and length 6 m. Instantaneous velocity fields were taken in the x-y plane using PIV and examined to clarify the effect of surfactant additives in a channel flow at Reynolds numbers 6,200, 10,000, 21,000, 42,000 and 62,000, where the Reynolds number was calculated using the bulk velocity and the channel height . It was found that the instantaneous velocity distribution for water flow without additives is different from the drag-reducing flows, showing a reduction in the random vortex motion for the drag-reducing flow. It was also observed that for the water flow there is penetration from low speed fluid into high-speed region (ejection or burst), this was not found in the drag reduction flow. A de-correlation of turbulence velocity components in

drag-reducing flows was also observed, which provides an explanation for the decrease of the Reynolds stresses.

De Angelis *et al.* (2002) carried out a DNS simulation using a FENE-P model for the polymers behavior. It was observed a widening of the streaks separation, related to a less dense population of streamwise vortices, located at a greater distance from the wall and weaker the corresponding Newtonian ones. There was a decrease in the wall normal fluctuations, attributed to their negative correlation with the corresponding component of the viscoelastic force. The streamwise turbulent intensity, in contrast, increased. This was associated with a larger turbulent transport term, explained by the alterations in the population of the streamwise vortices. The analysis of several instantaneous configurations indicates a substantial reduction of the turbulent activity in the wall region. The explanation offered for these modifications was that the viscoelastic force, by reducing the inhomogeneity in the field, promotes the stabilization of the sreaks and reduces the bursting rate, thus preventing most of the regeneration of streamwise vortices that would occur in presence of a pure Newtonian behavior.

Experiments in a closed loop fluid flow facility, consistent of a reservoir tank of 2 m^3, a pump, a settling chamber, a two-dimensional channel (40 mm high, 500 mm wide and 6 m long), a diffuser and an electro-magnetic flow meter were performed by Kawaguchi *et al*. (2002). A double pulse particle image velocimetry (PIV) system was used to clarify the spatial velocity distribution. A cationic surfactant cetyltrimethyl ammonioum chloride mixed with a counter-ion material NaSal was used as a drag-reducing additive to water at a mass concentration of 40 ppm. It was found that there is

a de-correlation of turbulence components in drag-reducing shear flow. The presence of inhomogeneous turbulence suppression was found. This means the normal fluctuating component is much suppressed than the streamwise fluctuating velocity component. This inhomogeneous suppression comes from the inhibition of energy transfer from u' to v' by large resistance eddy stretching. There is also a decrease in the presence of the strong vorticiy near the wall for drag-reducing flows.

The structure of turbulence in a drag-reducing flat-plate boundary layer flow with zero pressure gradient was studied by White *et al.* (2003) using PIV. In this study, drag reduction was achieved by injection of a concentrated polymer solution through a spanwise slot along the test wall at a location upstream of the measurement station. The measurements were carried out in a plane parallel to the wall (x-z), for 30 planes across the thickness of the boundary layer. The results indicate there is a significant modification of near-wall structure. With increasing drag reduction, there is an increase in the spanwise separation of the low-speed streaks and a reduction in the strength and numbers of the near-wall vortices.

1.2.2 Suction and Blowing

An experiment to test the concept of micro-blowing technique (MBT) was conducted by Hwang (1997). This technique consist of the blowing of an extremely small amount of air, in the vertical direction, through very small holes to reduce the surface roughness and to control the gradient of the flow velocity profile on the surface, reducing the skin friction and therefore the drag. Results showing a skin friction reduction in a range from

25 to 35% were obtained in the lower surface of a flat plate for a wide range of flow conditions. One of the principal parameters of the drag reduction by micro-blowing technique is the hole aspect ratio (thickness of the plate/ hole diameter). It was found that higher drag reduction was attained for cases where the hole aspect ratio was larger than 4.

The injection of an air film along the bottom of a hull to reduce skin friction drag was discussed by Latorre (1997). Results showed a performance improvement from adopting bottom air injection in high speed planing catamarans was presented. It was also found that bottom air injection on high speed planing catamarans resulted in a speed increase of 7-12 knots. Drag reduction of 10-12% was obtained by bottom air injection on full form barges and river cargo ships. The dependence of the drag reduction on the air flow injected Q_a to a certain level was established; however, above the threshold value there was not further decrease in drag.

The effects of localized injection through a porous strip on a turbulent layer at zero pressure gradient conditions were examined experimentally by Krogstad and Kourakine (2000). Experiments were performed in an open wind tunnel. The boundary layer investigated on the polished aluminum false floor of the working section that had a cross section of 0.46 x 0.46 m^2. The boundary layer was tripped at the leading edge by two sets of tripping devices consisting of 1 mm diameter rod followed by a 5 cm long strip of grit sandpaper. The free-stream turbulence was less than 0.5% and the roof was adjusted to produce zero pressure gradient flow conditions. The blowing section was installed 2.35 m downstream from the leading edge and consisted of a 0.12 m long porous strip

spanning the entire width of the test section. The strip was made of sintered stainless steel with and average hole diameter of 150 μm. Data was obtained for four blowing rates ($F= V_w/U_e$) 0, 0.0028, 0.0056 and 0.0086 (V_w is the injection velocity at the wall and U_e is the velocity at the free stream). The velocity was measured using hot wire anemometry. A decrease in the skin friction coefficient is significantly reduced over a region after the injection strip. However, the effects of the air injection can be observed for a significant distance downstream. The contributions to the shear stresses from the various quadrants (determined using quadrant analysis) were affected by the blowing. Contributions by the second quadrant (bursts or ejections) were reduced.

The effects of an oscillating localized blowing on near-wall turbulence were investigated by Tardu (2001). The imposed frequency is twice the ejection frequency of the inner layer, and the blowing amplitude is 5 wall units. The effects observed included a considerable decrease in the wall shear stress until it reaches a value equal to the one that would be found in a laminar boundary layer for the same Reynolds number. It was also observed that dissipation dominates the near-wall flow which is stabilized. The velocity fluctuations in the inner layer become inconsequential to the dynamics of the flow. Another finding is the decrease of the frequency of the active Reynolds-stress-producing events (bursts or ejections and sweeps). A very important finding is the strong decrease of the stretching of quasi-streamwise vorticity, this is indicated by negative values of the skewness of the streamwise velocity fluctuation time derivatives. However, the main effects of blowing are the displacement of the spanwise vorticity and the turbulent-drag-reducing quasi-streamwise vertical structures away from the wall.

The effect of periodic blowing and suction on a turbulent boundary layer was investigated by Park *et al.* (2003) using PIV. Experiments were carried out in a recirculating open water channel. A settling chamber, a honeycomb and a contraction were placed in sequence to secure flow homogeneity. The dimensions of the test section were 220 mm (width) x 250 mm (depth) x 1200 mm (length). A flat plate was installed 50 mm above the bottom wall of the test section. The boundary layer was tripped at the leading edge of the flat plate. PIV measurements were performed in an x-y plane. The local forcing (blowing and suction) was imposed through a spanwise thin slot. Three forcing frequencies $\left(f^+ = 0.044,\ 0.066 \text{ and } 0.088\right)$ were used at a Reynolds number of $Re_\theta = 690$; where $f^+ = f\nu/u_\tau^2$, f is the forcing frequency, ν is the kinematic viscosity and u_τ is the friction velocity. The results showed a reduction in the flow velocity in the vicinity of the wall due to the local forcing. Velocity retardation of the wall led to skin friction reduction. The degree to which the skin friction was reduced increased with forcing frequency. The maximum drag reduction was approximately 75% and was achieved at $f^+ = 0.088$.

1.2.3 Transverse Motion

A useful review of drag reduction in wall-bounded flows achieved by transverse motions was presented by Karniadakis and Choi (2003). In this work, a discussion of passive means (riblets) and external forcing methods (wall oscillations, transverse traveling-wave excitation, etc.) was presented.

Riblets are passive drag reduction devices, installed over smooth surface in the turbulent boundary layer. They can produce up to 10% drag reduction. Riblets consist of microgrooves of the size of the viscous sublayer that can have different geometries (triangular, semicircular, etc.). A reduction in the skin-friction drag can be obtained when the non-dimensional riblet spacing $s^+ = su_\tau/\nu$ is approximately 15. However, when the riblet spacing exceeds $s^+ = 30$ the drag starts to increase. These devices seem to work as longitudinal fences to reduce the skin-friction drag by impeding the spanwise movement of longitudinal vortices during sweep events. The reduction of drag by riblets is due to a modification of the sequence of the near-wall activity by passive spanwise forcing.

Another transverse motion method to achieve drag reduction is wall oscillation in the spanwise direction. A reduction in the mean velocity gradient at the boundary layer is produced by wall oscillation. This method regulates by a periodic oscillatory flow the behavior of longitudinal vortices in the near wall region. The result of this is that the streamwise vorticity fluctuation (with respect to phase-averaged values) near the wall is reduced by the spanwise wall oscillation, although it increases temporarily at the start of oscillation.

Transverse traveling wave excitation drag reduction technique has a different modification effect in the boundary layer. The effect of the action of the traveling wave, when drag reduction is achieved, is to weaken and in many cases to eliminate most of the wall streaks.

In general, for drag reduction by transverse motion the key mechanism identified is the control of the near-wall longitudinal vortices and the corresponding suppression of the instability of low-speed (sublayer) streaks.

1.2.4 Microbubble Injection

McCormick and Bhattacharyya (1973) presented a pioneer experimental work of drag reduction by electrolysis. They mounted a cathode to a hull (3-foot long body of revolution with a maximum diameter of 5 inch) and then created hydrogen bubbles beneath the boundary-layer by passing a current through the cathode. The hull was mounted to a force dynamometer which allowed measuring the drag force and towed along a tank at a constant mean depth. The cathode used was a copper wire of 6mm diameter. The hydrogen mass production was determined using Faraday's law of electrolysis, it was calculated using:

$$\dot{m}_H = 7.11x10^{-10}\left(\frac{Iw}{z}\right) \quad (1)$$

where I is the current in amperes, w is the atomic weight of the gas being liberated, and z is the valence number of the gas. For hydrogen w = 1.008 and z = +1.

It was found that the amount of drag reduction depends on the towing speed and the time-rate of hydrogen production. As the towing speed increased, the drag reduction

decreased. They attributed the drag reduction to the variation in viscosity near the hull. They also suggested that for a turbulent boundary layer, the hydrogen microbubbles disrupted the viscous sublayer, eliminating this high shear region. As the bubbles were convected away from the surface to the outer regions of the boundary layer, it was suggested that they reduced the Reynolds stresses by absorbing the momentum by their elasticity.

Bogdevich *et al.* (1977) performed experiments of saturation of bubbles in the turbulent boundary layer of a flat plate and in the initial section of a channel. Experiments with a plate were carried out in a cavitation tube with rectangular working section of 120 x 1000 mm. A plate was inserted in the working section; the plate had a rounded front edge of 955 mm long and 40 x 244 mm in the cross-section. The velocity of the flow velocity was equal to 4 – 11 m/s.

The experiments in the initial channel section were performed in a wind tube with an open 50 mm x 180 mm jet working section 1200 mm long. The flow velocity was 2 – 6 m/s. Bubbles were produced using insertions of porous materials flush-mounted with the stream-lined surface. Aluminium was used as a porous material with an average pore size of 2 μm. Measurements of surface friction were carried out using tensometric probes with floating surface elements, gas bubble concentration was measured by probes sensitive to the medium electrical conductivity, stream-lined surface pressure fluctuations were measured by a probe with a sensitive piezoceramics element 1.4 mm in diameter, gas flow rate and friction drag.

The obtained results showed a dependency on the value of the Reynolds number and the local friction. After increasing the Reynolds number above its critical values, it was observed that the efficiency of the gas saturation in reducing the drag is increased. When it happened, the local friction value approaches its calculational magnitude for a laminar flow in a homogeneous flow for the same Reynolds number. One of the most important parameters in this experiment is microbubble concentration in the boundary layer. In this case the higher concentration was found in the near wall region.

One of the early numerical simulations in drag reduction by microbubble injection was performed by Madavan *et al.* (1985). They used a simple mixing-length eddy-viscosity formulation, whose functional form is unchanged by the presence of bubbles. The effect of the bubbles on the boundary-layer characteristics are taken into account by allowing the viscosity and density to vary locally as a function of a prescribed bubble concentration profile. The results obtained indicated that the magnitude of skin-friction reduction depends upon the volumetric concentration of the bubbles, and also on their location and distribution within the boundary layer. The presence of bubbles in the viscous layer and the absence of bubbles in the buffer layer appeared to make the bubbles less effective.

In 1989 Merkle and Deutsh presented a review on the microbubble drag reduction phenomenon, experimental work done by themselves and other authors was analyzed. An illustrating report on the work carried out in the former USSR was also presented. The authors reported results obtained using flushed-mounted hot film probes for measurements of the shear stress. The experiments were performed in a constant-

pressure tunnel wall boundary layer in the two-dimensional (rectangular) test section of the 12-inch water tunnel. A second experiment was carried out in an axisymmetric body, mounted in the circular section of the 12-inch tunnel. A third experiment was performed in an upgraded installation similar to the one used in the first experiment with an improved optical access. The rectangular test section had dimensions of 508 mm x 114 mm and 762 mm long. The interchangeable circular section, used for the second experiment is 305 mm x 762 mm long. For any chosen configuration, the test section velocity can reach up to 20 m/sec and the pressure can be varied between 0.2 and 4 atmospheres.

The results obtained showed the following: the effect of the bubbles on the boundary layer had a strong dependence upon both their concentration and their location in the boundary layer. Microbubbles were more effective in the buffer layer. There was a growth of the viscous sublayer thickness when drag reduction was achieved. It was observed that the diameter of the bubbles played a significant role in the drag reduction phenomenon. It was suggested that if the bubbles were one order of magnitude larger than the viscous sublayer and one order of magnitude smaller than the boundary layer thickness, they were more effective.

Kato *et al.* (1994) conducted experiments in a water tunnel with a rectangular test section that has dimensions of 120 mm x 50 mm in cross-section. A circular rod of 5 mm diameter set on the tunnel wall 115 mm upstream of the test section acted as a turbulence stimulator. Velocity was measured by a laser-Doppler velocimeter.

A mixture of microbubbles and water was injected through a slit of 40 mm length and 0.6 mm width; the slit was oriented at an angle of 20° to the flat wall. The generation of microbubbles took place in an external device; clean water was pumped through an 8 mm diameter inner tube at a low rate (0.25 – 7 l/min). Compressed air was introduced to an outer annular chamber from which it could mix the injection water through 144 small holes of 0.5 mm diameter. The size of the bubbles produced ranged from 200 to 400 μm diameter.

The shear stress was measured using five shear-stress pick-ups installed on the flat wall of the test section. Each pick-up had a floating disk of 5 mm diameter with a capacity of 500 Pa. The main flow velocity was kept constant through the experiment at 8 m/s.

The results obtained from this experiment show that the position of the microbubbles within the boundary layer has a determinant role in the drag reduction phenomenon. The local maximum void fraction, α, defined as

$$\alpha = \frac{Q_a}{Q_a + Q_w} \tag{2}$$

where Q_a is the air flow rate and Q_w is the water flow rate, was pointed out as the governing parameter of the drag reduction rate. The importance of achieving a control of the microbubbles in the boundary layer was highlighted as a way to obtain better drag-reduction results.

Kim and Clever (1995) developed a correlation for predicting the persistence of drag reduction following the injection of microbubbles using experimental data. This

correlation was developed under the consideration that drag reduction is a function of the free stream velocity and gas injection rate. The correlation is stated as

$$C_f / C_{fo} = 1 - \exp\left(0.055\, Re_x^{6/7} / Re_i\right) \quad (3)$$

where Re_x is the Reynolds number based on the free stream velocity, the distance x and the kinematic viscosity of water and Re_i is the Reynolds number associated with the injection velocity of the gas through the porous section, with the length scale being the length of the region over which bubbles are injected.

Skin friction measurements were carried out by Guin *et al.* (1996) in a two-dimensional channel with an aspect ratio of 10. Air was injected through porous plates. The skin friction was measured using a miniature floating element transducer with a 5 mm circular sensing disk mounted flush on the top wall at 67 channel heights downstream of the injector. The void fraction, α, was obtained using a sampling probe and a fiber optic probe. It was confirmed that the microbubble drag reduction is inner-region dependent. In contrast with other drag reduction methods there seems to be an absence of outer-layer influence in this phenomenon. This was can be inferred from the lack of influence of the bubble distribution patterns away from the wall.

An investigation of the skin friction reducing characteristics of microbubble injection, combined with homogeneous solutions of surfactant or drag reduction polymers was carried out by Fontaine *et al.* in 1999. The experiments were performed on an axisymetric body at freestream speeds of 10.7 and 16.8 m/s. The measurements

encompassed integrated skin friction reduction as a function of the microbubble injection rate from 0 to 10 m^3/s, the concentration of Aerosol OT (6.2-130 ppm by volume) and PEO concentrations of 1 – 20 wppm.

The results of this study indicate that a combination of microbubble injection with polymer additives can produce drag reduction levels exceeding those of the individual techniques. Maximum drag reduction in the combined technique was greater than 80% for the 20 wppm polymer concentration and highest gas injection rates. One of the main objectives of this study was to analyze the combined effects of microbubble injection with homogeneous polymer solutions for additive or synergistic effects on integrated drag reduction. However, synergism between microbubbles and polymers was not observed, this means that the total effect of both combined methods is not larger that the sum of the drag reduction effects of microbubbles and polymers were they act independently.

Kodama *et al.* (2000) performed microbubble experiments in a water tunnel. The test section has 100 mm wide, 15 mm high and 3000 mm long. Microbubbles were generated in an air injection chamber by injecting air through a porous plate made of sintered bronze with nominal pore radius of 2 μm. The chamber is located at 1038 mm from the upstream end of the test section. The skin friction was measured using skin friction sensors at three different velocities U = 5, 7 and 10 m/s. The drag reduction was greater at larger air injection rate and at lower speed. It was found that the local void fraction, α, close to the wall is important for drag reduction by microbubbles.

The marker-density-function (MDF) method was developed by Kanai and Miyata (2001) to conduct direct numerical simulation (DNS) for bubbly flows. The method was applied to a turbulent bubbly channel flow to elucidate the interaction between bubbles and wall turbulence. For conditions of Weber number $We = (U^2 D_b \Delta\rho)/\sigma = 21.8$ and Froude number $Fr = U/(g\ R_b)^{1/2} = 5$ the turbulent energy was reduced. In this case, the void fraction has a peak near the wall and the streamwise velocity fluctuation in the buffer layer near the wall was reduced when the turbulent energy was reduced due to the existence of bubbles.

This indicates that the interaction between the bubbles and the wall turbulence near the wall contributes to the reduction of turbulent energy. The necessity of concentration of the bubbles near the wall, specifically within the buffer layer, to attain drag reduction was pointed out. The drag reduction effect was attributed to the prevention of the formation of the sheet-like structure of the spanwise vorticity near the wall due to the bubbles' presence. The streamwise vorticity, which is considered to be created from the spanwise vorticity detaching from the wall, was weakened, depressing the bursting phenomenon. Accordingly, the low-speed streaks below the detachment position of the spanwise vorticity disappeared reducing the turbulent energy and attaining drag reduction.

A series of numerical simulations of small bubbles seeded in a turbulent channel flow at average void fractions of up to 8% were carried out by Xu *et al.* (2002). They carried out a DNS simulation using the force-coupling method (FCM) to simulate the presence of the bubbles and their influence on the flow. The effects of bubble seeding

levels, bubble size and interactions with the turbulent flow were simulated. In this work, the bubbles are considered to be small, rigid and spherical; it is also considered that those bubbles were initially distributed in layers near each wall and then dispersed through the channel under the action of turbulence. Three different bubble diameters were used in the simulations. A transient reduction of drag was observed for large bubbles while smaller bubbles produce a sustained drag reduction. The results obtained from these simulations point out at least three mechanisms involved: one linked to the initial seeding of the bubbles, the second associated with density effects, where the bubbles reduce the turbulent momentum transfer, and the third governed by specific correlations between the bubbles and the turbulence. Turbulence modification was observed in the presence of microbubbles in the form of lifted streaks, which become more coherent while the spaces of the streaks increased for the cases where drag reduction was obtained.

Investigation of frictional resistance reduction by microbubbles were performed by Moriguchi and Kato (2002). More than 400 experiments under various conditions were performed in two-dimensional recirculating water channel. The test section was 10 mm high, 100 mm wide and 2000 mm long. Fully developed turbulent flow was attained. Microbubbles were injected through a porous plate in the test section at the upstream upper surface, generating a gas-liquid flow. Frictional resistance was measured by shear transducers at 750 mm and 1250 mm downstream of the air injection point. The diameter of the bubbles was changed by modifying the flow velocity at the air injection port. The results obtained showed that drag reduction increases as the void fraction increases. In

their study, it was found that the diameter of the microbubbles did not have an effect on the drag reduction. This result contradicts findings of other authors and it was agreed that more research work is necessary before conclusive results are obtained.

The turbulence structure of flow field including microbubbles in a horizontal channel was experimentally investigated by Kitagawa *et al.* (2003) using particle tracking velocimetry and Laser Induced Fluorescence (PTV/LIF) technique. The channel was made of transparent acrylic resin with a height of 15 mm, a width of 100 mm and a total length of 3000 mm. Air bubbles were injected into the channel through an array of holes in a plate installed at the upper wall. The inner diameter of the air injection holes was 0.5 mm. It was clarified from the obtained results that the turbulence intensity increases while the Reynolds stresses decrease with increasing void fraction.

CHAPTER II

EXPERIMENTAL SET UP AND TECHNIQUES

A detailed description of the channel flow facility and experimental techniques used in this research study is reported in this chapter. Particle Image Velocimetry (PIV) technique is used in this investigation due to its capability of providing instantaneous velocity maps without disturbing the flow thanks to its not-intrusive characteristics.

2.1 Channel Flow Facility

The experiment was carried out in a rectangular cast acrylic channel, with dimensions of 4.8 m long, 20.5 cm wide and 5.6 cm high. Water flow was circulated through a closed loop by three pumps of ½, ¼ and $^1/_6$ hp connected in parallel. First, water flowed from an upper tank, which is located about 2.02m above the channel level, to the channel by gravity. Then, water was transported to a lower tank, located 0.5m below the channel approximately, from which water was pumped to the elevated tank, which has a constant head maintained by the pumps.

The water flow rates in the different hoses were measured by three water flow meters. Two of them are GPI electronic digital meters with a measurement range from 3 to 50 GPM. The third one is a rotameter fabricated by Dwayer with a measurement range from 0 to 10 GPM.

The pressure gradient in the test section was measured with pressure taps positioned on the top wall of the channel over a distance of 157.48 cm. A Validyne pressure transducer (Model DP103) was used. This transducer has a range of pressure difference of 0-35 Pascal, the pressure drop measurements are used to calculate the wall shear stress for single phase flow.

Hydrogen microbubbles, used to achieve drag reduction, were produced by electrolysis at 10 cm upstream the test zone. Platinum wire with a diameter of 76 μm is used as electrodes. To produce hydrogen microbubbles with an average diameter of 30 μm a current of 25 mA is conducted through the electrodes. The negative electrode (cathode) produces hydrogen microbubbles whereas the positive one (anode) produces oxygen microbubbles.

The flow facility used in this research is depicted in figure 1. The schematic also shows the microbubble production set up.

2.2 Particle Image Velocimetry (PIV)

In this section, the particle image velocimetry (PIV) system used to obtain instantaneous, two-dimensional turbulent velocity fields in the channel flow facility is described. The velocity fields were measured in the x-y plane both for pure water and for two-phase flow (water and microbubbles). A brief description of the fundamental concepts of PIV is given also in this section.

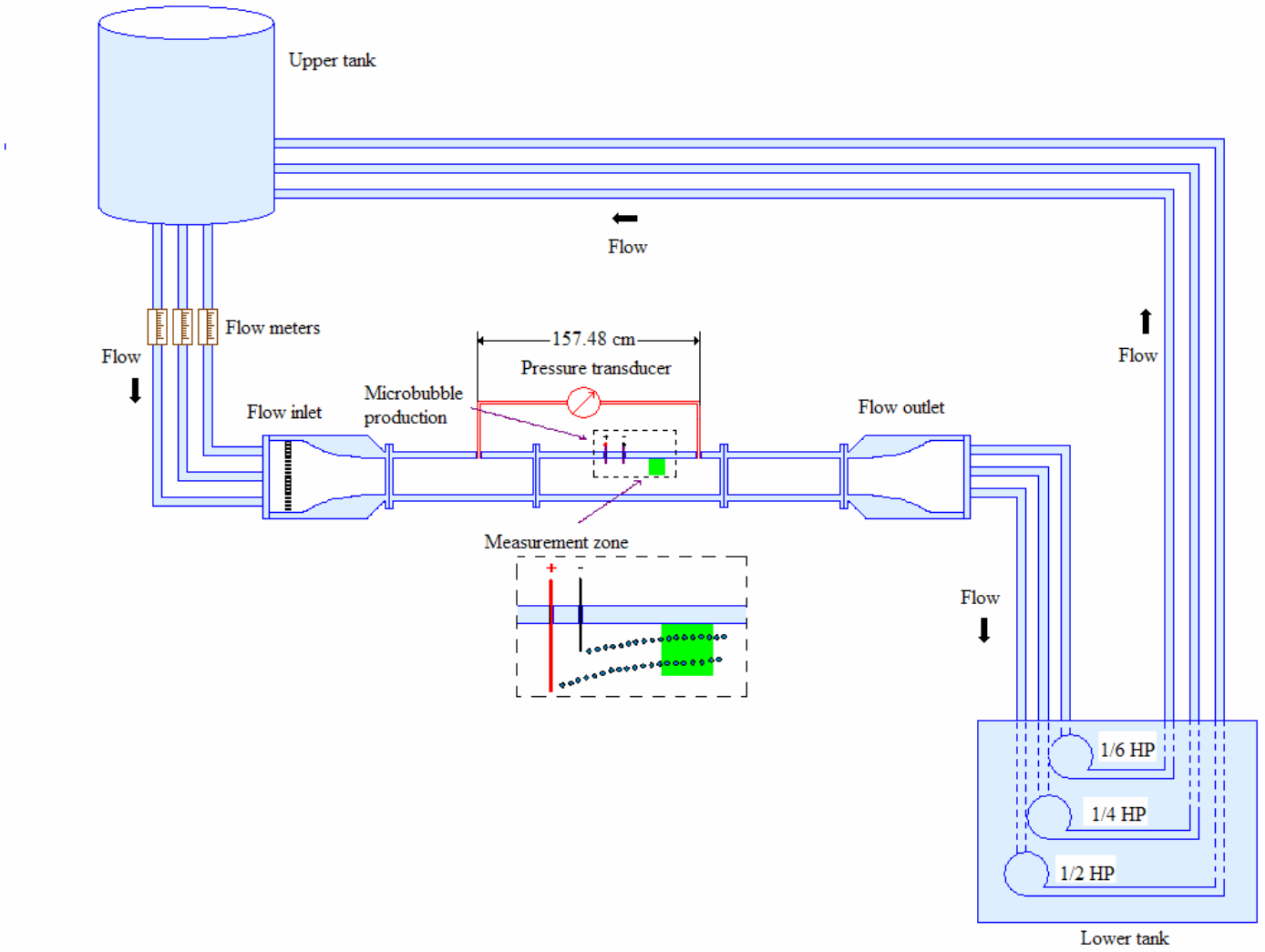

FIGURE 1. Diagram of channel flow facility.

2.2.1 Principle of PIV

In PIV applications, seeding particles, added to the flow, are used as tracers. These particles are illuminated in a plane of the flow at least twice within a short time interval; the time delay between pulses depends on the mean flow velocity and the magnification imaging. The main assumption of this technique is that the particles move with the local flow velocity between the two illuminations; this is obtained experimentally using seeding particles with a specific gravity value very close to the specific gravity value of the fluid. The light scattered by the particles is recorded either on a single frame or on a sequence of frames using either photographical film or a CCD camera. For evaluation, the PIV recording is divided in small subareas called “interrogation areas”. The local displacement of the particles of the first and second illumination is determined for each interrogation area by means of statistical methods (autocorrelation and crosscorrelation). The velocity is calculated according to its fundamental definition,

$$u(x,t) = \frac{\Delta x(t)}{\Delta t} \tag{4}$$

where Δx is the displacement of the particle over a known time interval, Δt, which is the time interval between the light illuminations (Raffel *et al.* 1998).

The interrogation method, i.e. the method of analysis depends on the type of image that is obtained, which can be low density or high density. In the low density image, the mean number of particles per interrogation cell is small ($N_I << 1$). On the other hand, high density images have particle concentrations large enough to ensure that the mean number of particles per interrogation cell is large ($N_I >> 1$).

Interrogation of an image begins by illuminating an interrogation spot with a beam of intensity $I_I(X - X_I)$, where X_I is the center of the spot. The interrogation spot intensity is given by

$$I(X) = I_I(X - X_I)\tau(X) \tag{5}$$

where $\tau(X)$ is the intensity transmissivity of the image.

The autocorrelation of I(X) is given by

$$R(s) = \int_{spot} I(X)I(X + s)dX \tag{6}$$

where s is a two-dimensional displacement vector. Autocorrelation is generally used in high density images.

The loss of pairs due to motion out of the interrogation spot can be eliminated by performing cross-correlation between first images in a small, first interrogation window and second images in a larger second interrogation window. The second window is chosen on the basis of a priori knowledge about the flow field, such as a predominant mean flow, an imposed image shift, or an estimate of the local flow direction based on neighboring vectors (Adrian, 1991).

2.2.2 Description of PIV System

The illumination source for the PIV system is a high power, dual oscillator Nd:YAG laser. The model is Spectra-Physics PIV-400-30. Each oscillator has a fixed frequency of 30 Hz. Therefore, the laser system has the capability of working at a frequency of 60 Hz.

The maximum power of the laser is rated at 400 mJ per pulse, for the 532 nm wavelength, which corresponds to green light, but the actual maximum output power achievable ranges from 300 to 350 mJ per pulse. The pulse width is about 7 ns.

High energy mirrors and lenses are required to transmit and shape the laser beam. Sharp images are obtained with the help of 60 mm focal length lenses, and a sheet of light of about 1mm thickness is used to illuminate the viewing area. The velocity field in an x-y plane is obtained by particle image velocimetry (PIV) at 3.15 m downstream from the channel inlet (L/h = 112.5). The particle seeds used for tracing the flow have small diameters range from 6-9 μm with specific gravity of 1.01 close to water's specific gravity.

The scattered laser light from the seeding particles was recorded using a CCD Kodak Megaplus camera, Model Megaplus ES 1.0/10, 1008 x 1018 pixels. This camera has a 1 inch CCD array format, and the pixel size is 9 μm. The camera has the Trigger Double Exposure capability, which allows for study of high velocity flows. Figure 2 shows the schematic of the optical configuration for PIV measurements in the x-y plane.

The viewing area was 1.28 cm^2 and was located close to the upper channel wall. The system recorded 60 images per second. Thirty velocity fields per second of the viewing are were obtained. Each velocity field was obtained from a pair of consecutive images capturing the second image of the pair 1ms after the first one via frame straddling approach. Images were recorded for a time span of approximately 3.3 sec. The total sets of velocity fields per run were 100. Several runs were obtained with the same flow

conditions for single phase flow. For two phase flow this is not possible due to the constant change in the values of the local void fraction.

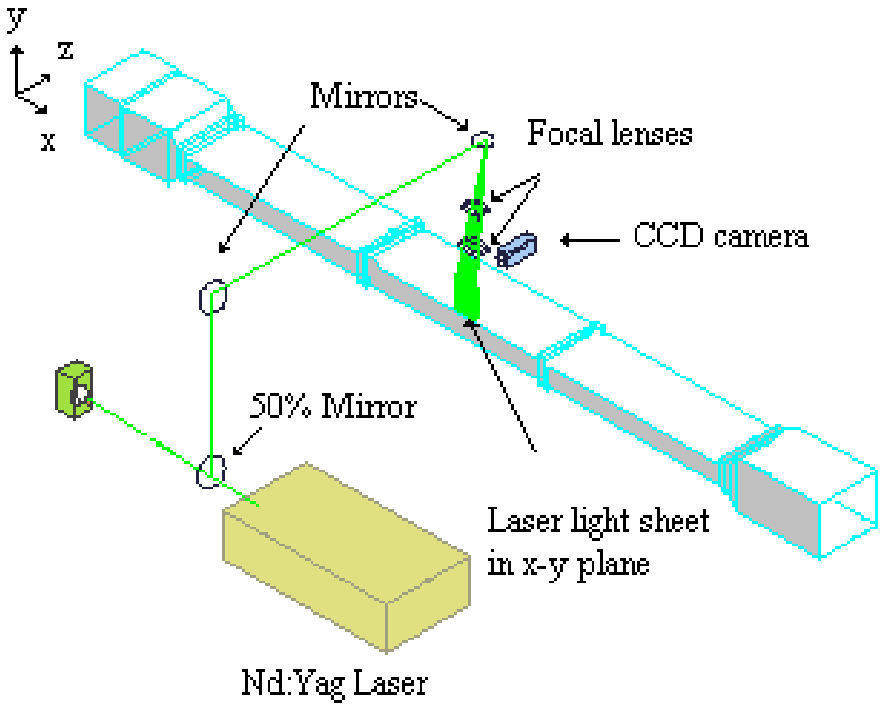

FIGURE 2. Optical configuration for PIV measurements in the x-y plane.

The image acquisition rate was 60 frames per second (fps) at a resolution of 1007 × 1007 pixel, although the normal continuous frame rate of the CCD camera is only 30 fps. The increase of the camera frame rate is a consequence of the correct synchronization between the triggered double exposure capability of the CCD camera, and the laser system light pulsing. The synchronization is performed by the high accuracy pulse

generator MFL, which has a four-channel digital delay/pulse generator. A diagram showing the synchronization system is shown in figure 3.

This pulse generator, manufactured by Stanford Research Systems, Inc. model DG535 has accuracy in the range of picoseconds. In order to achieve the 60 Hz rate, the exposure time for the first frame is only 0.128 ms, but for the second frame the CCD array is exposed for 32.4 ms. This indicates that the second CCD array is exposed, which allows to fire the second laser light pulse anytime within the 32.4 ms duration. The time length, dt between pulse 1 and pulse 2 is 1 ms. The time duration, ΔT between pulse 2 and pulse 3 is 32.33 ms. Clearly, this feature allows to study highly turbulent flows with a high spatial resolution. Figure 4 shows a diagram of the synchronization and timing used during our measurements.

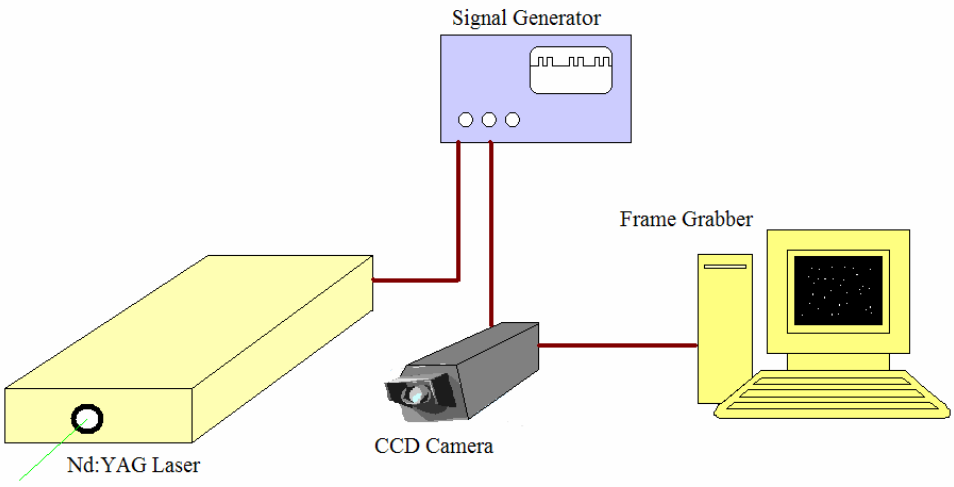

FIGURE 3. Synchronization system.

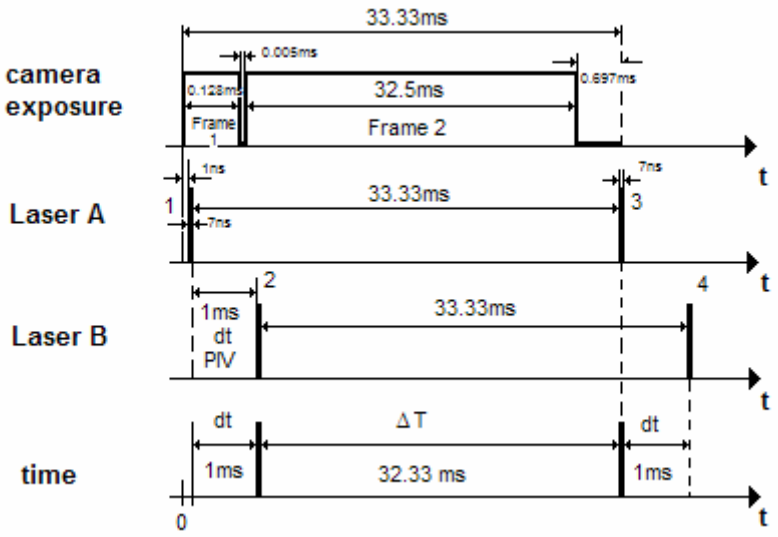

FIGURE 4. Time synchronization diagram.

2.2.3 Image Processing

A rectangular target with white dots regularly distributed was use in the PIV system calibration. The distance between adjacent dots was 2.54 mm.

To remove background, noise, reflection effects, and other distortion that can cause possible mismatching of the tracer particles through consecutive frames, image preprocessing is performed. The methodology is applied to a pair of consecutive PIV images with different illumination conditions.

The raw images are acquired by a high resolution CCD camera. The illumination conditions, i.e. the laser light intensity from one pulse to another, can change due to different exposure time for each image. An average image from the whole set of original

images is calculated. Since the illumination is different for even (Laser B) and odd (Laser A) images, two separate average images are needed, one for the odd images and other for the even images. The next step is to subtract the average images from the corresponding original images. Then, these images are equalized before using for the particle tracking routines or PIV analysis process.

Two different software applications were used for the tracking process. The resulting velocity vectors from each application were then compared against each other to avoid repetition, and then they are combined. The use of this hybrid tracking technique allows a significant increase of the total number of vectors used for the flow field analysis.

The first application works in a windows environment. One of its advantages is flexibility about the number of images that can be processed at the same time making possible to process just one pair of images or the whole set of images at once. This characteristic facilitates the setting of the image threshold and tracking conditions. This software is based on successive abandonment (SA) method. This method (SA) was modified using selected characteristic pixels which have the highest intensity and the lowest one in a line of an interrogation window. By this method, difference between correct candidate and other ones becomes clear and the SA method can be accelerated. Combined by this selected pixel approach and error detection suitable for SA, high-speed super-resolution PIV is achieved (Yamamoto, 1992).

The other tracking process is an in-house routine (Hassan *et al.* 1992), and it has been improved over the last fifteen years. This application is not windows environment friendly, and it runs on a UNIX environment. It requires the bynarization of images. The image

processing and conversion is performed through a developed application with the LabView programming environment. The tracer particle centroid algorithm runs in UNIX environment. This tracking method can be performed between two sequential, high resolution images. The particle velocity is calculated by determining the correspondence between particles in two sequential frames. The correspondence is obtained through calculation of a correlation coefficient between a referenced pattern in the first binary image and a possible candidate pattern in the second binary image, where the latter is shifted so that the centroids of the possible particle pair coincide. The velocity for a particle is determined by the particle displacement divided by the image acquisition time.

Once the velocity vectors are obtained from both particle tracking algorithms, they go through separate filtering processes. The first filter is the cross correlation value itself. In our case, only those vectors with a cross correlation coefficient value higher than the average value are considered for the flow field analysis. During this step usually about 50% of the total vectors are removed. Some of these vectors can easily be seen as incorrect vectors, i.e.; vectors with direction and/or magnitude values deviated from the neighbor vectors.

The second filter removes vectors that are not within the average +/- a standard deviation value of the magnitude and direction of the representative velocity vector within a small interrogation area. Then, those vectors very close to the image boundaries are also removed due to the high incidence of inaccuracy in this particular zone. In this step about 10% of the vectors are filtered out. In total, about 40% of the initially tracked vectors are kept for analysis after the filtering process. Finally, the remaining vectors from each

process are combined to one single file for each instantaneous velocity field. The average number of instantaneous velocity vectors within the viewing area of approximately $1cm^2$ is close to 1500.

Then, the instantaneous velocity vector fields are interpolated applying the inverse distance algorithm using windows of 20x20 pixels. The final instantaneous velocity fields have a vector distribution of 50x50 vectors.

CHAPTER III

TURBULENT CHANNEL FLOW

The fully developed turbulent boundary layer contains many interacting vortical structures. These structures are so complex in their spatial distribution and temporal evolution that the dynamical cause and effect relationships are difficult to clarify. In order to attain a better understanding of the complicated dynamics found within the boundary layer, several analysis techniques were applied. These techniques are presented in this chapter.

3.1 Equations of Motion

The principles of conservation of mass and momentum are expressed in the continuity and Navier-Stokes equations respectively:

$$\frac{\partial u_i}{\partial x_i} = 0 \tag{7}$$

$$\frac{\partial u_i}{\partial t} + u_j \frac{\partial u_i}{\partial x_j} = -\frac{1}{\rho}\frac{\partial p}{\partial x_i} + \nu \frac{\partial^2 u_i}{\partial x_j^2} \tag{8}$$

where u_i is the ith component of velocity, x_j is the spatial coordinate in the jth direction, p is the pressure, ρ is the fluid density, ν is the fluid kinematic vistosity. Equations (7) and (8) are only valid for incompressible, Newtonian fluids.

For turbulent flows, the instantaneous velocity u is decomposed into mean and fluctuating components using the “Reynolds decomposition” as it is shown in equation (9).

$$u = U + u' \tag{9}$$

where U is the mean velocity and u’ is the velocity fluctuation.

The average process to obtain the mean component of the velocity is carried out using

$$U_i = \frac{1}{N_T}\sum_{k=1}^{N_T} u_{i(k)} \tag{10}$$

Substituting the instantaneous velocity in its decomposed form into the streamwise component of the Navier-Stokes equation, averaging each term and enforcing conservation of mass the mean momentum equation in the streamwise direction:

$$U_j \frac{\partial U_i}{\partial x_j} = -\frac{1}{\rho}\frac{\partial P}{\partial x_i} + \frac{\partial}{\partial x_j}\left(\nu \frac{\partial U_i}{\partial x_j} - \overline{u'v'}\right) \tag{11}$$

The additional term on the right hand side $-\overline{u'v'}$, comes from the product of the fluctuating velocities and represents the transport of momentum by the fluctuating components of the velocity. This term is commonly known as turbulent stress or Reynolds stress. For fully developed two-dimensional channel flow equation (11) can be reduced to

$$0 = -\frac{1}{\rho}\frac{\partial P}{\partial x_1} + \frac{\partial}{\partial x_2}\left[\nu \frac{\partial U_1}{\partial x_2} - \overline{u'v'}\right] \tag{12}$$

where ρ is density, ν is kinematic viscosity of the fluid, and U is the local mean velocity. The terms inside the brackets are the Newtonian viscous stress and the Reynolds shear stress respectively.

The Newtonian viscous stress is important in a region close to the wall. In such region, the layers of fluid feel a retardation effect of the solid boundary at the molecular level (Bernard and Wallace, 2002). Far from the wall, the molecular momentum flux is replaced by a turbulent momentum flux, represented by the Reynolds stress.

The region close to the wall $\left(0 \le y^+ < 5\right)$ is known as the viscous sublayer; the buffer layer is located in the zone from $y^+ = 5$ to $y^+ = 70$, whereas the overlap layer is located in the region were $y^+ > 70$. In the viscous sublayer, it is convenient to scale quantities in terms of parameters such as kinematic viscosity, ν, and the wall shear stress, τ_w, which is defined as

$$\tau_w = \mu \left.\frac{dU}{dy}\right|_{y=0} \tag{13}$$

The wall shear stress is a quantity that determines the energy needed for moving the flow of liquids and gases over solid walls (Fernholz, *et al*. 1996). For a fully developed channel flow, which is homogeneous in the streamwise direction, there is an exact balance between the wall shear stress acting on the walls and the net pressure force acting across the flow. A force balance produces

$$\tau_w = -h\frac{dP}{dx} \tag{14}$$

where h is half of the channel height, and dP is the pressure drop in the streamwise direction.

An inner velocity, u_τ, known as friction velocity is defined in terms of the wall shear stress by

$$u_\tau = \sqrt{\frac{\tau_w}{\rho}} \tag{15}$$

A corresponding length scale for this region, which is also known as wall layer thickness or viscous length scale (Schlichthing and Gersten, 2000) may be determined from the two characteristic quantities ν and u_τ :

$$\ell = \frac{\nu}{u_\tau} \tag{16}$$

For the viscous region, the time scale is defined as

$$t_\tau = \frac{\nu}{u_\tau^2} \tag{17}$$

These are called inner scales (Fisher *et al.* 2001). These scales can be used to make different variables not-dimensional. These non-dimensional variables are commonly known as “wall units”

$$y^+ = \frac{y}{\ell} = \frac{yu_\tau}{\nu} \tag{18}$$

$$U^+ = \frac{U}{u_\tau} \tag{19}$$

$$t^+ = \frac{t}{t_\tau} \tag{20}$$

Close to the wall, the relation

$$y^+ = U^+ \tag{21}$$

holds to a high degree of accuracy. Experiments have shown that equation (21) is very accurate until $y^+ \approx 5$. Equation (21) is known as the law of the wall.

The log law represents and extension of the law of the wall to the intermediate layer. It can be expressed as

$$U^+ = \frac{1}{\kappa} \ln y^+ + B \tag{22}$$

where κ is the Kármán constant, which has a value of 0.42 constant and B is a "universal constant" that has taken several values according to different experiments. The most common value for B is 5.5. The validity of the log law stands in the overlap layer ($y^+ > 70$).

3.2 Statistics

Several different techniques were used to analyze the behavior of the channel flow. Velocity statistics were obtained from PIV measurements in the x-y plane. These velocity statistics are determined by ensemble averaging over the number of velocity fields,

$$\overline{A} = \frac{\sum_{i=1}^{N} A_i\left(\overline{X}\right)}{N} \tag{23}$$

where A is the quantity being averaged, $\overline{X}$ is the position vector, and N is the total number of realizations. The result from equation (23) is a two-dimensional average

vector field. Further averaging can be done in the x-direction due to the assumption of fully developed channel flow. The fluctuating velocity fields were obtained using the Reynolds decomposition for each vector in each instantaneous velocity field.

3.2.1 Turbulent Intensities and Reynolds Shear Stress

The intensity of turbulence is defined as the rms value of the fluctuating velocities. The streamwise (u_{rms}) and normal (v_{rms}) turbulent intensities were calculated using

$$u_{rms}(x,y) = \sqrt{\frac{1}{N}\sum_{i=1}^{N}\left[u_i(x,y) - U(x,y)\right]^2} \tag{24}$$

The total shear stress, τ_t, across half height of the channel can be determined from

$$\tau_t = \mu\frac{dU}{dy} - \rho\overline{u'v'} \tag{25}$$

where $\mu(dU/dy)$ is the viscous stress and $-\rho\overline{u'v'}$ is the Reynolds shear stress. The viscous component of the total shear stress can be determined from the measured streamwise velocity profile. The derivative dU/dy is calculated using a central difference scheme.

The Reynolds shear stress is the contribution of the turbulent motion to the main stress tensor. The Reynolds shear stress can be obtained from equation (25) for single phase flow, because the viscous component of the total shear stress can be known and the total stress τ_t varies linearly with the distance from the wall

$$\tau_t = \tau_w \left[1 - \frac{y}{h} \right] \tag{26}$$

where τ_w is the wall shear stress, which can be determined form the pressure drop, y is the distance from the wall and h is half height of the channel. Reynolds shear stress can also be measured directly from PIV using

$$\overline{u'v'}(x,y) = \frac{1}{N} \sum_{i=1}^{N} \{ [u'_i(x,y)][v'_i(x,y)] \} \tag{27}$$

3.2.2 Correlation Coefficients

Velocity correlation measurements are useful for obtaining direct estimates of the turbulence length scales. In this work, several correlation coefficients calculations were used to analyze the turbulent flow.

3.2.2.1 Two-point Correlation Coefficients

The two-point or Eularian correlations play a leading part in turbulence theory. In general, the velocity correlations can be expected to be dependent on two things: a) distance between the two points, and b) the absolute value of the velocities.

The correlations values depend on distance because as we move the measuring points apart, it is expected the correlation to die away. Furthermore, the magnitude of the correlations at a fixed separation must also depend on the absolute values of the measured velocities (McComb 1990).

The first suggestion of the use of the statistical correlation in the analysis of turbulence was made by Taylor (1935). He pointed out that without any regard of the definition of the diameter of an eddy, if the separation of two points in space is small compared with the eddy diameter, there must be a high degree of correlation between the velocities at those points. If such points are taken so far apart that the distance between them is larger than the diameter of an eddy, little correlation can be expected. The two-point correlation coefficient also called Eularian correlation (Brodkey 1967), can be obtained from

$$R_{ij}(\Delta r) = \frac{\overline{u'_i(r)u'_j(r+\Delta r)}}{u_{rms_i}(r)u_{rms_j}(x+\Delta r)} \tag{28}$$

where u' is the fluctuating velocity , u_{rms} is the rms velocity fluctuation of turbulence intensity at the point in question, and Δr is the distance separation between the two points.

The integral length scale can be calculated from the value of the two-point correlation function, using the area under the velocity two-point correlation curve. This scale is thought to be the average size of the eddies. This scale can be calculated from

$$L_{ij} = \int_0^b R_{ij}(\Delta r)dr \tag{29}$$

where L_{ij} is the integral length scale, R_{ij} is the two-point correlation coefficient, and 0 an b are the limits of the span region where R_{ij} is positive, i.e. b is the point where the correlation coefficient becomes zero.

3.2.2.2 Autocorrelation Coefficient

For statistically stationary processes, the simplest multi-time statistic that can be considered is the autocorrelation coefficient (Pope 2000), also known as the Lagrangian correlation, which can be expressed as

$$R_{ij}(\Delta t) = \frac{\overline{u'_i(t)u'_j(t+\Delta t)}}{u_{rms_j}(t)u_{rms_j}(t+\Delta t)} \tag{30}$$

The autocorrelation function has the properties

$$R_{ij}(0) = 1 \tag{31}$$

$$\left|R_{ij}(\Delta t)\right| \le 1 \tag{32}$$

For processes present in turbulent flows, the correlation diminishes as the lag time Δt increases.

The definition of the Lagrangian integral time-scale T_L is given by

$$T_L = \int_0^b R_{ij}(\Delta t)dt \tag{33}$$

3.2.2.3 Two-dimensional Two-point Correlation Coefficients

The computation of the 2D correlation coefficient function is very advantageous due to the possibility to measure the correlations in any arbitrary direction on the measurement plane (Piirto *et al.* 2001). The two-dimensional correlation function can be obtained from

$$R_{ij}(\Delta x, \Delta y) = \frac{\overline{u'_i(x,y)u'_j(x+\Delta x, y+\Delta y)}}{u'_{rms_i}(x,y)u'_{rms_j}(x+\Delta x, y+\Delta y)} \quad (34)$$

3.2.3 Vorticity

A better understanding of many aspects of turbulent flows can be gained from the dynamics of the vorticity field. Vorticity is a local propert of the flow field (Panton 1996), which is a measure of the rotation of a fluid element as it moves in the flow field (Fox and McDonald 1998).

$$\omega = \nabla x U \quad (35)$$

where V is the fluid velocity. Vorticity can be calculated using the average, the instantaneous, or the fluctuating velocity field. One of the advantages of PIV measurements is that it can offer information about the vorticity field from the spatial distribution of velocity. In this case, since measurements are carried out in the x-y plane, just one component (spanwise) of the vorticity vector can be obtained. Therefore, the expression for instantaneous spanwise vorticity is

$$\omega_z = \left(\frac{\partial u}{\partial y} - \frac{\partial v}{\partial x} \right) \quad (36)$$

The derivative calculation is carried out using central difference scheme. Substituting the fluctuating components of the velocity in equation (36), the fluctuating spanwise vorticity can be obtained. Likewise, the substitution of the average velocity components will yield the average vorticity field.

3.2.4 Rate of Strain

Straining or deformation is important because is related to the stresses in the fluid. The total straining velocity is directly proportional to the symmetric part of the velocity gradient tensor, which is called the strain-rate tensor of the rate of deformation tensor. For mean flow, the rate of strain tensor can be obtained from

$$S_{ij} = \frac{1}{2}\left(\frac{\partial U_i}{\partial x_j} + \frac{\partial U_j}{\partial x_i} \right) \tag{37}$$

From the mean rate of strain the turbulent energy Production can be obtained from

$$P = -\overline{u_i u_j} S_{ij} \tag{38}$$

The rate at which viscous stresses perform deformation work against the fluctuating strain rate is called viscous dissipation. It can be expressed as

$$\varepsilon = 2\nu \overline{s_{ij} s_{ij}} \tag{39}$$

where ν is the kinematic viscosity of the fluid and s_{ij} is the fluctuating rate of strain, which can be expressed as

$$s_{ij} = \frac{1}{2}\left(\frac{\partial u'_i}{\partial x_j} + \frac{\partial u'_j}{\partial x_i} \right) \tag{40}$$

The fluctuating strain rate s_{ij} is larger than the mean rate of strain S_{ij} when the Reynolds number is large. This implies that the eddies contributing most to the dissipation of energy have very small convective time scale compared to the time scale of the flow (Tennekes and Lumley 1972).

3.2.5 Quadrant Analysis

The idea of quadrant splitting was introduced by Wallace *et al.* (1972). The instantaneous value of u'v' is classified according to the sign of u' and v'. The u'v' product is separated into its four possible sign combinations: Q1 (u' > 0, v' > 0); Q2 (u' < 0, v' > 0); Q3 (u' < 0, v' < 0); and Q4 (u' > 0, v' < 0).

A conditional sampling technique is used to quantify the contribution to the Reynolds shear stress during the cycle of events observed close to the wall in the boundary layer. The cycle of events includes the burst or ejections (ejections of low momentum fluid away from the wall) appear in the second quadrant (u' < 0, v' > 0) and the sweeps (inrushes of high momentum fluid towards the wall) in the fourth quadrant (u'>0, v'<0). This technique sorts contributions to $\overline{u'v'}$ into quadrants of the u'- v' plane (Antonia 1981). As initially proposed by Lu and Willmart (1973), the conditioning function is

$$h_j(t_i) = \begin{cases} 1, & \text{if the point } (u', v') \text{ is in the jth quadrant of the u'-v' plane.} \\ 0, & \text{otherwise.} \end{cases} \tag{41}$$

To identify more accurately contributions from violent ejections and sweeps equation (41) was modified.

$$S_j(H, t_i) = \begin{cases} 1, & \text{if } |u'v'| > H u_{rms} v_{rms} \text{ and the point } (u', v') \text{ is in} \\ & \text{the jth quadrant of the u'-v' plane} \\ 0, & \text{otherwise.} \end{cases} \tag{42}$$

The importance of the quadrant analysis lies on the empirical observation that bursts and sweeps are the dominant contributors to the Reynolds stress (Gordon 1975). Furthermore, increase of drag in turbulent flows is associated with the presence of coherent structures in the wall layer, which provides, through velocity fluctuations, the large momentum transfer from the bulk region of the flow towards the wall (Kline *et al.* 1967), as well as to the associated ejection/sweep events (Fukagata *et al.* 2002) . Quasi-streamwise vortices (vertical structures mainly aligned along the streamwise direction) and low and high speed streaks (regions with longitudinal velocity smaller and larger than the local mean value respectively are the main ingredients to sustain turbulence (Robinson 1996).

Through their interactions, a pseudo-cyclic process is originated. This process consists of: formation of quasi-streamwise vortices, creation of streaks through the lift-up mechanism, streak instability, break-down and regeneration of new vortices (Welaffe 1997).

3.3 Visualization Techniques

Although Reynolds decomposition of velocity into mean and fluctuating components is the standard method to characterize turbulent velocity fields, and offers the right bases for statistical analysis of the turbulent flows, it is not always the best method for visualizing turbulent structures in the flow.

When the primarily objective is investigate the dynamics of small-scale vortices or any other structures, and then the use of different methods for detection of such structures is the better path to follow.

3.3.1 Modified Reynolds Decomposition

To improve the detection of vortices or any other kind of coherent structures in a turbulent velocity field, a modification of the Reynolds decomposition is proposed. This technique is based on the concepts of the traditional Reynolds decomposition and the Galilean decomposition.

The traditional Reynolds decomposition was already discussed in this chapter and stated mathematically in equation (9). In the Galilean transformation the total velocity is represented as the sum of a constant convection velocity, Uc, plus the deviation

$$u = U_c + u_c \tag{43}$$

In 2000, Adrian *et al.* selected different fractions of the centerline velocity as the convection velocity to implement the Galilean transformation technique.

From these concepts, a new decomposition technique is proposed. In this case, a time averaging process is carried out to obtain the mean velocity, just as it is done in the Reynolds decomposition; however, to obtain the fluctuating component of the velocity, just a fraction of this mean velocity is subtracted from the instantaneous velocity, this can be expressed as

$$u = fU + u' \tag{44}$$

where U is the mean velocity, f is any number between 0 and 1 (if f = 1 this constitute the traditional Reynolds decomposition), and u' is the fluctuating velocity obtained.

3.3.2 Spatial Decomposition

This is another method used to elucidate structures in fluctuating velocity fields. In this case, the mean velocity is calculated from spatial averaging in a statistically homogenous direction. In this case, that direction is the streamwise (x – direction), since the flow is fully developed. This decomposition can be expressed as

$$u = U_s + u'_s \tag{45}$$

where U_s is the mean velocity obtained by spatial averaging in the x-direction for each y position.

3.3.3 Vortex Identification

Vorticity analysis is generally used to identify locations of vortices. However, vorcity not only identifies vortex cores, but also detects any shearing motion in the flow. Strong shear layers are very common the near wall region in turbulent wall-bounded flows. These regions frequently mask the presence of eddies or vortices in vorticity maps.

In 1990 Chong *et al.* suggested that a vortex core is a region of space where the vorticity is sufficiently strong to cause the rate-of-strain tensor to be dominated by the

rotation tensor, i.e., the rate-of-deformation tensor has complex eigenvalues. This definition depends only on the properties of the deformation tensor; it is independent of the frame of reference.

In three dimensions, the rate of deformation tensor will have a real eigenvalue (λ_r) and a pair of complex conjugate eigenvalues ($\lambda_{cr} \pm \lambda_{ci}$) when the discriminant of its characteristic equation is positive. It this is true, the particle trajectories about the eigenvector corresponding to λ_r exhibit a swirling, spiral motion; λ_{ci}^{-1} represents the period required for a particle to swirl once about the λ_r-axis. If $\lambda_{ci} > 0$, the fluid particle corresponds to short almost circular ellipses, i.e. eddies. This technique has been successfully applied by Zhou *et al.* (1996, 1999) for three dimensional flows, where it was shown that the strength of any local swirling motion is quantified by λ_{ci}.

The application of this particular technique in two-dimensional velocity fields obtained from PIV measurements was presented by Adrian *et al.* (2000). For two-dimensional measurements, an equivalent two-dimensional form of the velocity gradient tensor is used

$$\underline{\underline{D}}^{2-D} = \begin{bmatrix} \frac{\partial u_i}{\partial x_i} & \frac{\partial u_i}{\partial x_j} \\ \frac{\partial u_j}{\partial x_i} & \frac{\partial u_j}{\partial x_j} \end{bmatrix} \tag{46}$$

In this case, $\underline{\underline{D}}^{2-D}$ will either have two real eigenvalues or a pair of complex conjugate eigenvalues. Hence, vortices can be identified by plotting regions were $\lambda_{ci} > 0$.

CHAPTER IV

MICROBUBBLE DRAG REDUCTION AND BOUNDARY LAYER MODIFICATIONS

The addition of microbubbles within the boundary layer to achieve drag reduction has been studied for a long time. A series of consistent results has been obtained from several different researchers over a period of time (McCormick and Bhattacharyya 1973; Bogdevich *et al.* 1977; Madavan *et al.* 1985; Merkle and Deutsh 1989; Kato *et al.* 1994; Kim and Clever 1995; Guin *et al.* 1996; Kodama *et al.* 2000; Kanai and Miyata 2001; Xu *et al.* 2002; Moriguchi and Kato 2002). Some preliminary results about modification of the boundary layer structure by microbubbles have been already presented. However, the aim of this work is to present a more extensive study of the effects of microbubbles presence within the boundary layer. Results obtained from the PIV measurements for single phase and two-phase flow are presented in this chapter.

4.1 Mean Quantities

For this investigation, velocity measurements were made at a Reynolds number, Re_h = 5128 approximately, where the Reynolds number is calculated using half height of the channel and the bulk velocity. To attain drag reduction, microbubbles of an average

diameter of 30 μm were injected using electrolysis as method of production. The general characteristics of the flow are shown in table 1.

$U_b = 18.3$ cm /s	$\delta_{99} = 3.9$ mm
$Re_h = \frac{U_b h}{\nu} = 5128$	$\delta^* = \int_0^\infty \left(1 - \frac{u}{U}\right) dy = 1.25$ mm
$Re_\tau = \frac{u_\tau h}{\nu} = 324.8$	$\theta = \int_0^\infty \left(\frac{u}{U} - \left(\frac{u}{U}\right)^2\right) dy = 0.75$ mm
$\frac{U_b}{u_\tau} = 15.7$	$\frac{\delta^*}{\theta} = 1.66$
$C_f = \frac{\tau_w}{\frac{1}{2}\rho U_b^2} = 8.03 \times 10^{-3}$	$\frac{\delta^*}{\delta_{99}} = 0.32$

TABLE 1. Mean flow variables

The values presented were compared with the computed values obtained by Kim *et al.* (1987) for fully developed channel flow. They found that the value of the bulk mean velocity normalized by the friction velocity is 15.63, which is in reasonable agreement with the value obtained in this study of 15.7. There is also good agreement for the result of the displacement thickness normalized by the momentum thickness, which in their case is 1.62, compared with the value of 1.66 found in this case. The ratio of the displacement thickness and the boundary layer thickness is approximately 1/3 as accounted for in the literature (Schlichting and Gersten 1999). The skin friction

coefficient, $C_f = \tau_w \Big/ \frac{1}{2}\rho U_b^2$ is $8.03x10^{-3}$, is in reasonable agreement with Dean's suggested correlation of $C_f = 0.073 Re_h^{-0.25} = 8.62x10^{-3}$ (Dean, 1978).

The non-dimensional mean streamwise $U^{+,}$ versus the non-dimensional y location, y^+, velocity is shown in figure 5. The abscissa is in log coordinates to expand the inner region of the velocity profile and perform a better analysis. For $y^+ < 7$, the measured data agree well with the law of the wall. For $y^+ \geq 30$, there is a good agreement between the obtained data and the log law. Results for a fully developed channel flow obtained form LDV (Warholic 1997) at very similar conditions were included to validate the results obtained using PIV, a good agreement is observed.

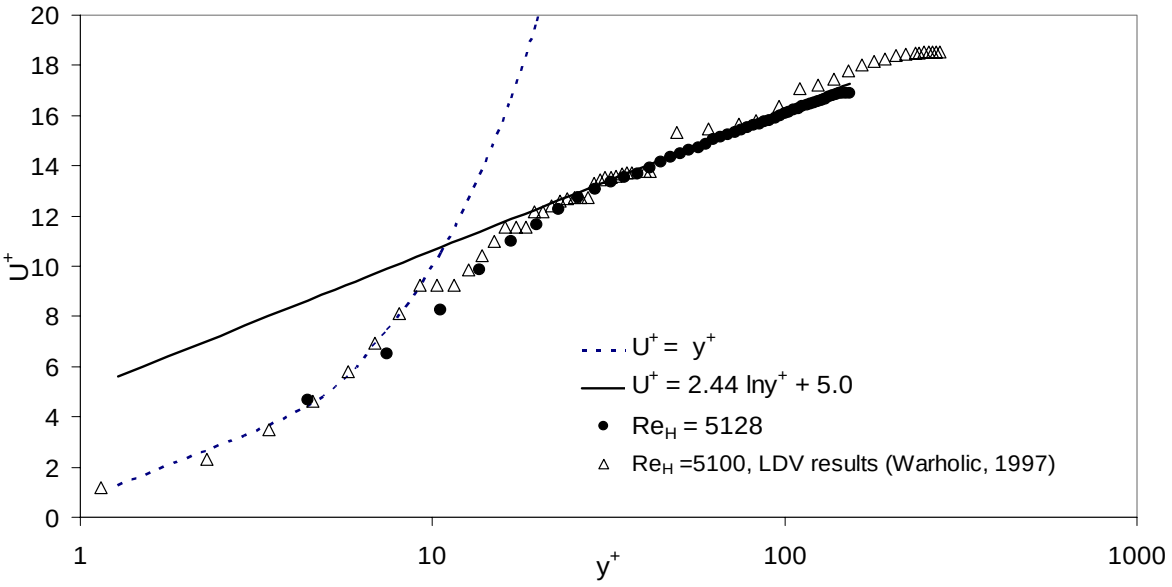

FIGURE 5. Non-dimensional streamwise velocity, U^+, versus the non-dimensional distance from the wall, y^+, for single phase flow.

The wall shear stress for single phase was calculated by equation (14). It was also evaluated by equation (13) using the measured velocity fields from PIV. The derivative was computed with the second order central difference scheme. The wall shear stress values from the two methods are shown in table 2.

Re_h (Single phase)	τ_w from pressure drop [N/m^2] equation (14)	τ_w from $\mu \left.\frac{dU}{dy}\right\|_{y\approx 0}$ [N/m^2]
5128	0.134	0.139

TABLE 2. Comparison of wall shear stress values for single phase

It can be observed that a reasonable agreement was obtained from the two approaches. Based on these results, the PIV measurements were used to estimate the shear stress in two-phase flow conditions.

The Two-phase flow measurements were performed with different void fraction values. The generated bubble size was 30 μm. The void fraction value within the measurement zone was estimated using the following relation:

$$\alpha = \frac{V_g}{V_g + V_l} \tag{47}$$

where V_g is the volume of the gas bubble in the viewing volume, and V_l is water volume in the viewing volume. The test volume has dimensions of $\Delta x = \Delta y = 11.31$ mm and $\Delta z \cong 1$ mm. The drag reduction, DR is obtained from the equation

$$DR = \left[1 - \left(\frac{u_{\tau 2-phase}}{u_{\tau sin glephase}} \right)^2 \right] \tag{48}$$

The values of the drag reduction with various void fractions for Reynolds number of 5128 approximately are summarized in table 3. The diameter, d, of the bubble is presented in wall units $\left(d^+ = \frac{du_\tau \rho}{\mu} \right)$, where u_τ is the friction velocity.

u_τ [m/s]	0.0108	0.0106	0.0097	0.0091
d+	0.32	0.31	0.29	0.27
Void fraction (α)	2.4%	3.4%	4.4%	4.9%
Drag Reduction	12.06%	16.4%	29.8%	38.4%

TABLE 3. Drag reduction at various void fraction conditions

4.2 Turbulent Intensities

The non-dimensional streamwise turbulent intensity (u_{rms}) profiles for single phase flow and two-phase flow are shown in figure 6. The streamwise turbulent intensity for single phase flow reaches a maximum at $y^+ \approx 15$. The magnitude of the peak intensity is 2.55. Both results, the magnitude or the peak intensity and the position (y^+) agree with experimental results for fully developed channel flow for water presented by Warholic (1997), $u^+_{rms,max} = 2.6$ at $y^+ = 15$ for Re = 5100. There is also agreement with results obtained from DNS simulations presented by Günter *et al.* (1998) for a channel flow at Re = 5750, where $u^+_{rms,max} \approx 2.61$ at $y^+ = 15$. These results agree with the findings of Durst *et al.* (1996), where experimental results for fully developed channel flow at different Reynolds number conditions were reported. In this work, experimental measurements at low Reynolds numbers in a range from Re_h = 1250 to 4900 are reported. In all the cases, the peak value for the streamwise turbulence intensity remains constant at a value of 2.55 approximately. The location of this peak also remains constant at $y^+ \approx 15$.

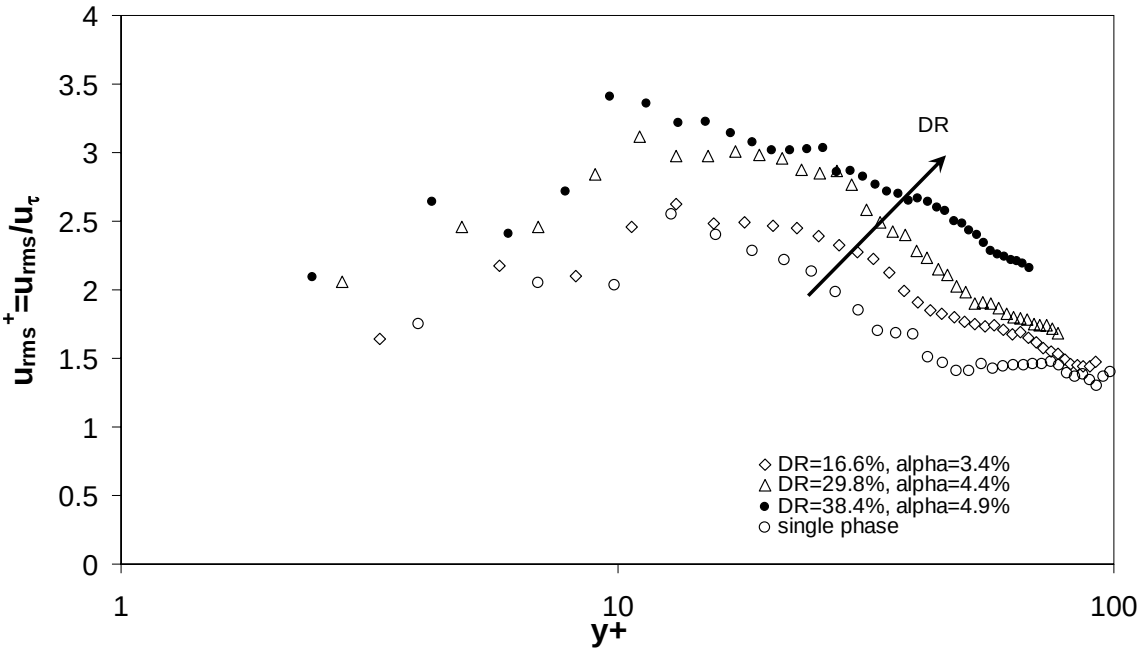

FIGURE 6. Non-dimensional streamwise turbulent intensities.

An increase in the magnitude of the streamwise turbulence intensity is observed when microbubbles are injected. As the local void fraction increases, there is an increase in the drag reduction effect. It is also observed that as void fraction and drag reduction increases, there is an increase in the value of the non-dimensional streamwise turbulent intensities. This behavior coincides with results reported about drag reduction by polymer injection investigations.

The non-dimensional normal turbulent intensities, v_{rms}^{+}, for single-phase flow and two-phase flow are shown in figure 7.

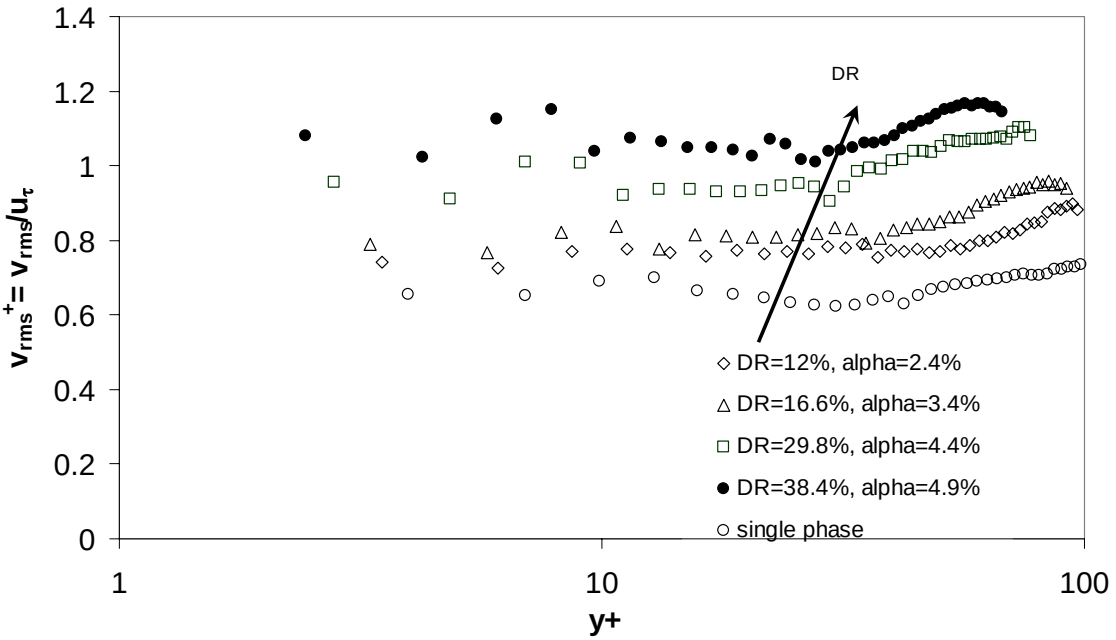

FIGURE 7. Non-dimensional normal turbulent intensities.

It can be seen in figure 7 that there is an increase in the magnitude of the normal turbulence intensity with the increase of the drag reduction. This trend is opposite to the one observed in the results involving drag reduction by polymers injection (Virk 1975; Wei and Willmarth 1992; Warholic *et al.* 2001).

4.3 Reynolds Stresses

Reynolds stresses, for single phase flows, can be obtained from the velocity fields and the values of wall shear stress from equation (25) using $-\rho\,\overline{u'v'} = \tau_w\left[1-\frac{y}{H}\right]-\mu\frac{dU}{dy}$. The viscous stress can be obtained from the measured streamwise mean velocity profile. A

comparison between Reynolds stresses results directly obtained from PIV measurements and results obtained using equation (25) is shown in figure 8. A reasonable agreement was observed between the two methods. The standard deviation between of the measured results and calculated results is 0.25 (6.37%).

Experimental results for Reynolds stresses $-\rho\overline{u'v'}$ for various values of local void fractions from 2.4% to 4.9% are shown in figure 9. The shear stresses are presented as function of the non-dimensional distance from the wall y^+.

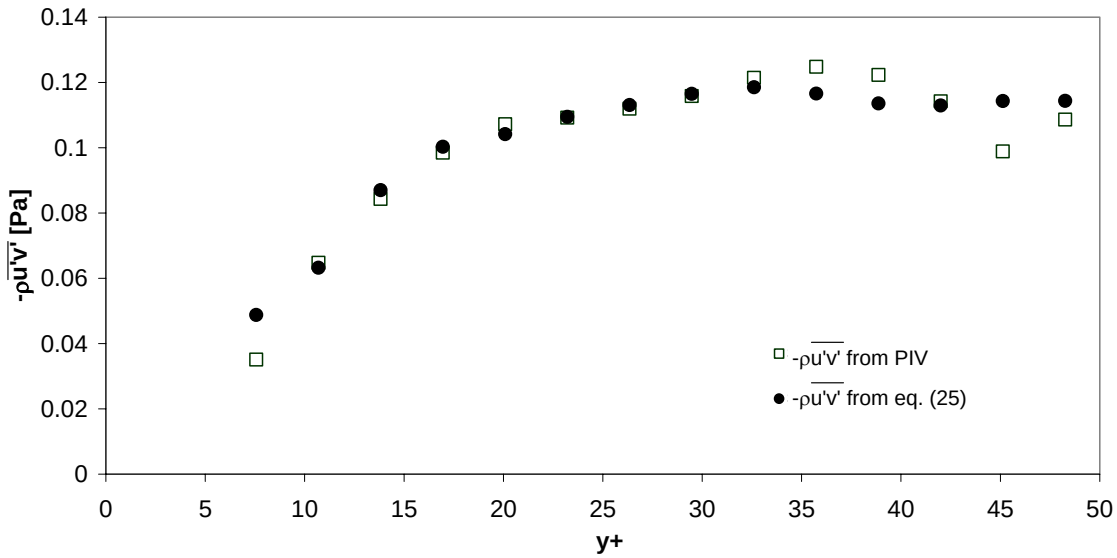

FIGURE 8. Comparison between values of Reynolds stresses obtained by two independent techniques.

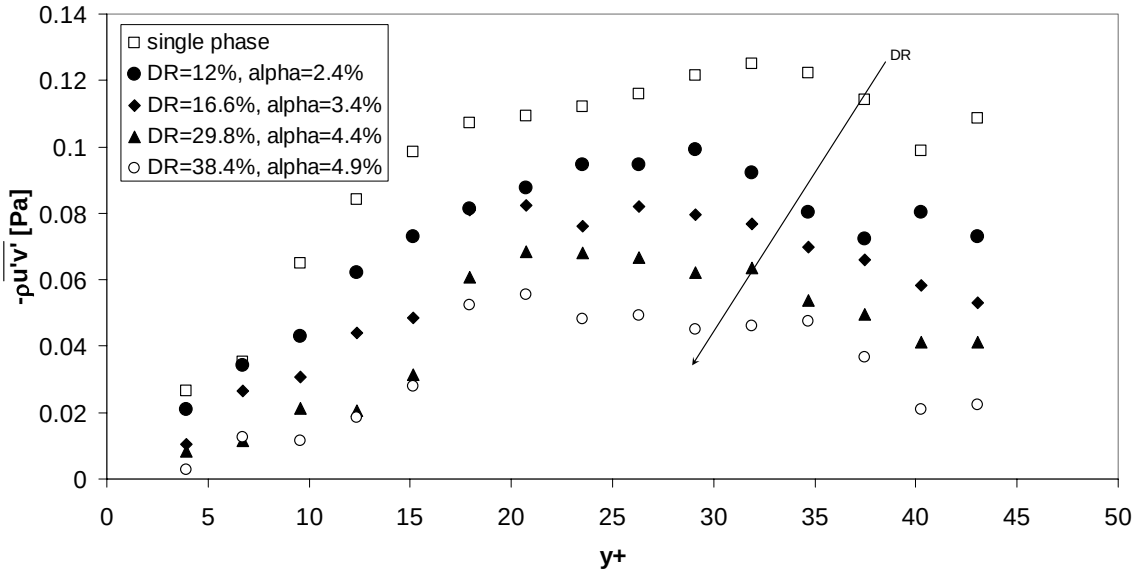

FIGURE 9. Reynolds shear stress versus the normalized distance from the wall y^+, for several void fraction cases.

A significant decrease in the Reynolds stress with increasing local void fraction is obtained. This effect is sometimes called Reynolds stress defect in different experiments with drag-reducing polymers. This reduction in the value of the Reynolds stresses is a function of the local void fraction, as the void fraction increases, the Reynolds stresses decrease. A decorrelation between the streamwise (u') and the normal (v') velocity fluctuating components is the source of these decrease of the Reynolds stresses. This phenomenon may be explained due to a modification in the organized structures in the viscous sublayer and the buffer layer (Robinson 1991).

Sreenivasan (1988) examined measurement of wall-bounded turbulent flow. From a least-square fit of the Reynolds stress peak locations, he obtained:

$$y^{+}_{uv,peak} = 2(Re_{\tau})^{0.5} \quad (49)$$

where $y^{+}_{uv,peak}$ is the non-dimensional y-location of the peak Reynolds shear stress and Re_{τ} is the Reynolds number based on the half channel height and the friction velocity u_{τ}. The calculated peak location is $y^{+}_{uv,peak} \cong 36$ for $Re_{\tau} = 324.8$.

4.4 Two-point Correlation Coefficients

To elucidate the changes that the presence of microbubbles originates within the turbulent boundary layer, two-point correlation coefficients are calculated in the longitudinal (streamwise) direction at different distances from the wall (y-positions) for the streamwise and normal fluctuating components of the velocity. Furthermore, the integral length scale for each case is computed and presented. Figures 10 and 11 show the two-point correlation function for the streamwise and normal fluctuating velocities respectively. These calculation are performed in the longitudinal direction at a fixed distance from the wall $y^{+} = 9.2$. It can be observed that when microbubbles are injected, the two-point correlation coefficient values increase for the streamwise fluctuating velocity. On the other hand, for the normal component of the fluctuating velocity the two-point correlation values decrease as the local void fraction increases.

The integral length scale calculations for the two-point correlation function at $y^{+} = 9.2$ are shown in table 4. The results found are consistent with the behavior observed in

figures 10 and 11; there is an increase in the value of the integral length scale for the streamwise velocity and a decrease for the length scale calculated from the normal velocity.

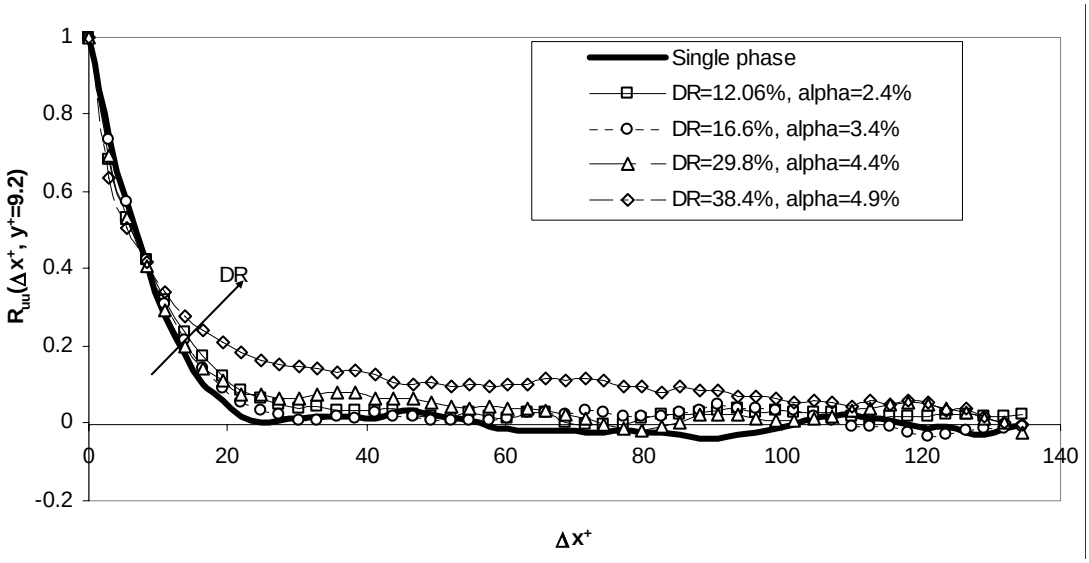

FIGURE 10. Two-point correlation coefficient in the longitudinal direction at $y^+ = 9.2$ for streamwise fluctuating velocity.

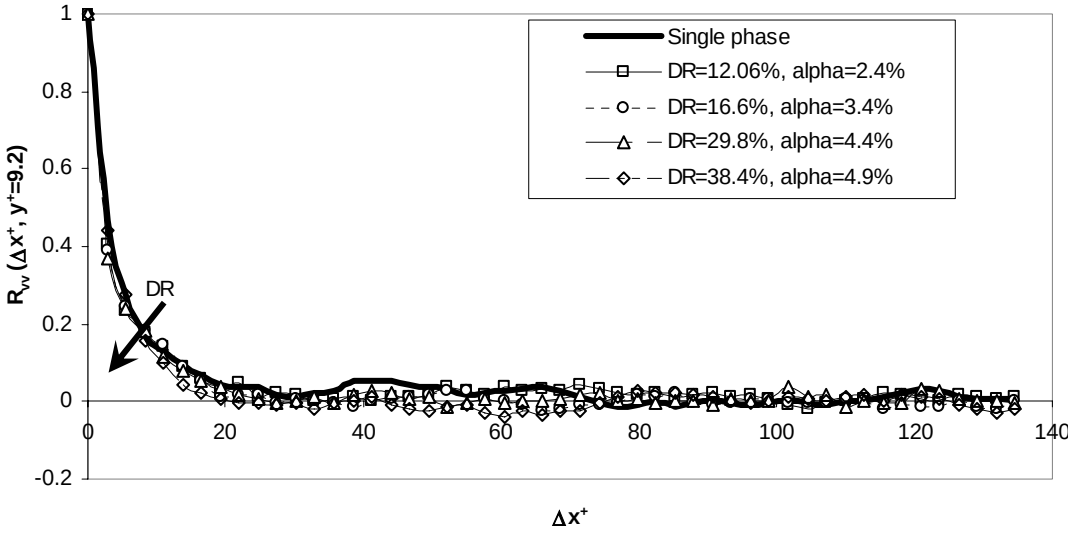

FIGURE 11. Two-point correlation coefficient in the longitudinal direction at y^+ = 9.2 for normal fluctuating velocity.

Longitudinal direction (y^+ = 9.2)	Single phase	DR=12.06%, α=2.4%	DR=16.6%, α=3.4%	DR=29.8%, α=4.4%	DR=38.4%, α=4.9%
L_{uu} [mm]	0.68	0.81	0.86	0.89	1.58
L_{vv} [mm]	0.53	0.49	0.33	0.32	0.30

TABLE 4. Integral length scales from longitudinal two-point correlation coefficients at y^+ = 9.2

To find out if this tendency was also found within the buffer layer, the same calculations for the two-point correlation values in the longitudinal direction at y^+ = 14.7, 17.4, and 25.7 for streamwise and normal velocity fluctuations were performed. These results are shown in figures 12 to 17. The respective integral length scale calculations are presented in tables 5 to 7.

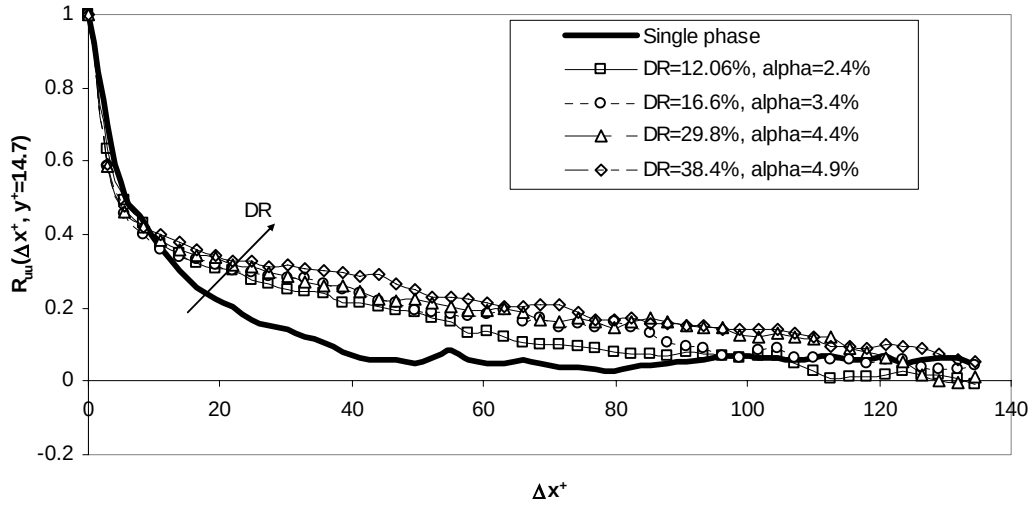

FIGURE 12. Two-point correlation coefficient in the longitudinal direction at $y^+ = 14.7$ for streamwise fluctuating velocity.

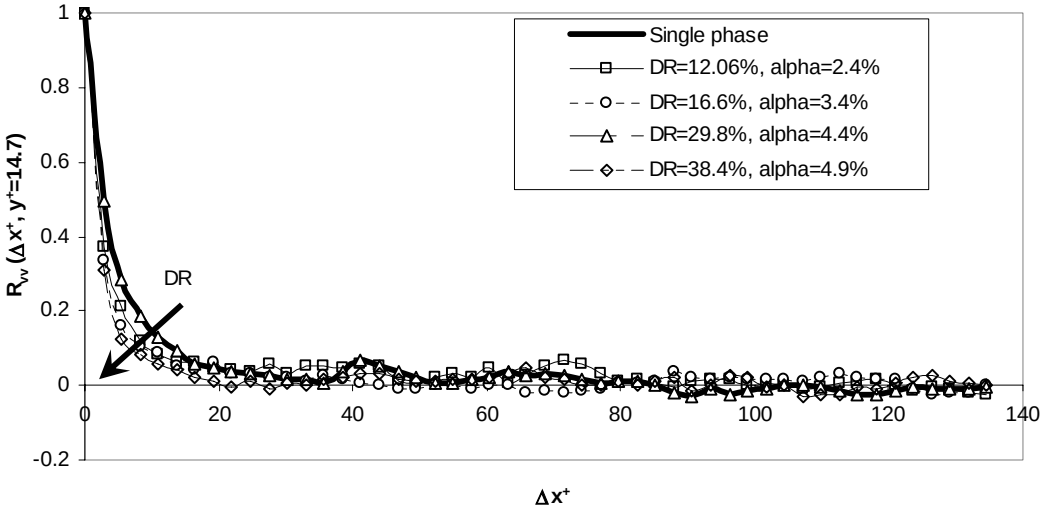

FIGURE 13. Two-point correlation coefficient in the longitudinal direction at $y^+ = 14.7$ for normal fluctuating velocity.

Longitudinal direction ($y^+ = 14.7$)	Single phase	DR=12.06%, α=2.4%	DR=16.6%, α=3.4%	DR=29.8%, α=4.4%	DR=38.4%, α=4.9%
L_{uu} [mm]	1.41	1.88	2.17	2.37	2.60
L_{vv} [mm]	0.54	0.50	0.32	0.30	0.22

TABLE 5. Integral length scales from longitudinal two-point correlation coefficients at $y^+ = 14.7$

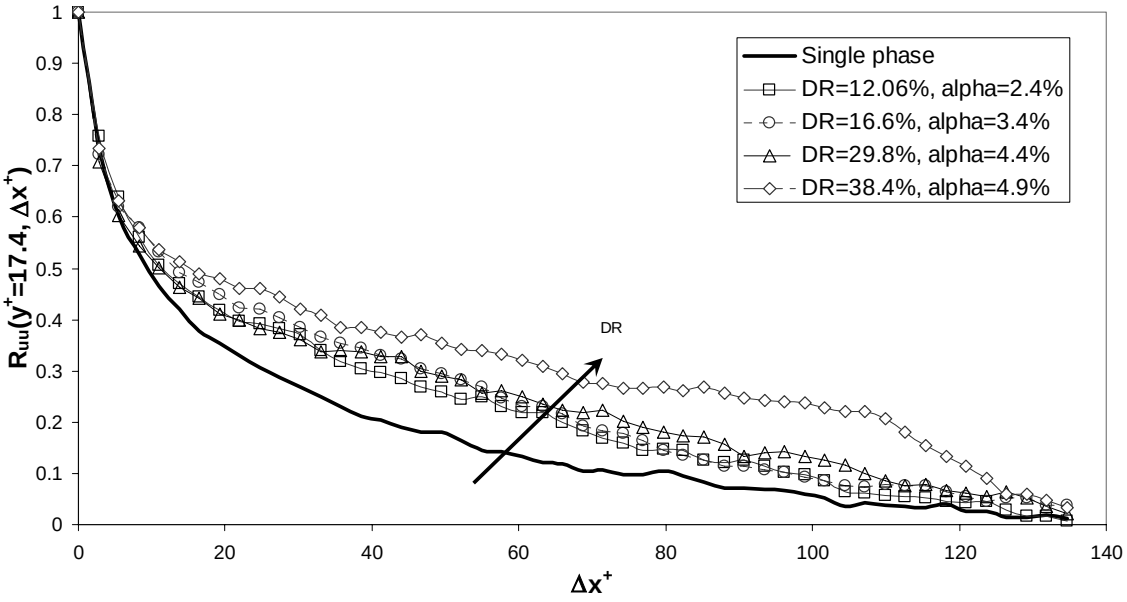

FIGURE 14. Two-point correlation coefficient in the longitudinal direction at $y^+ = 17.4$ for streamwise fluctuating velocity.

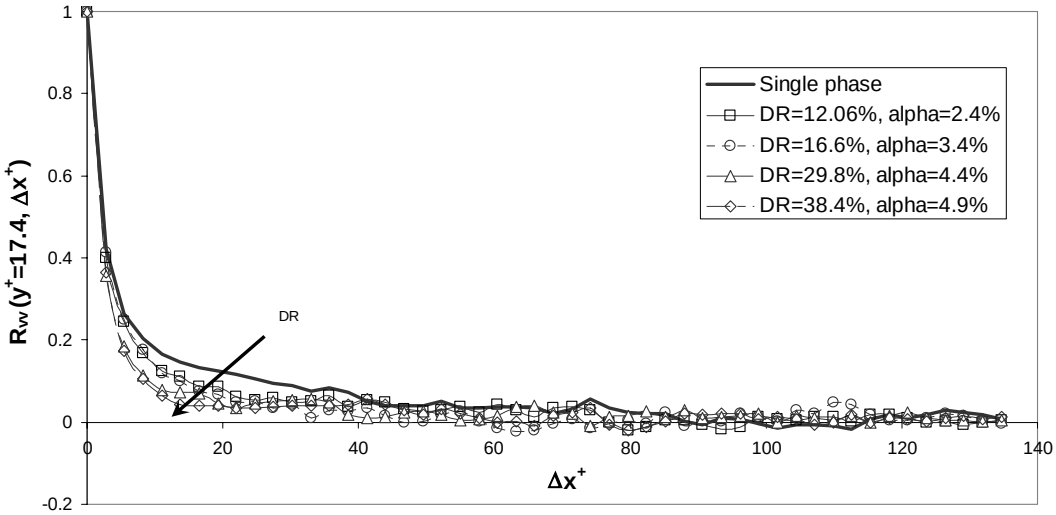

FIGURE 15. Two-point correlation coefficient in the longitudinal direction at y^+ = 17.4 for normal fluctuating velocity.

Longitudinal direction (y^+ = 17.4)	Single phase	DR=12.06%, α=2.4%	DR=16.6%, α=3.4%	DR=29.8%, α=4.4%	DR=38.4%, α=4.9%
L_{uu} [mm]	2.05	2.65	2.82	2.88	3.62
L_{vv} [mm]	0.72	0.50	0.44	0.42	0.39

TABLE 6. Integral length scales from longitudinal two-point correlation coefficients at y^+ = 17.4

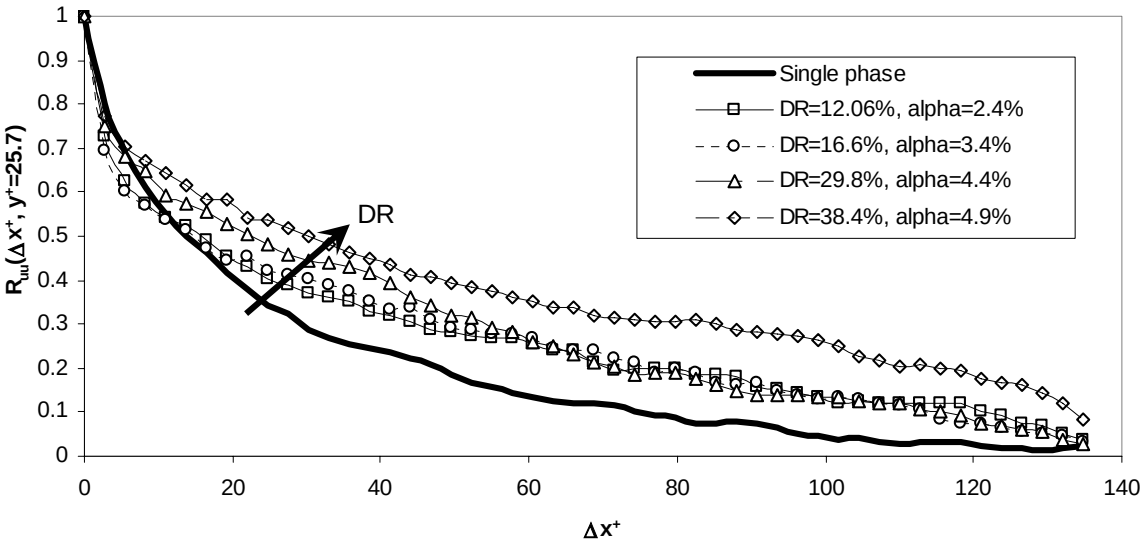

FIGURE 16. Two-point correlation coefficient in the longitudinal direction at $y^+ = 25.7$ for streamwise fluctuating velocity.

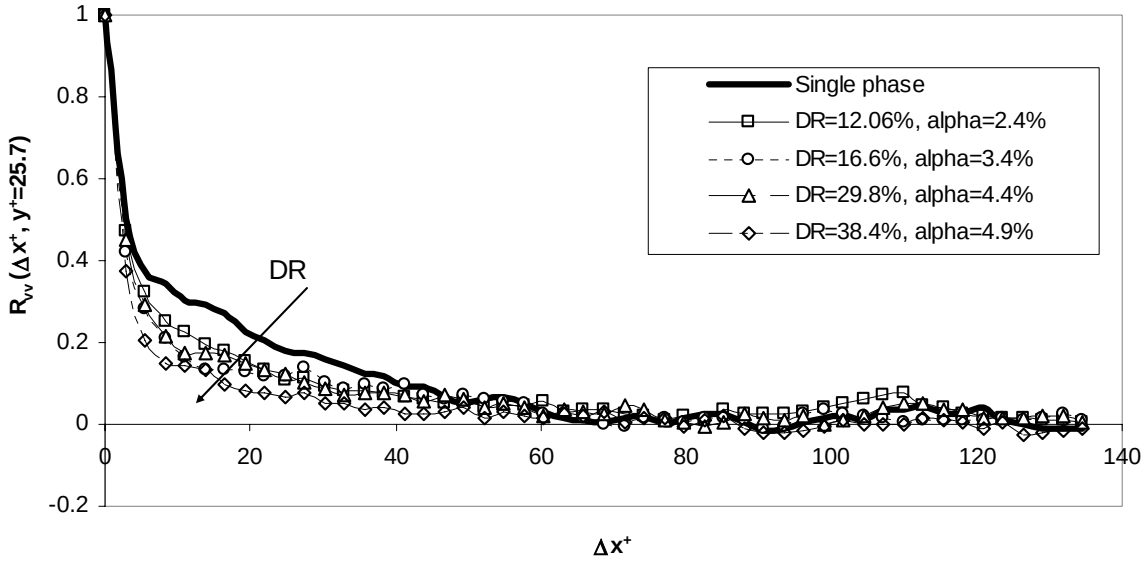

FIGURE 17. Two-point correlation coefficient in the longitudinal direction at $y^+ = 25.7$ for normal fluctuating velocity.

Longitudinal direction ($y^+ = 25.7$)	Single phase	DR=12.06%, α=2.4%	DR=16.6%, α=3.4%	DR=29.8%, α=4.4%	DR=38.4%, α=4.9%
L_{uu} [mm]	2.23	3.04	3.06	3.28	4.2
L_{vv} [mm]	1.04	0.96	0.76	0.73	0.53

TABLE 7. Integral length scales from longitudinal two-point correlation coefficients at $y^+ = 25.7$

The results observed for the values of the two-point correlation in these three locations within the buffer layer show the same tendency as the ones at $y^+ = 9.2$. There is a pronounced increase in the values of the two-point correlation in the longitudinal direction for the streamwise fluctuating velocity as the local void fraction increases, and therefore the drag reduction is increased. The opposite effect is observed for the two-point correlation values in the longitudinal direction calculated using the normal fluctuating velocity. In the latter case, there is a decrease for the two-point correlation values as the void fraction is increased. However, it can be observed that although these trends are preserved as the distance from the wall grows, there is an increase in the value of the integral length scale as the calculation location moves far away from the wall.

To investigate if this tendency was also found outside the buffer layer, the same calculations for the two-point correlation values in the longitudinal direction at $y^+ = 69.7$ for streamwise and normal velocity fluctuations were performed. These results are shown in figures 18 and 17. The respective integral length scale calculations are presented in table 8.

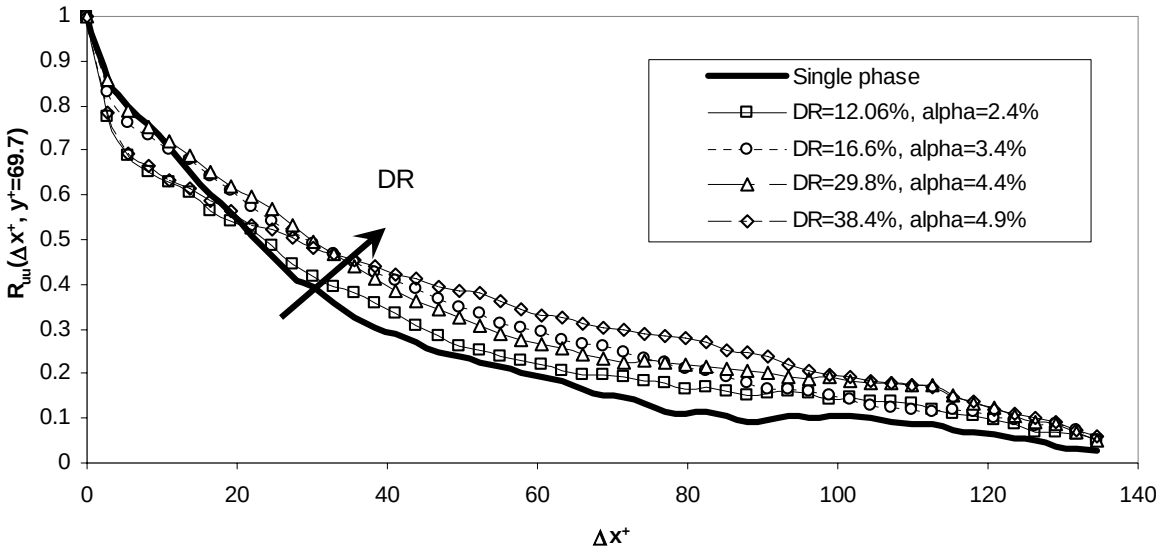

FIGURE 18. Two-point correlation coefficient in the longitudinal direction at $y^+ = 69.7$ for streamwise fluctuating velocity.

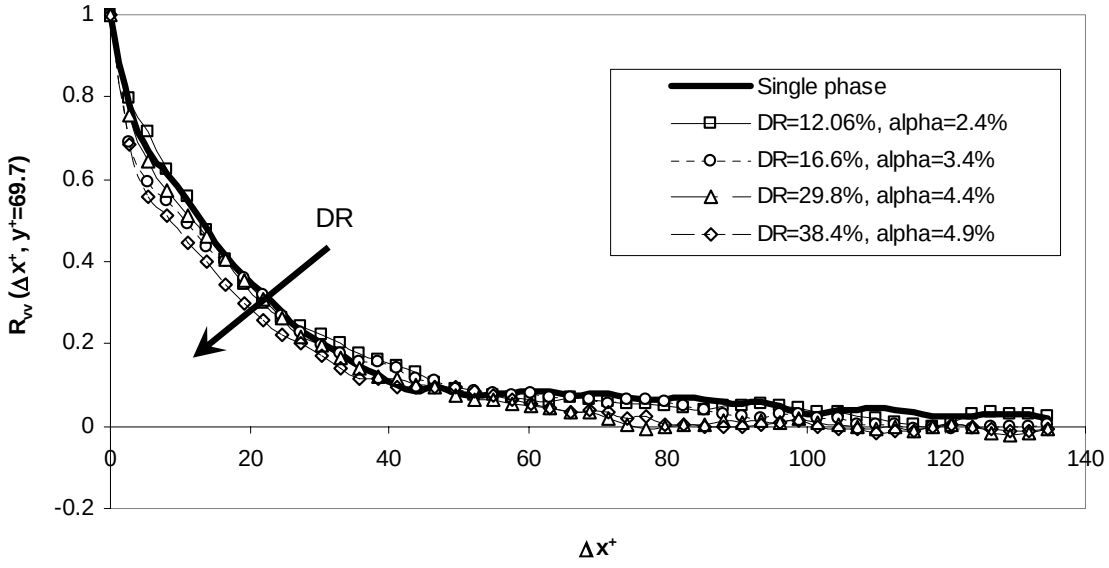

FIGURE 19. Two-point correlation coefficient in the longitudinal direction at $y^+ = 69.7$ for normal fluctuating velocity.

Longitudinal direction ($y^+ = 69.7$)	Single phase	DR=12.06%, α=2.4%	DR=16.6%, α=3.4%	DR=29.8%, α=4.4%	DR=38.4%, α=4.9%
L_{uu} [mm]	3.2	3.6	3.7	3.8	3.9
L_{vv} [mm]	1.81	1.74	1.61	1.45	1.33

TABLE 8. Integral length scales from longitudinal two-point correlation coefficients at $y^+ = 69.7$

Outside the buffer layer, at $y^+ = 69.7$, a large growth in the values of the integral length scale values is observed. However, the same trends tendencies prevail: an increase in the integral length scale for the streamwise velocity as the local void fraction is increased and a decrease in the length scale for the normal velocity with an increase in the local void fraction.

To investigate the changes in the values of the two-point correlation coefficient values in the transversal (normal) direction, calculation were carried out at different positions in the x-direction. These results are shown in figures 20 to 27, and the values for the integral length scales calculated are shown in tables 9 to 12.

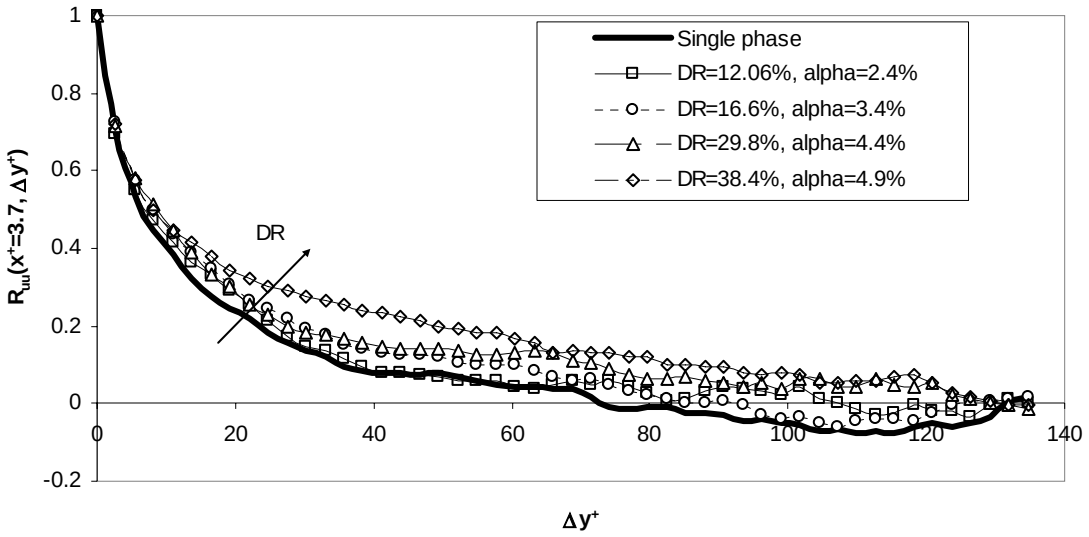

FIGURE 20. Two-point correlation coefficient in the transverse direction at $x^+ = 3.7$ for streamwise fluctuating velocity.

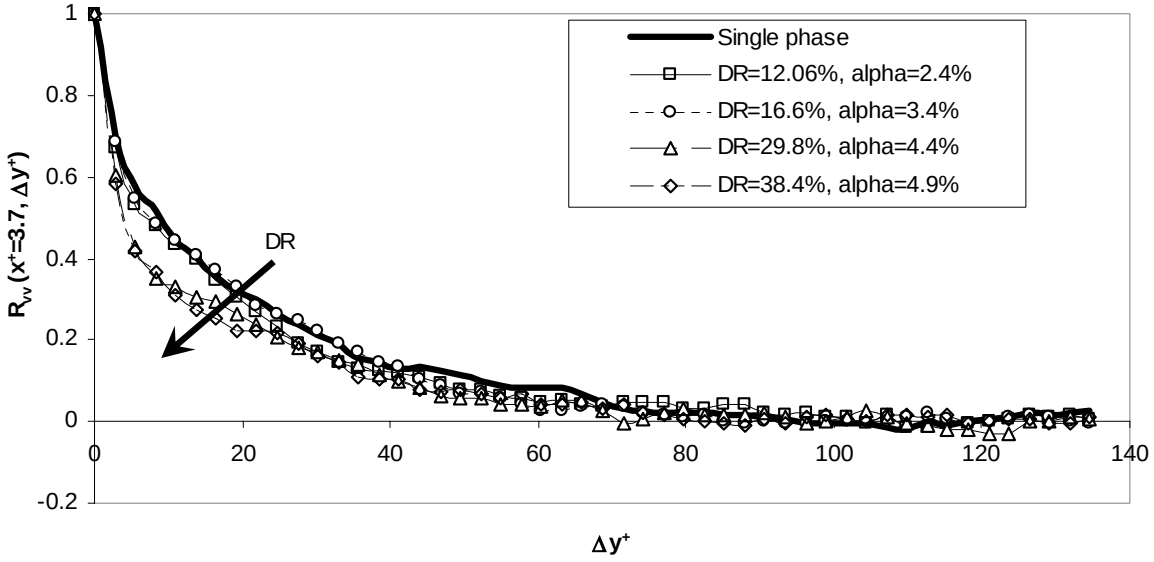

FIGURE 21. Two-point correlation coefficient in the transverse direction at $x^+ = 3.7$ for normal fluctuating velocity.

Transverse direction ($y^+ = 3.7$)	Single phase	DR=12.06%, α=2.4%	DR=16.6%, α=3.4%	DR=29.8%, α=4.4%	DR=38.4%, α=4.9%
L_{uu} [mm]	1.34	1.42	1.48	1.48	2.2
L_{vv} [mm]	1.5	1.4	1.39	1.13	1.1

TABLE 9. Integral length scales from transverse two-point correlation coefficients at $y^+ = 3.7$

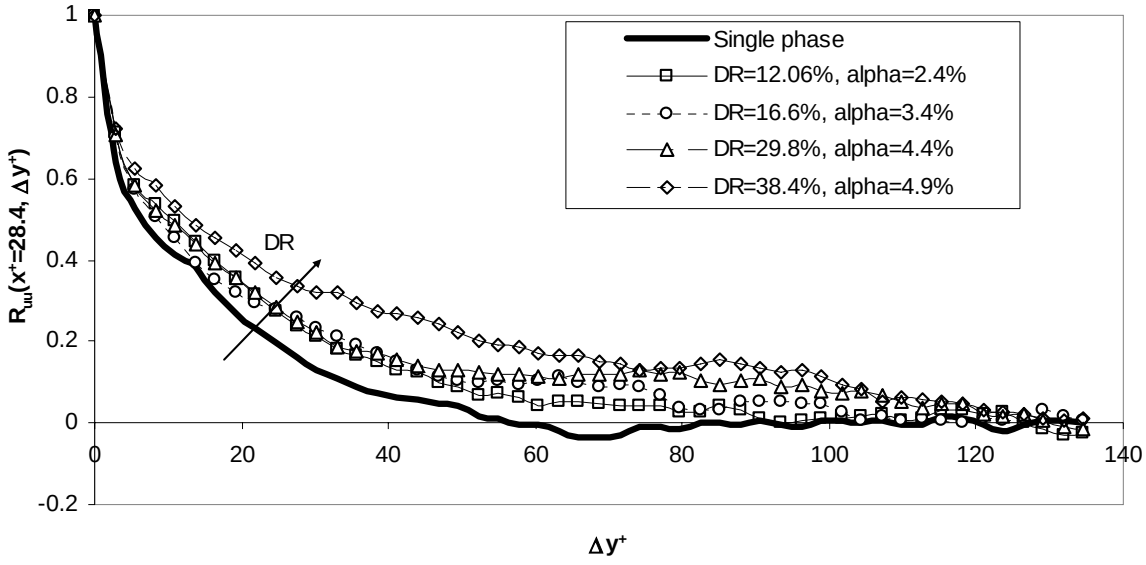

FIGURE 22. Two-point correlation coefficient in the transverse direction at $x^+ = 28.4$ for streamwise fluctuating velocity.

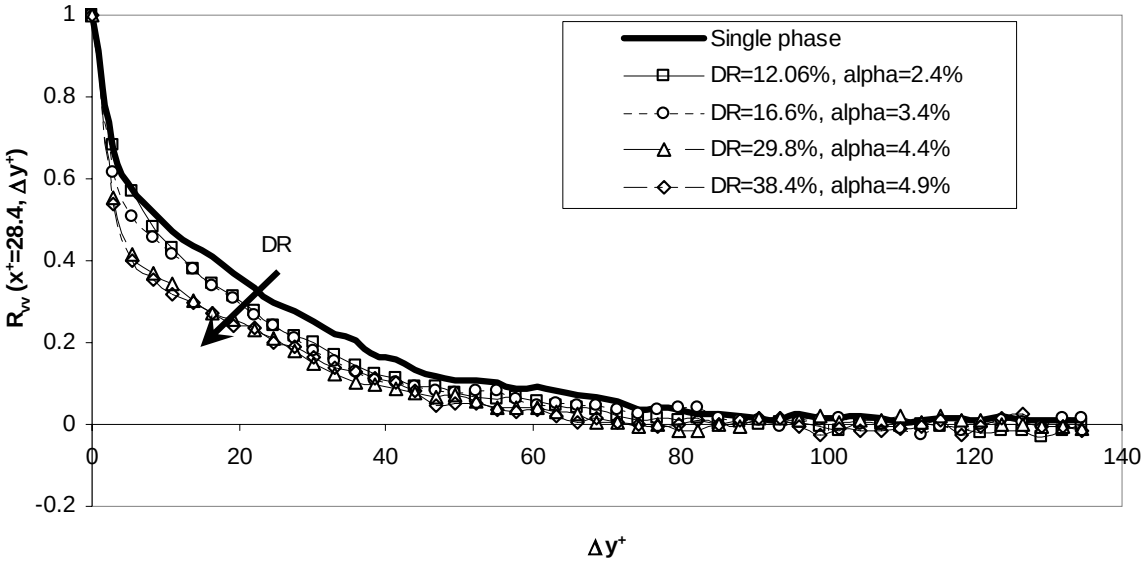

FIGURE 23. Two-point correlation coefficient in the transverse direction at $x^+ = 28.4$ for normal fluctuating velocity.

Transverse direction ($y^+ = 28.4$)	Single phase	DR=12.06%, α=2.4%	DR=16.6%, α=3.4%	DR=29.8%, α=4.4%	DR=38.4%, α=4.9%
L_{uu} [mm]	1.1	1.52	1.71	1.98	2.51
L_{vv} [mm]	1.68	1.33	1.32	1.06	1.03

TABLE 10. Integral length scales from transverse two-point correlation coefficients at $y^+ = 28.4$

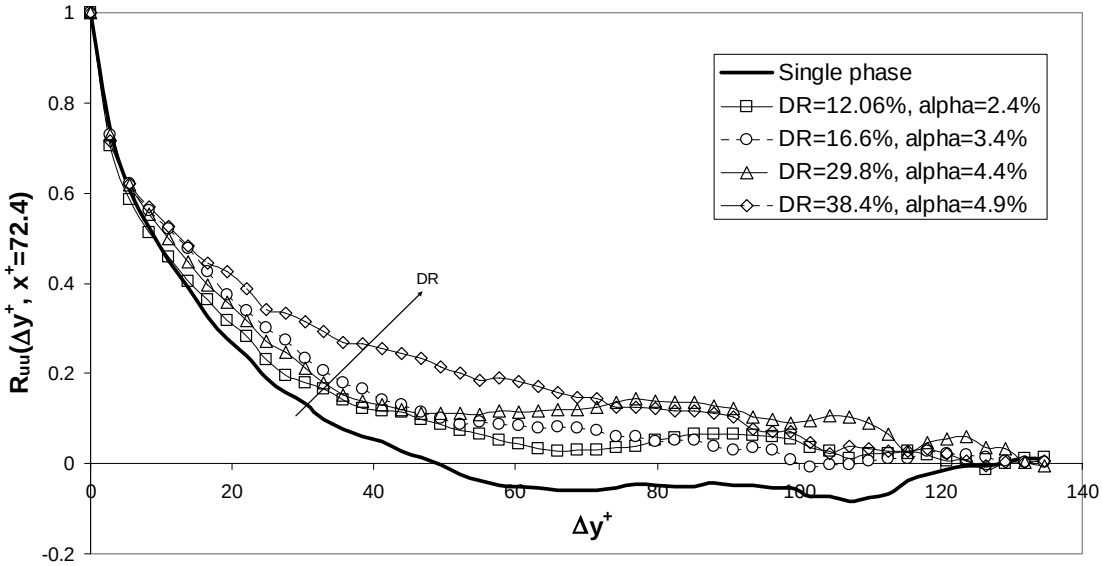

FIGURE 24. Two-point correlation coefficient in the transverse direction at $x^+ = 72.4$ for streamwise fluctuating velocity.

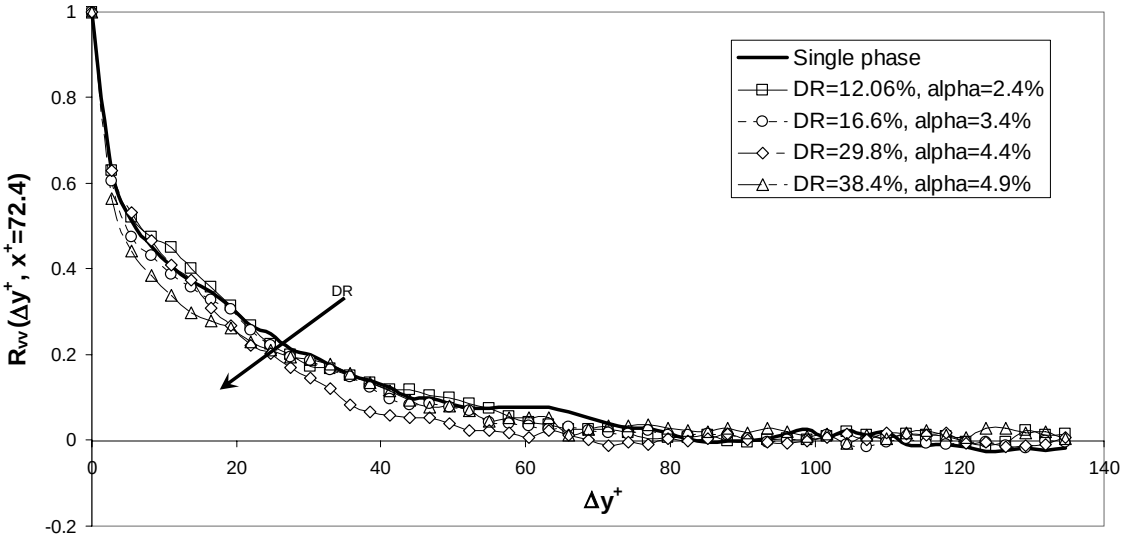

FIGURE 25. Two-point correlation coefficient in the transverse direction at $x^+ = 72.4$ for normal fluctuating velocity.

Transverse direction ($y^+ = 72.4$)	Single phase	DR=12.06%, α=2.4%	DR=16.6%, α=3.4%	DR=29.8%, α=4.4%	DR=38.4%, α=4.9%
L_{uu} [mm]	1.07	1.52	1.71	2.07	2.26
L_{vv} [mm]	1.36	1.32	1.24	1.22	1.02

TABLE 11. Integral length scales from transverse two-point correlation coefficients at $y^+ = 72.4$

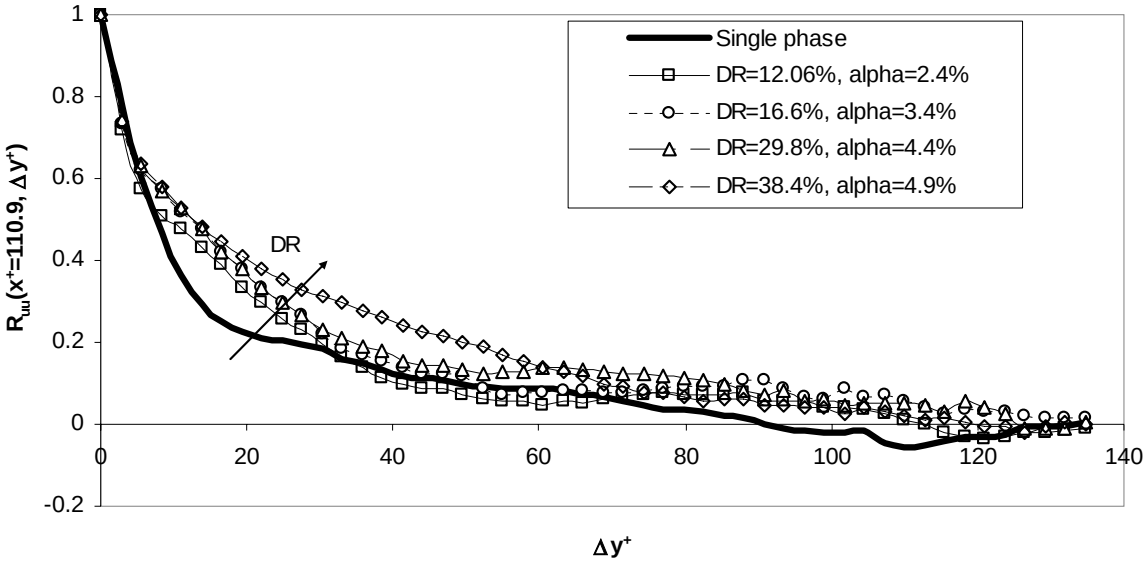

FIGURE 26. Two-point correlation coefficient in the transverse direction at $x^+ = 110.9$ for streamwise fluctuating velocity.

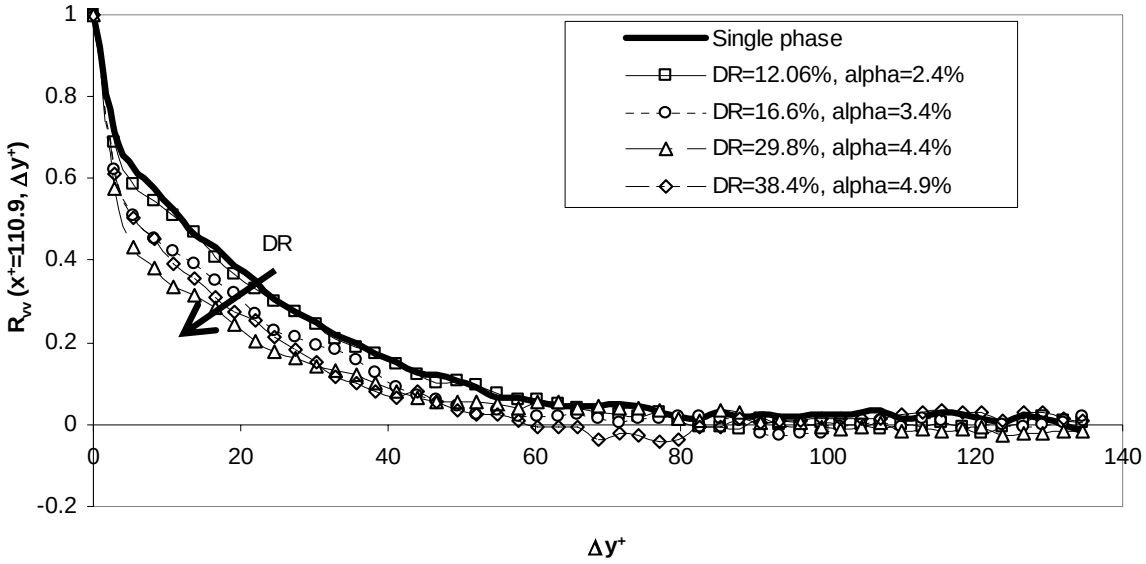

FIGURE 27. Two-point correlation coefficient in the transverse direction at $x^+ = 110.9$ for normal fluctuating velocity.

Transverse direction ($y^+ = 110.9$)	Single phase	DR=12.06%, α=2.4%	DR=16.6%, α=3.4%	DR=29.8%, α=4.4%	DR=38.4%, α=4.9%
L_{uu} [mm]	1.36	1.58	1.93	2.04	2.12
L_{vv} [mm]	1.71	1.53	1.24	1.12	1.07

TABLE 12. Integral length scales from transverse two-point correlation coefficients at $y^+ = 110.9$

It is observed that the length scale for the streamwise fluctuating velocity increases as the local value of void fraction increases. However, the length scale for the normal fluctuating velocity decreases as an increase in the local void fraction is observed. A

noteworthy characteristic of these results is that as the position in the streamwise direction is changed, there is no significant change in the magnitude of the length scale as it was observed for the longitudinal calculations. This is a good indicator of the fully developed nature of the flow.

Two-point correlation coefficient calculations were also performed in various directions with different inclinations to the wall of angles of 18.5°, 26.5°, 45°, 63.5°, and 71.5°; where $\tan\theta = \Delta x/\Delta y$, Δr is the spacing between two points and is equal to $\Delta x/\cos\theta$. Figure 28 shows a scheme of the angle used to calculate the correlation in the full velocity field obtained from PIV. The results obtained for two-point correlation coefficients for the 5 different angles are shown in figures 29 to 38 whereas results for the calculated length scales are shown in tables 13 to 17.

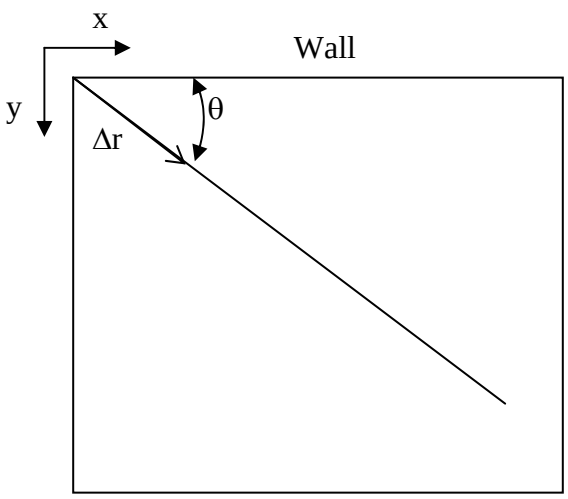

FIGURE 28. Direction of angular two-point correlation coefficients calculation.

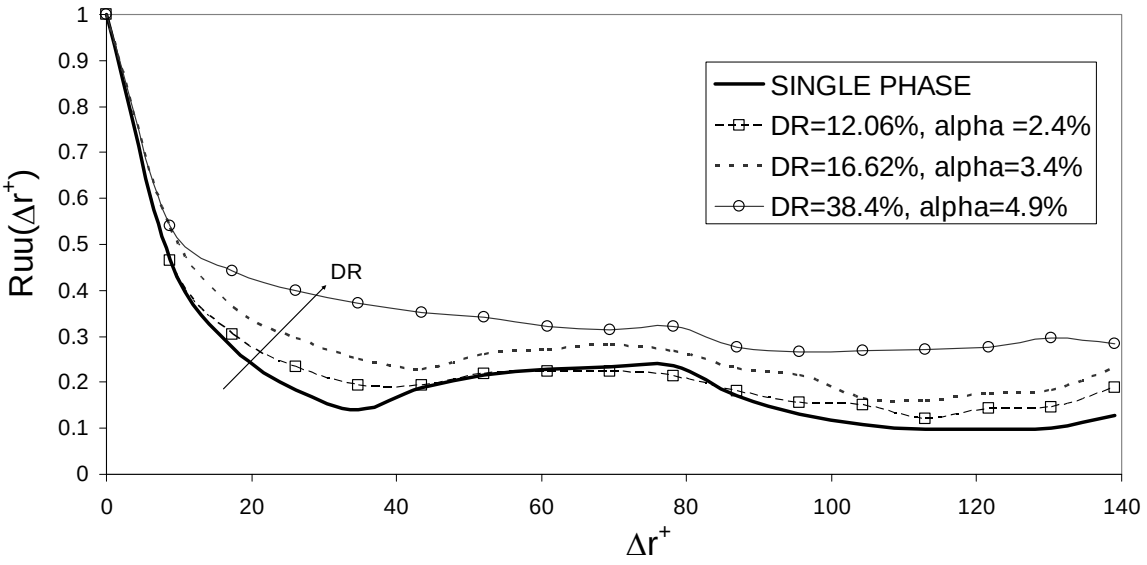

FIGURE 29. Two-point correlation coefficient at θ = 18.5°for streamwise fluctuating velocity.

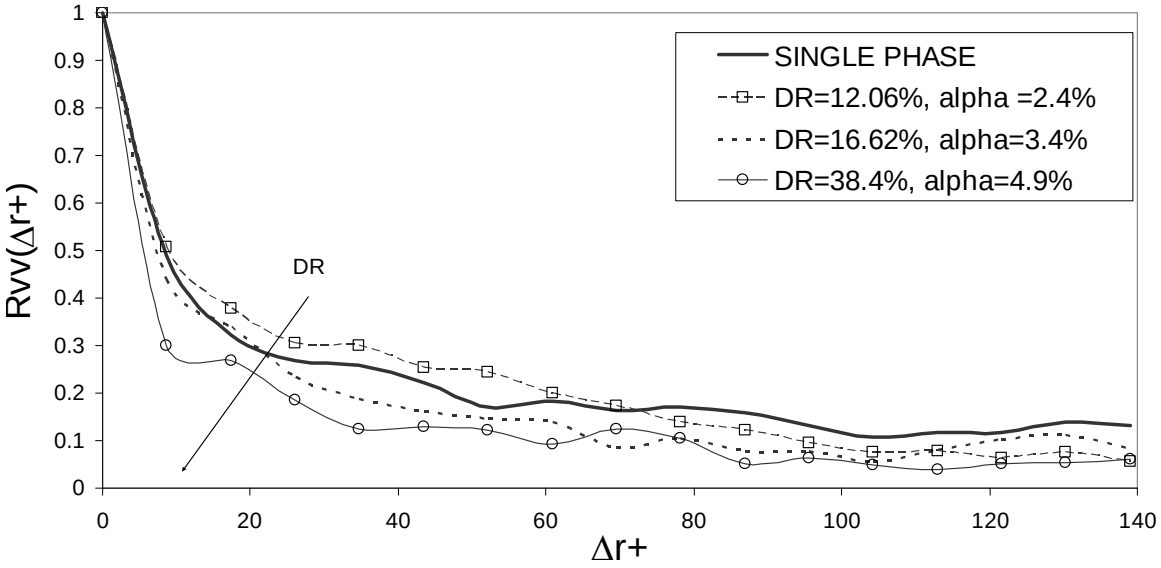

FIGURE 30. Two-point correlation coefficient at θ = 18.5°for normal fluctuating velocity.

θ = 18.5°	Single phase	DR=12.06%, α=2.4%	DR=16.6%, α=3.4%	DR=38.4%, α=4.9%
L_{uu} [mm]	1.69	2.33	2.89	3.65
L_{vv} [mm]	1.42	1.41	1.12	1.02

TABLE 13. Integral length scales from angular two-point correlation coefficients at θ = 18.5°

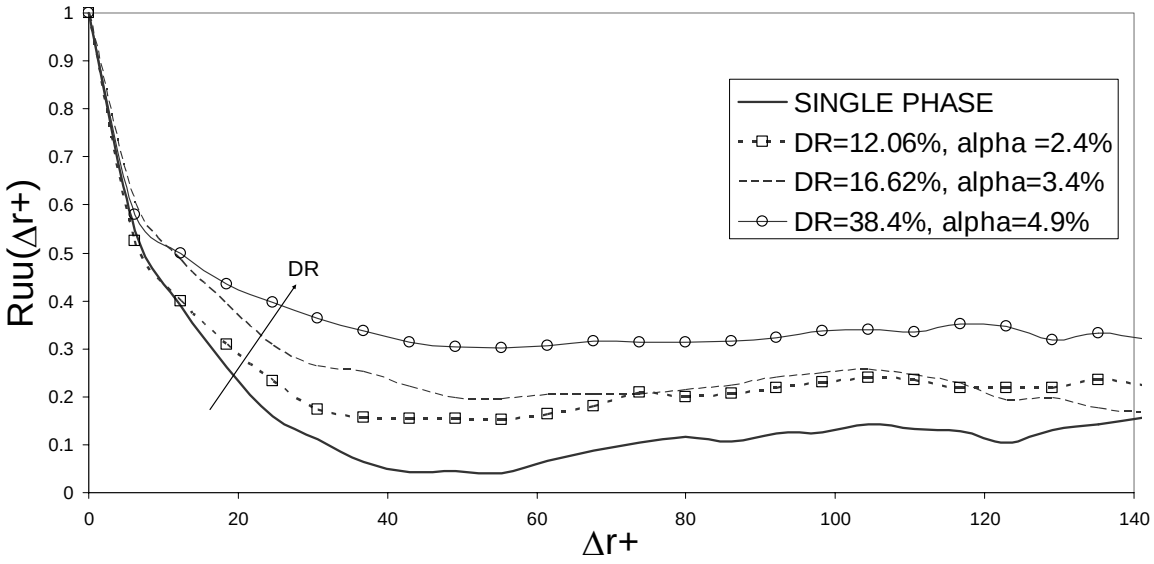

FIGURE 31. Two-point correlation coefficient at θ = 26.5°for streamwise fluctuating velocity.

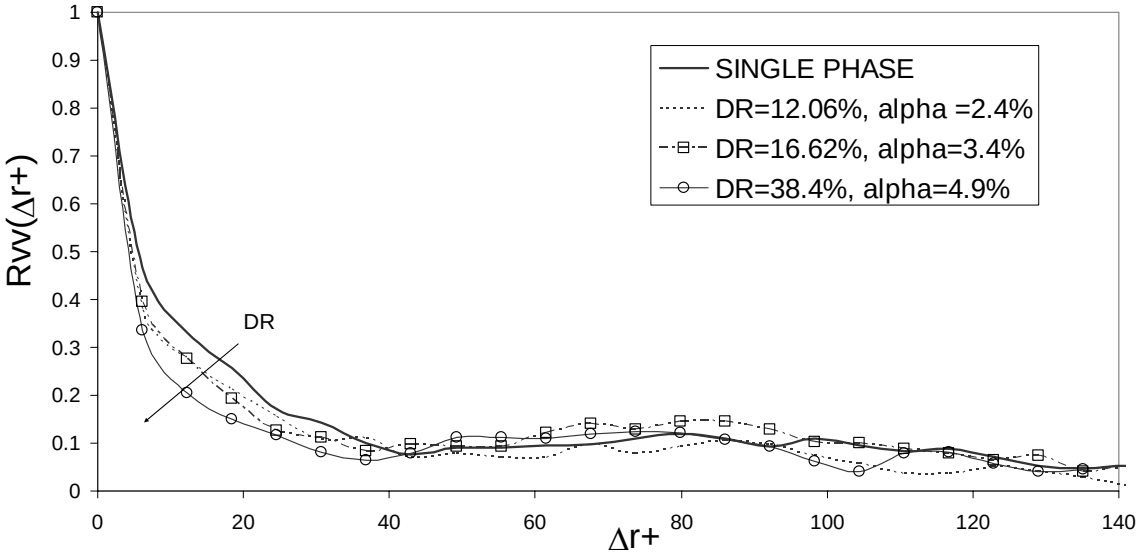

FIGURE 32. Two-point correlation coefficient at θ = 26.5°for normal fluctuating velocity.

θ = 26.5°	Single phase	DR=12.06%, α=2.4%	DR=16.6%, α=3.4%	DR=38.4%, α=4.9%
L_{uu} [mm]	1.85	2.50	2.95	3.94
L_{vv} [mm]	1.76	1.72	1.69	1.54

TABLE 14. Integral length scales from angular two-point correlation coefficients at θ = 26.5°

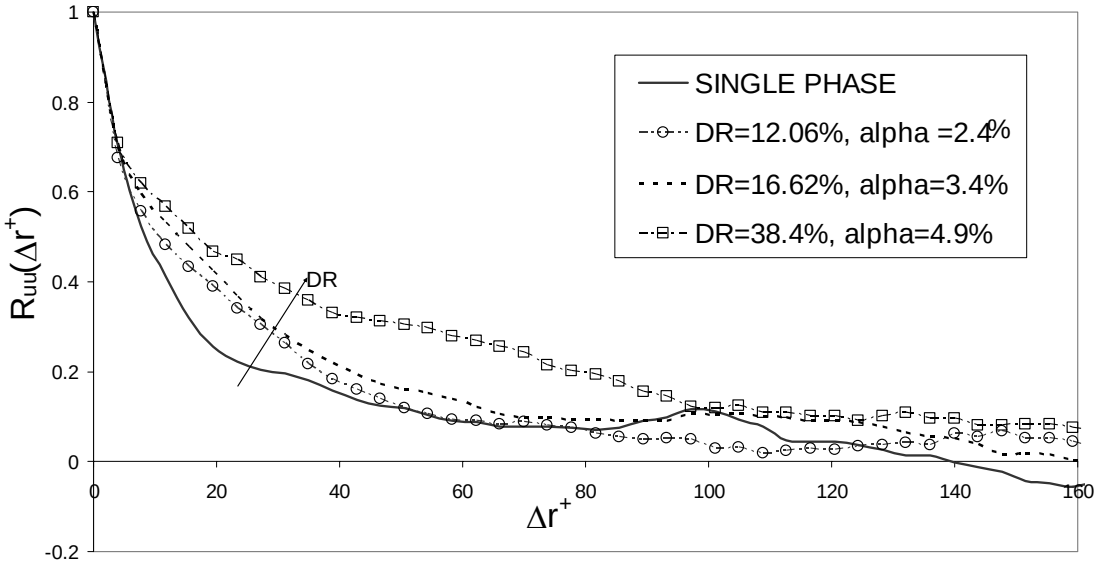

FIGURE 33. Two-point correlation coefficient at θ = 45°for streamwise fluctuating velocity.

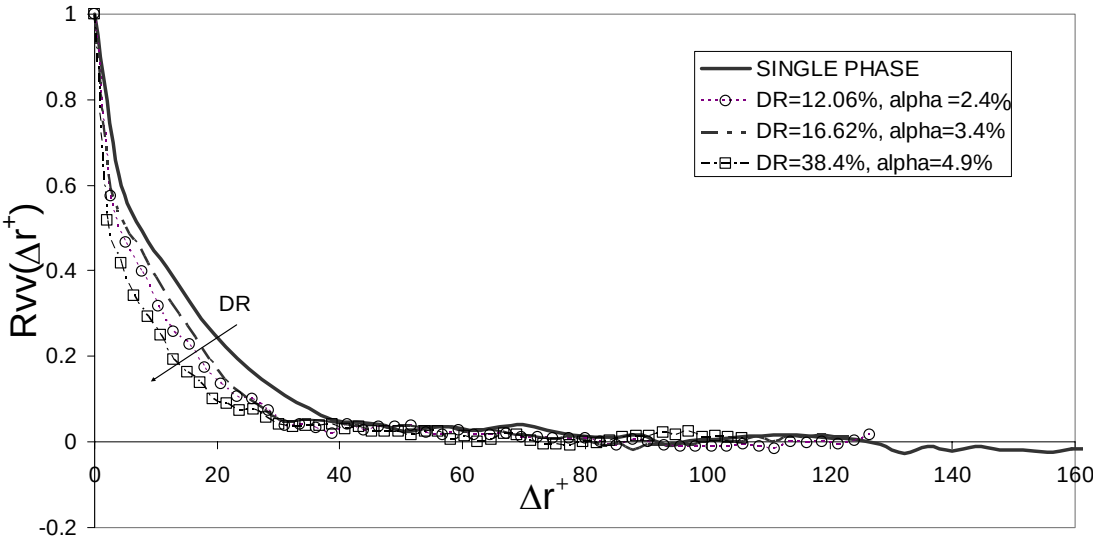

FIGURE 34. Two-point correlation coefficient at θ = 45°for normal fluctuating velocity.

θ = 45°	Single phase	DR=12.06%, α=2.4%	DR=16.6%, α=3.4%	DR=38.4%, α=4.9%
L_{uu} [mm]	1.87	2.12	2.51	3.56
L_{vv} [mm]	1.48	1.47	1.27	1.23

TABLE 15. Integral length scales from angular two-point correlation coefficients at θ = 45°

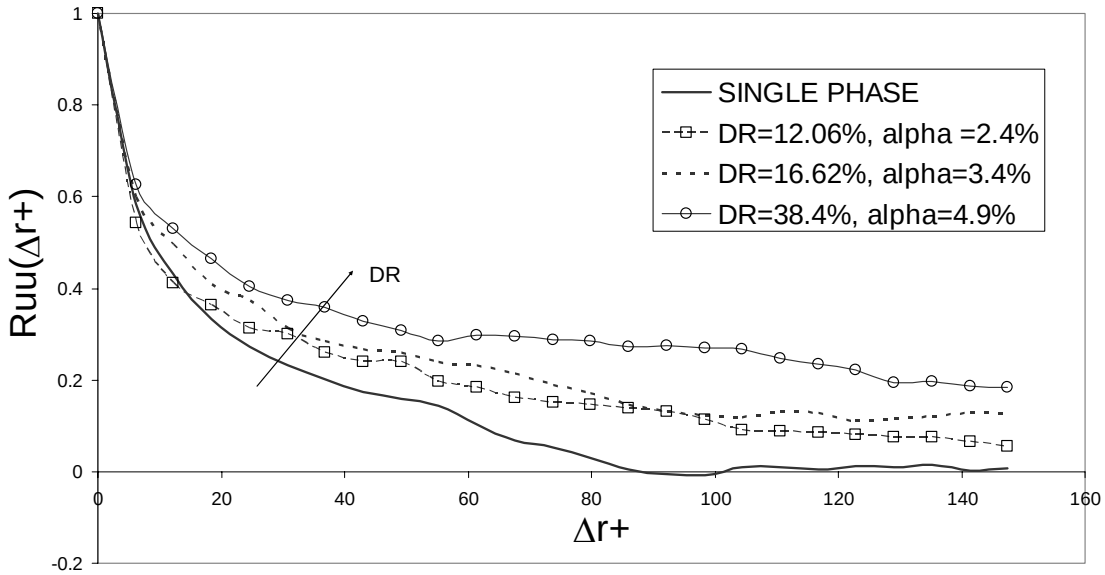

FIGURE 35. Two-point correlation coefficient at θ = 63.5°for streamwise fluctuating velocity.

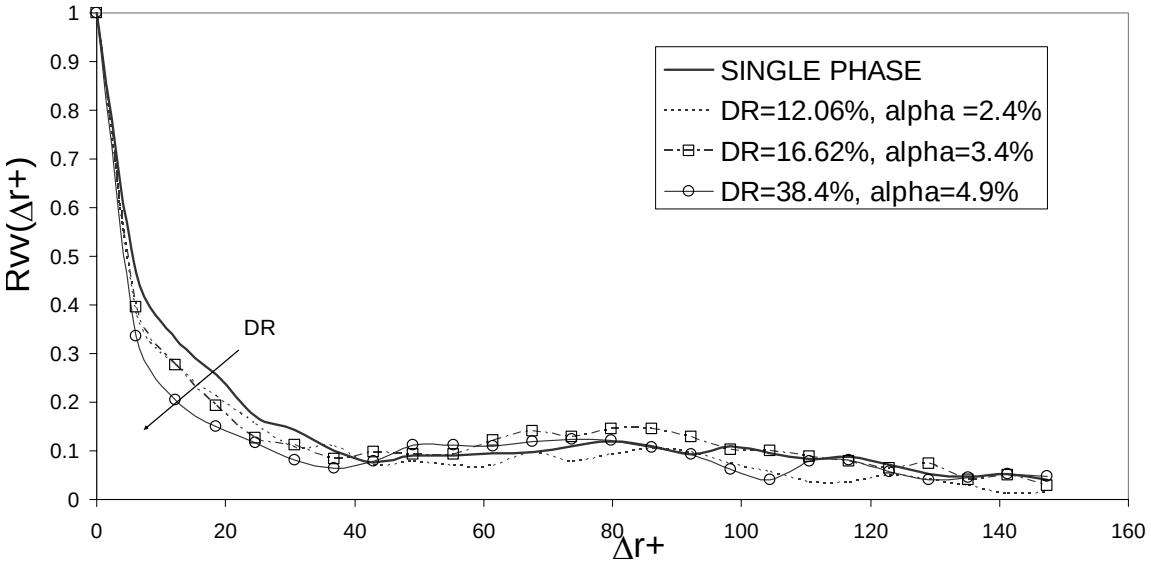

FIGURE 36. Two-point correlation coefficient at θ = 63.5°for normal fluctuating velocity.

θ = 63.5°	Single phase	DR=12.06%, α=2.4%	DR=16.6%, α=3.4%	DR=38.4%, α=4.9%
L_{uu} [mm]	1.96	2.93	3.28	4.41
L_{vv} [mm]	1.83	1.73	1.60	1.55

TABLE 16. Integral length scales from angular two-point correlation coefficients at θ = 63.5°

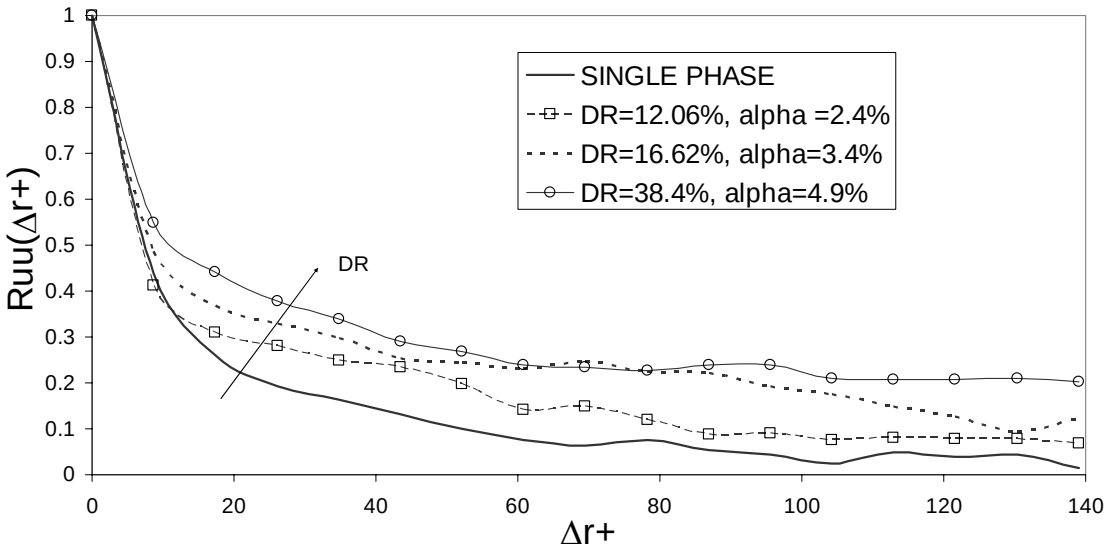

FIGURE 37. Two-point correlation coefficient at θ = 71.5°for streamwise fluctuating velocity.

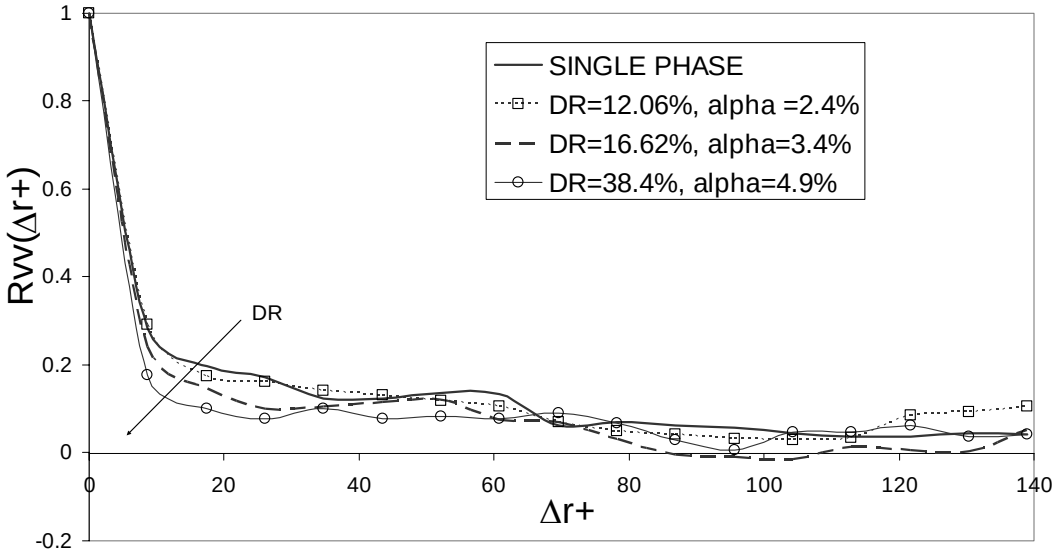

FIGURE 38. Two-point correlation coefficient at θ = 71.5°for normal fluctuating velocity.

$\theta = 71.5°$	Single phase	DR=12.06%, α=2.4%	DR=16.6%, α=3.4%	DR=38.4%, α=4.9%
L_{uu} [mm]	2.57	2.81	3.37	4.27
L_{vv} [mm]	2.49	2.44	1.99	1.53

TABLE 17. Integral length scales from angular two-point correlation coefficients at $\theta = 71.5°$

A growth in the integral length scale for the streamwise fluctuating velocity is also observed in the calculations made following different inclinations to the wall when the local void fraction increases. A decrease in the integral length scale for the normal fluctuating velocity is also observed. These trends are consistent with the results obtained from the two-point correlation coefficient in the longitudinal and transverse directions. All these results make it clear that the presence of microbubbles alters the length scales within the boundary layer. This lead directly to changes in the shape of the energy containing eddies. These changes in the organized structures located within the boundary layer reinforce the idea of a decorrelation of u' and v' as the source of the decrease of the Reynolds stresses. Moreover, the fact that streamwise and normal turbulent intensities increase as the local void fraction increases demonstrates that the decrease in the magnitude of the Reynolds stresses is not caused by a simple decrease in the magnitude of the turbulent intensities of one or both of the fluctuating velocity components.

4.5 Autocorrelation Coefficients

To elucidate the changes that the presence of microbubbles produces in the integral time scale, autocorrelation coefficients were calculated at different positions within the boundary layer. Figures 39 to 49 show the autocorrelation function calculated at different positions, mainly within the buffer layer, for streamwise and normal fluctuating velocities. The corresponding integral time scales calculated from these autocorrelation results are shown in tables 18 to 21.

A modification in the time scales is also found in the presence of microbubbles. An increase in the time scale is observed for streamwise velocity when microbubbles are injected. On the contrary, for the normal fluctuating velocity, the time scale obtained from the autocorrelation results is decreased as microbubbles are injected.

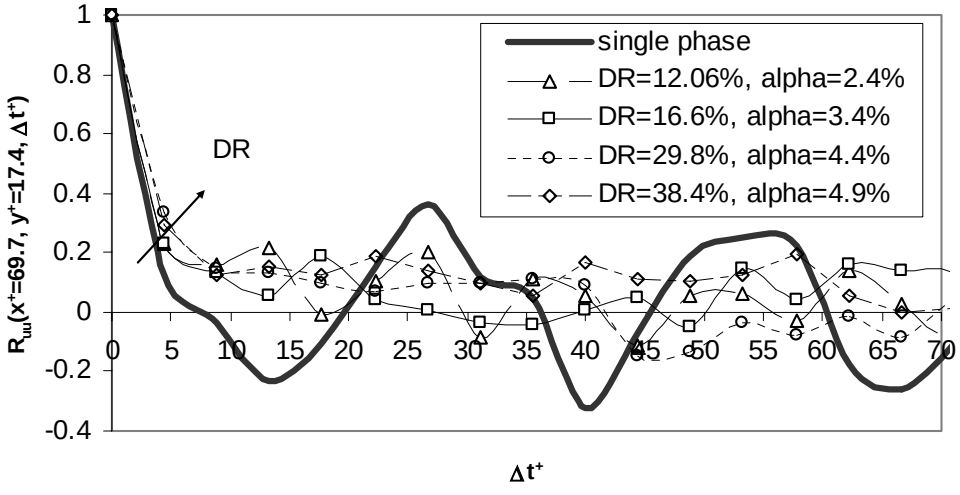

FIGURE 39. Autocorrelation coefficient at $x^+ = 69.7$, $y^+ = 17.4$ for streamwise fluctuating velocity.

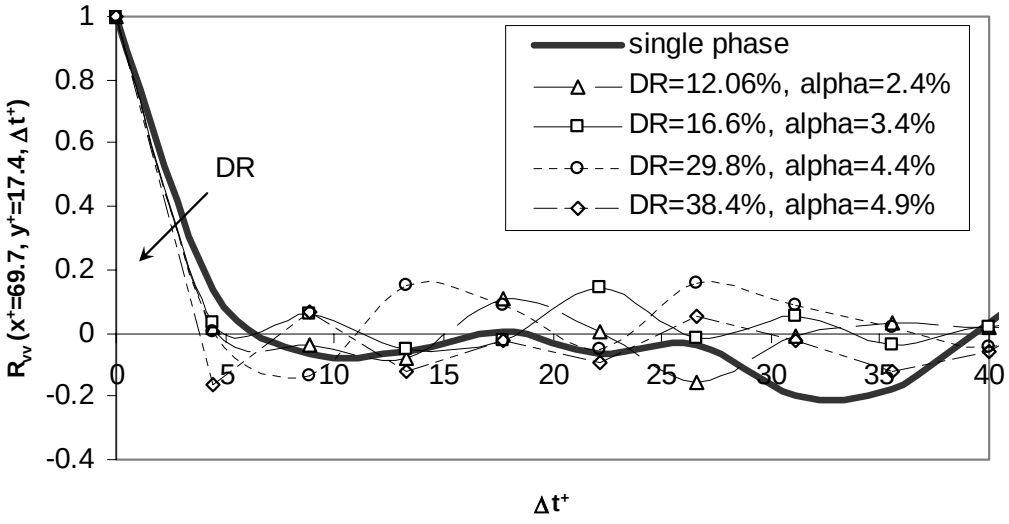

FIGURE 40. Autocorrelation coefficient at $x^+ = 69.7$, $y^+ = 17.4$ for normal fluctuating velocity.

($x^+ = 69.7$, $y^+ = 17.4$)	Single phase	DR=12.06%, α=2.4%	DR=16.6%, α=3.4%	DR=29.8%, α=4.4%	DR=38.4%, α=4.9%
T_{Lu} [s]	0.012	0.028	0.030	0.047	0.072
T_{Lv} [s]	0.011	0.009	0.008	0.007	0.005

TABLE 18. Integral time scales from autocorrelation coefficients at $x^+ = 69.7$, $y^+ = 17.4$

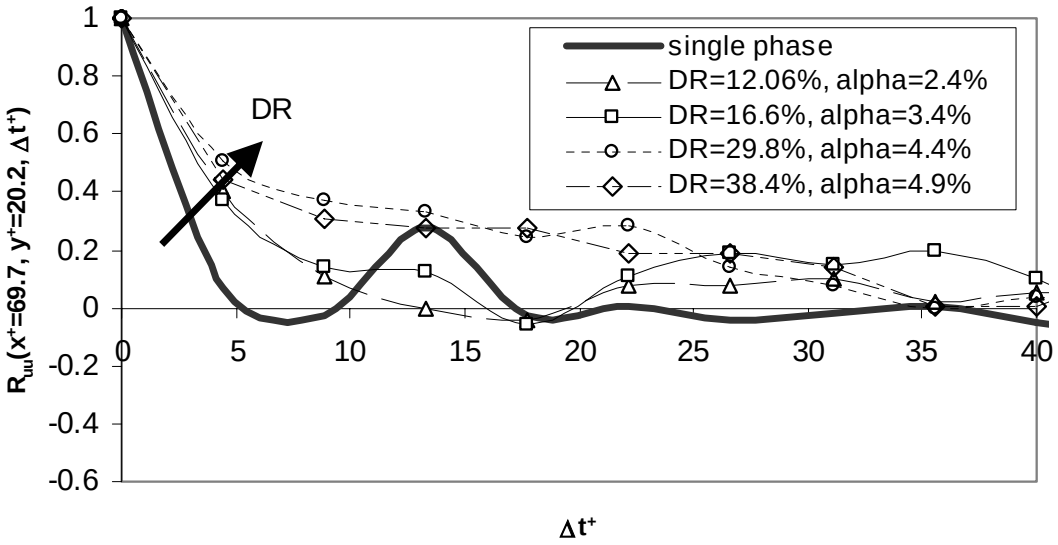

FIGURE 41. Autocorrelation coefficient at $x^+ = 69.7$, $y^+ = 20.2$ for streamwise fluctuating velocity.

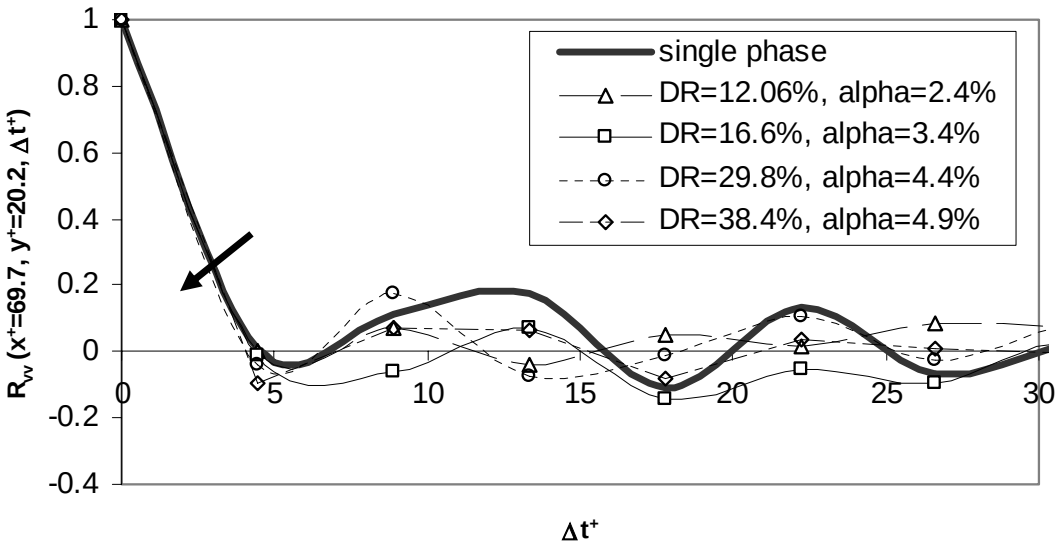

FIGURE 42. Autocorrelation coefficient at $x^+ = 69.7$, $y^+ = 20.2$ for normal fluctuating velocity.

(x^+ = 69.7, y^+ = 20.2)	Single phase	DR=12.06%, α=2.4%	DR=16.6%, α=3.4%	DR=29.8%, α=4.4%	DR=38.4%, α=4.9%
T_{Lu} [s]	0.011	0.021	0.030	0.074	0.1
T_{Lv} [s]	0.017	0.01	0.009	0.006	0.005

TABLE 19. Integral time scales from autocorrelation coefficients at x^+ = 69.7, y^+ = 20.2

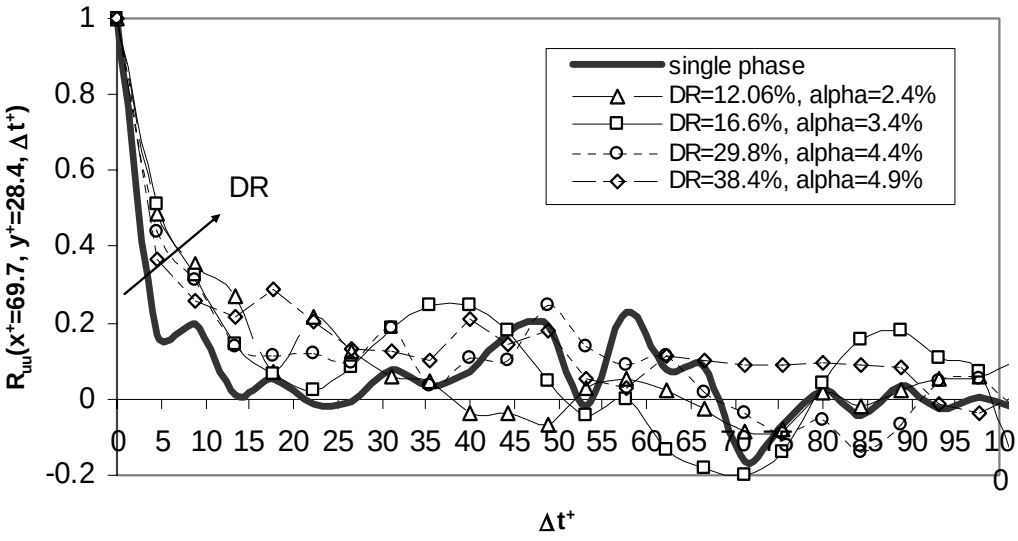

FIGURE 43. Autocorrelation coefficient at x^+ = 69.7, y^+ = 28.4 for streamwise fluctuating velocity.

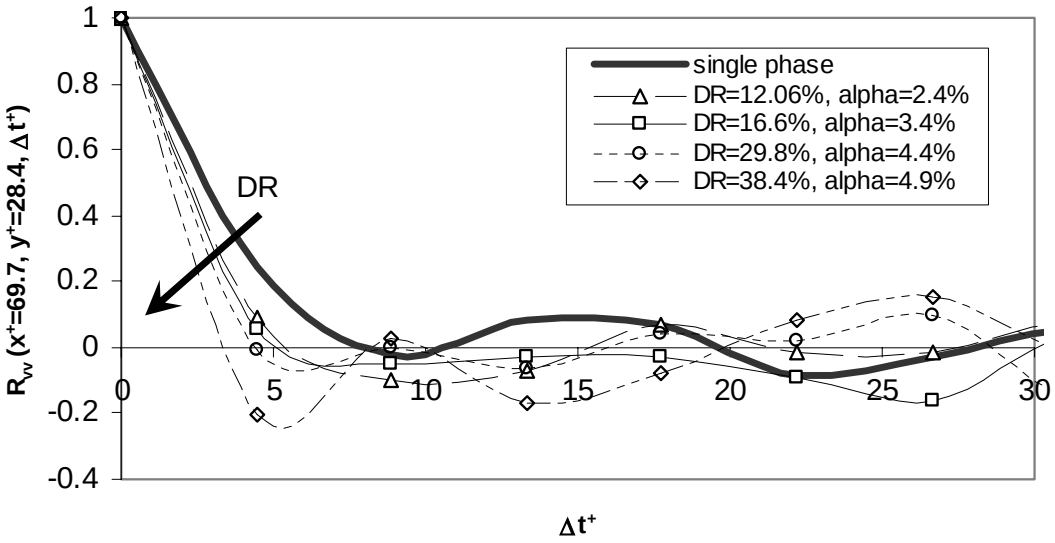

FIGURE 44. Autocorrelation coefficient at $x^+ = 69.7$, $y^+ = 28.4$ for normal fluctuating velocity.

($x^+ = 69.7$, $y^+ = 28.4$)	Single phase	DR=12.06%, α=2.4%	DR=16.6%, α=3.4%	DR=29.8%, α=4.4%	DR=38.4%, α=4.9%
T_{Lu} [s]	0.02	0.06	0.07	0.08	0.1
T_{Lv} [s]	0.015	0.01	0.009	0.008	0.004

TABLE 20. Integral time scales from autocorrelation coefficients at $x^+ = 69.7$, $y^+ = 28.4$

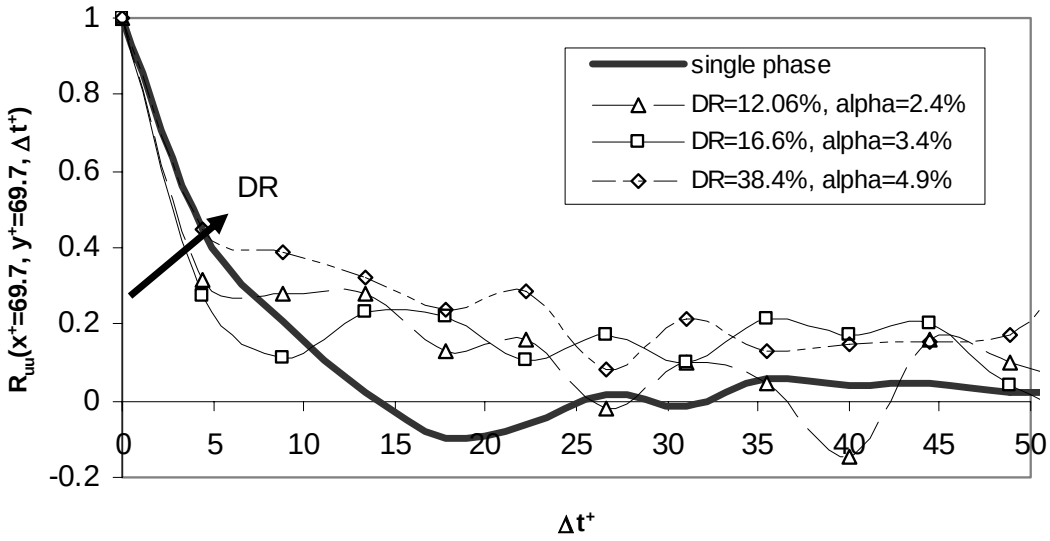

FIGURE 45. Autocorrelation coefficient at $x^+ = 69.7$, $y^+ = 69.7$ for streamwise fluctuating velocity.

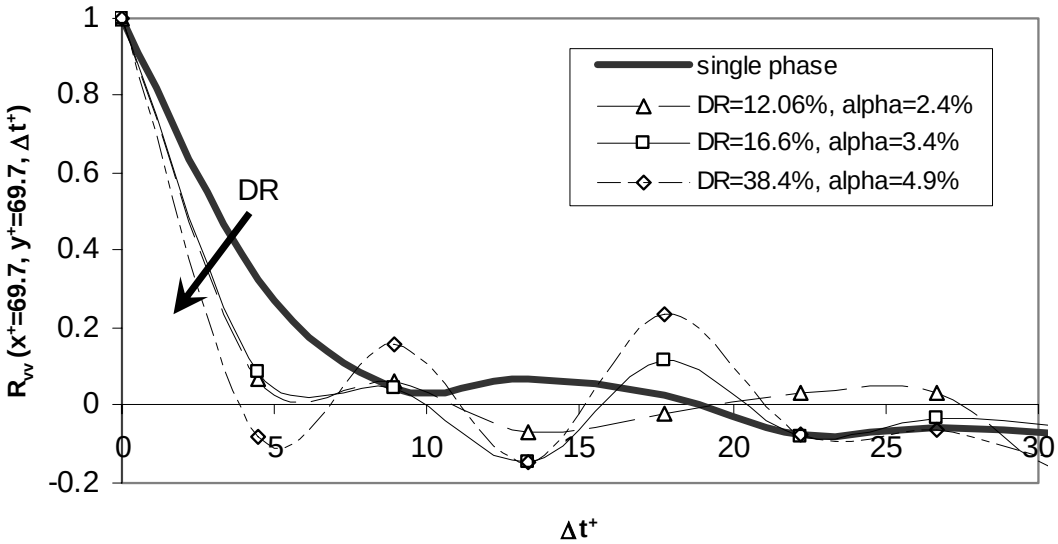

FIGURE 46. Autocorrelation coefficient at $x^+ = 69.7$, $y^+ = 69.7$ for normal fluctuating velocity.

(x^+ = 69.7, y^+ = 69.7)	Single phase	DR=12.06%, α=2.4%	DR=16.6%, α=3.4%	DR=29.8%, α=4.4%	DR=38.4%, α=4.9%
T_{Lu} [s]	0.028	0.046	0.07	0.103	0.13
T_{Lv} [s]	0.02	0.012	0.01	0.009	0.006

TABLE 21. Integral time scales from autocorrelation coefficients at x^+ = 69.7, y^+ = 69.7

4.6 Two-dimensional Two-point Correlation Coefficient

Two-dimensional correlation results were obtained in the x-y plane at two different (x,y) locations for u' and v'. These results were calculated for single phase flow and for the different cases of microbubbles presence within the boundary layer. Figures 47 to 66 show the changes produced by microbubbles presence at different local void fractions. The variation of the streamwise and the normal lenthscales, which are associated with the maximum widths (along the x- and y-directions, respectively) of the contours R_{uu} = 0.2 and R_{vv} = 0.2 obtained from the fluctuating velocity fields can be observed in those figures. The R-levels were selected as a reasonable value in order to focus on the large-scale events, as well as achieving better defined shapes for the correlation maps. It is observed that for the streamwise fluctuating velocity, the length scales in x and y direction increases when microbubbles are present. The opposite effect is observed for the normal velocity results.

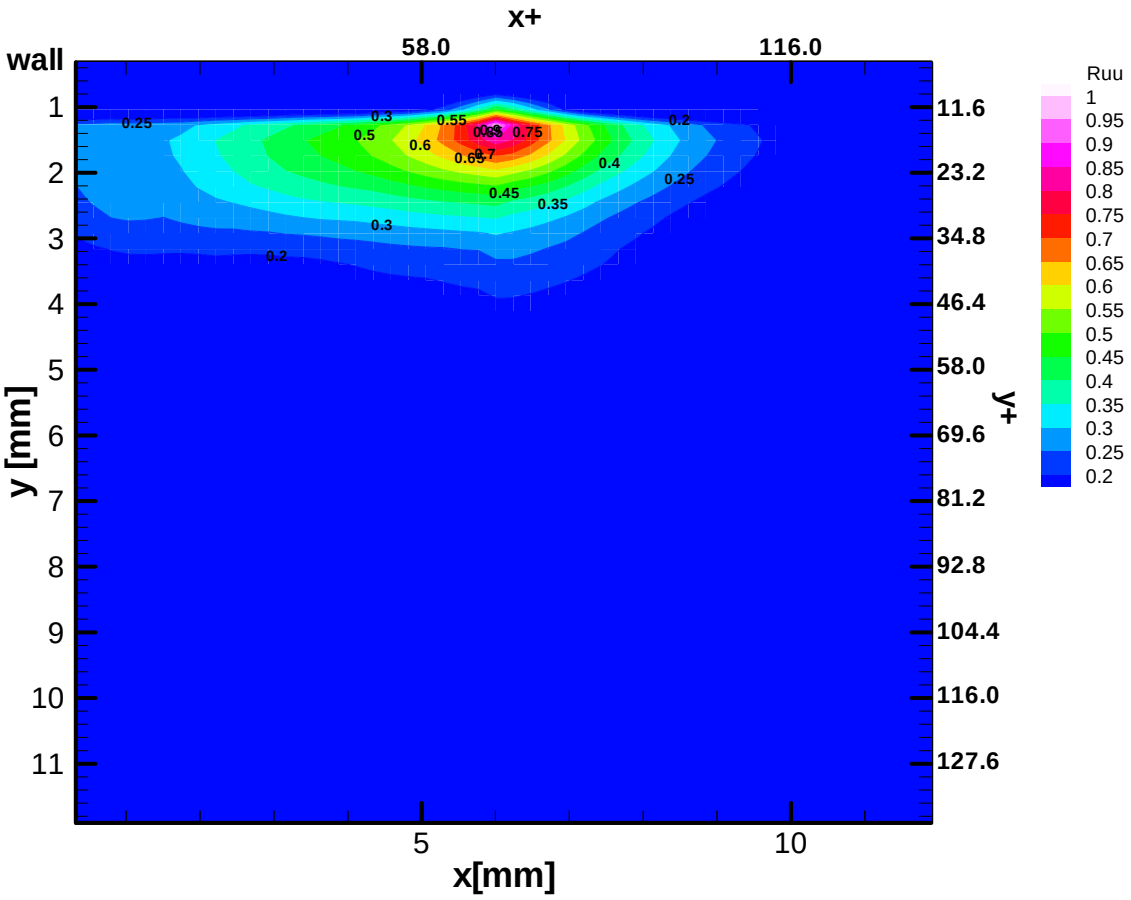

FIGURE 47. Two-dimensional two-point correlation coefficient at $x^+ = 69.7$, $y^+ = 14.7$ for streamwise fluctuating velocity for single phase.

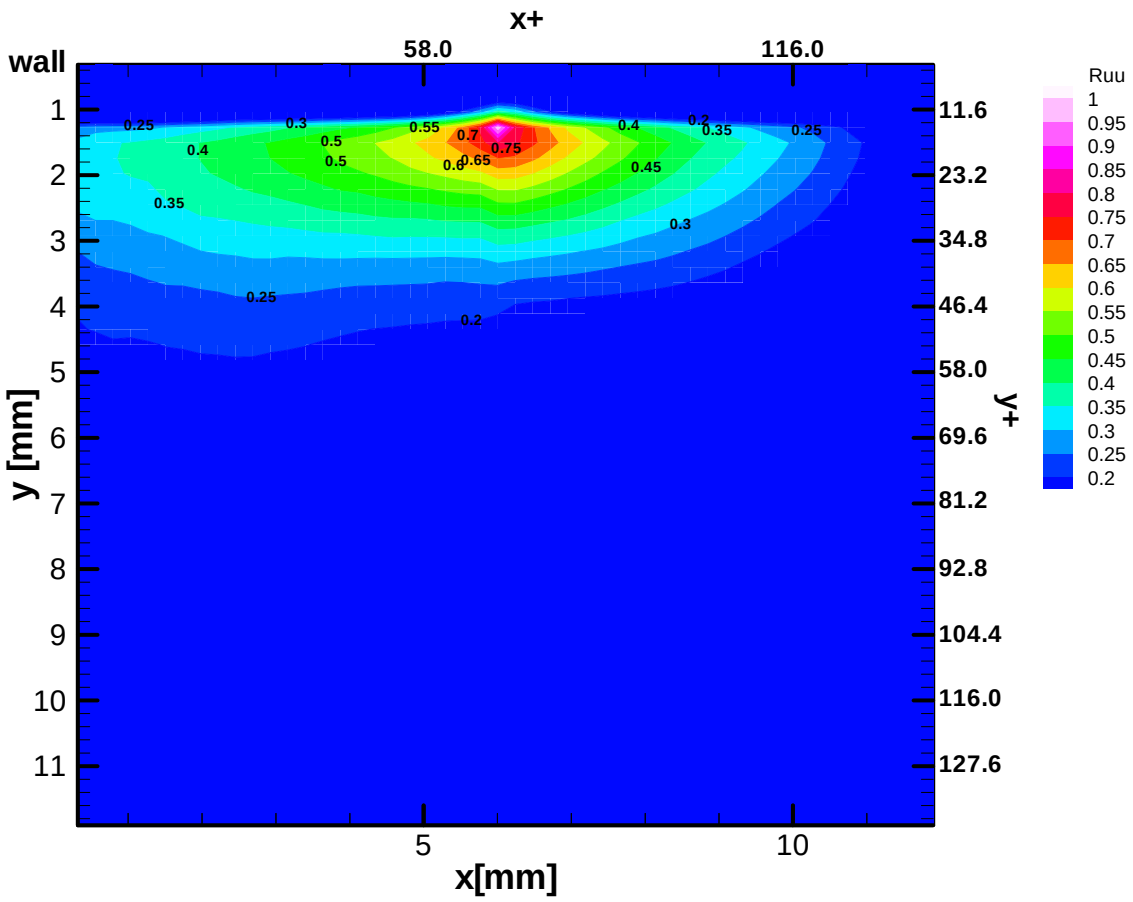

FIGURE 48. Two-dimensional two-point correlation coefficient at $x^+ = 69.7$, $y^+ = 14.7$ for streamwise fluctuating velocity for $\alpha = 2.4\%$, DR= 12.06%.

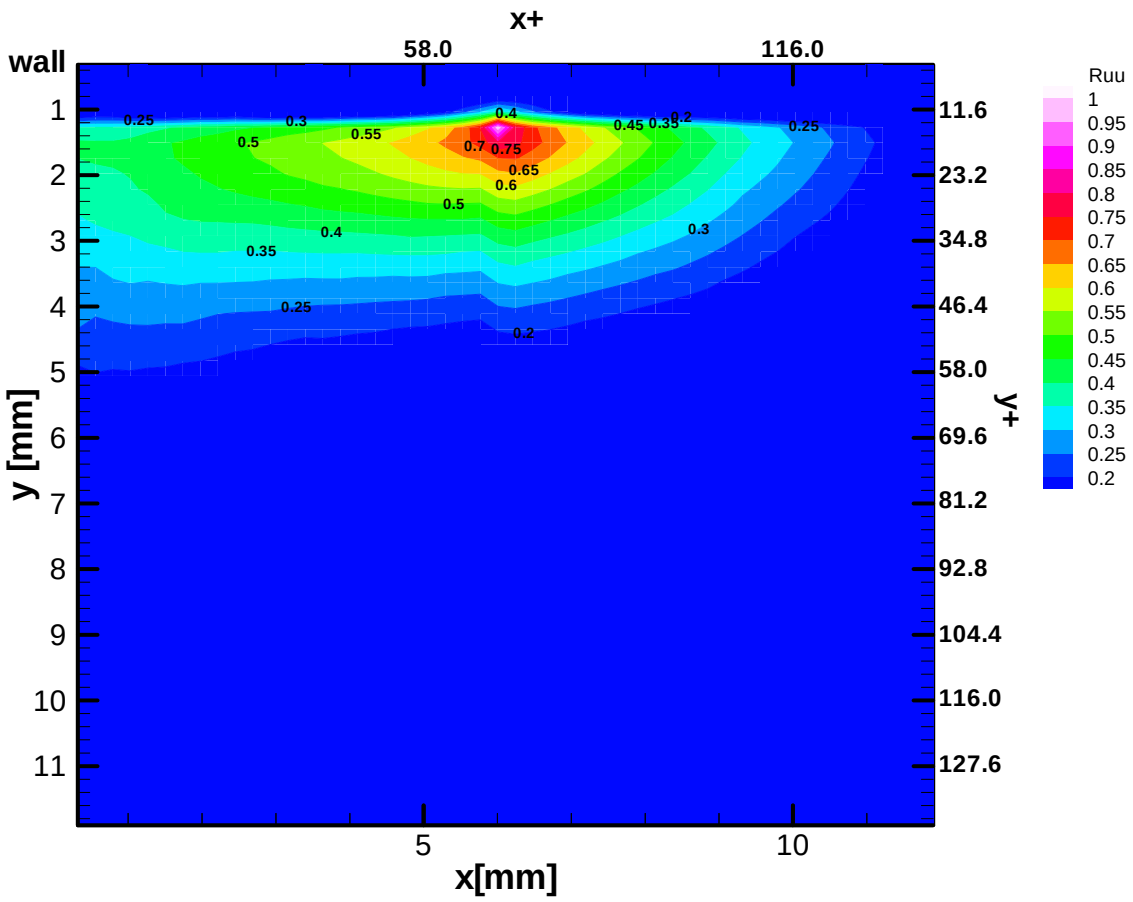

FIGURE 49. Two-dimensional two-point correlation coefficient at $x^+ = 69.7$, $y^+ = 14.7$ for streamwise fluctuating velocity for $\alpha = 3.4\%$, DR= 16.6%.

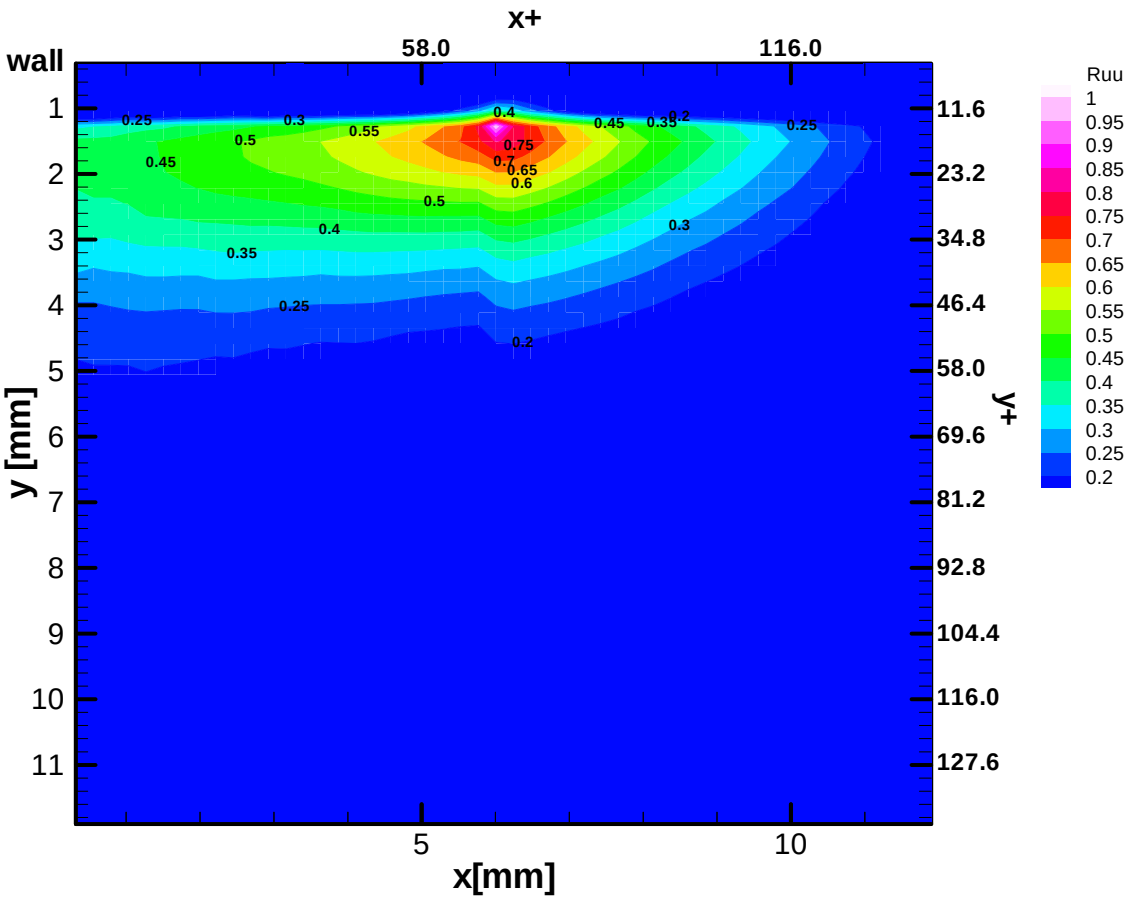

FIGURE 50. Two-dimensional two-point correlation coefficient at $x^+ = 69.7$, $y^+ = 14.7$ for streamwise fluctuating velocity for $\alpha = 4.4\%$, DR= 29.8%.

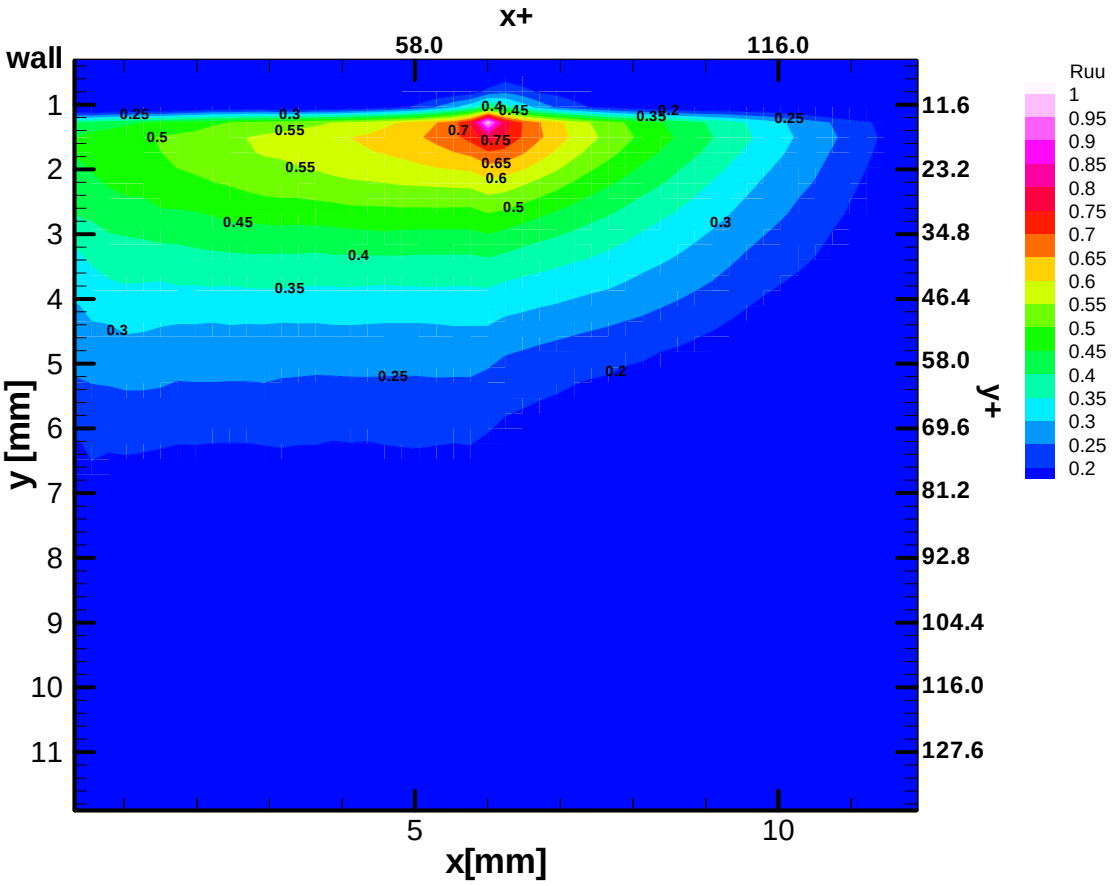

FIGURE 51. Two-dimensional two-point correlation coefficient at $x^+ = 69.7$, $y^+ = 14.7$ for streamwise fluctuating velocity for $\alpha = 4.9\%$, DR= 38.4%.

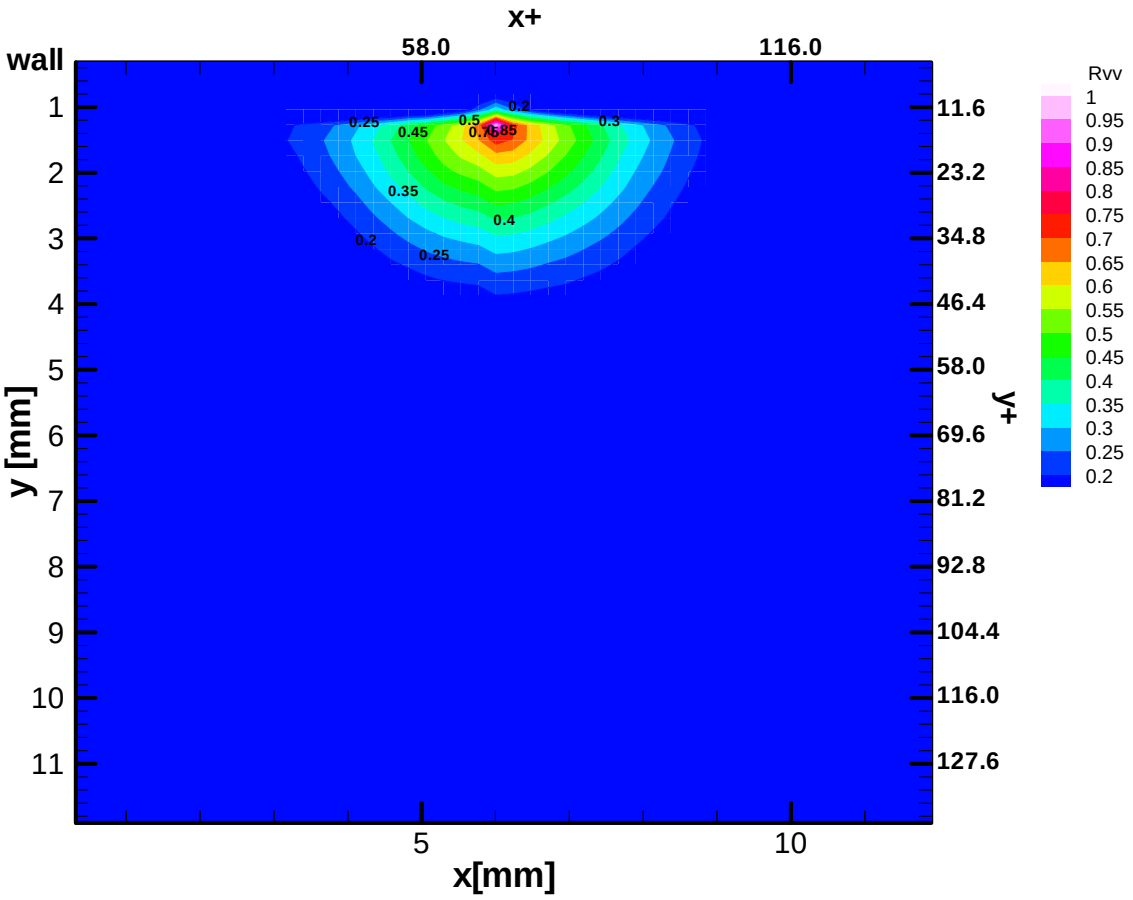

FIGURE 52. Two-dimensional two-point correlation coefficient at $x^+ = 69.7$, $y^+ = 14.7$ for normal fluctuating velocity for single phase.

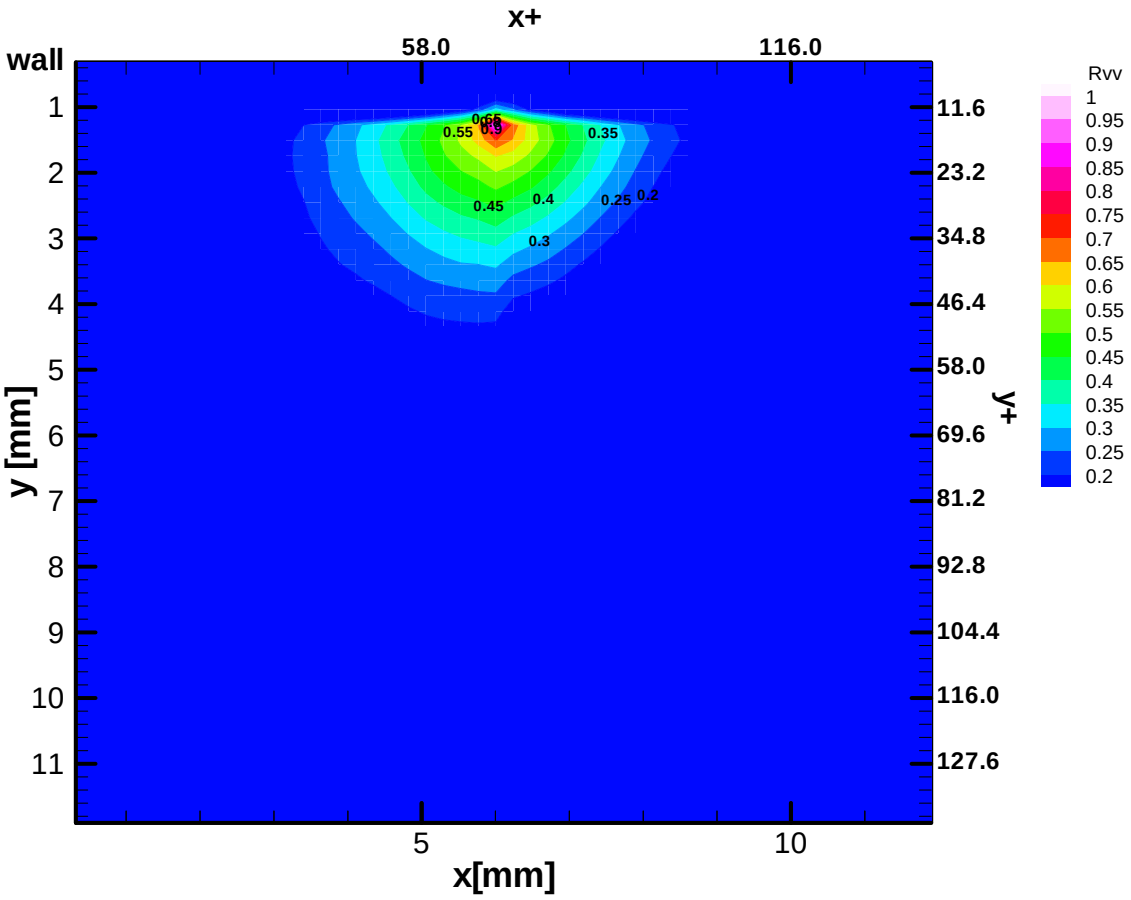

FIGURE 53. Two-dimensional two-point correlation coefficient at $x^+ = 69.7$, $y^+ = 14.7$ for normal fluctuating velocity for $\alpha = 2.4\%$, DR= 12.06%.

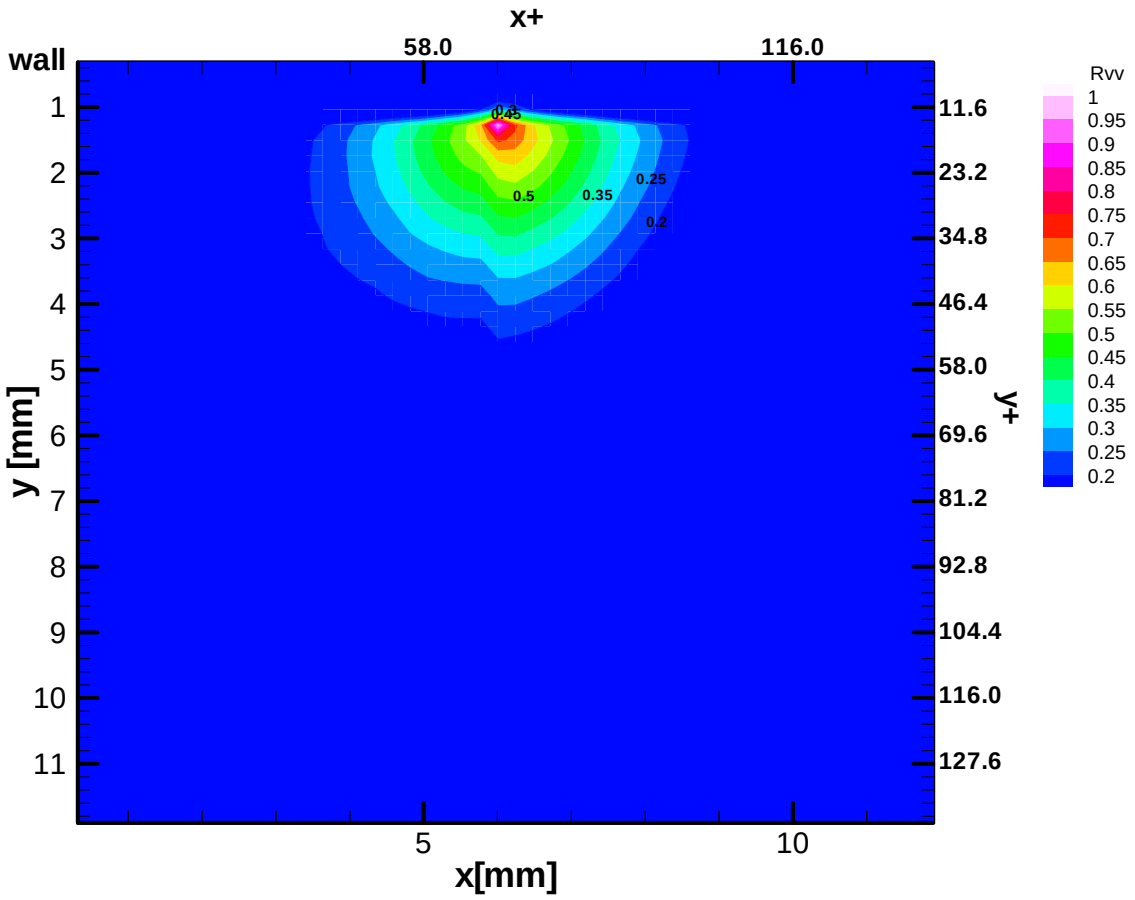

FIGURE 54. Two-dimensional two-point correlation coefficient at $x^+ = 69.7$, $y^+ = 14.7$ for normal fluctuating velocity for $\alpha = 3.4\%$, DR= 16.6%.

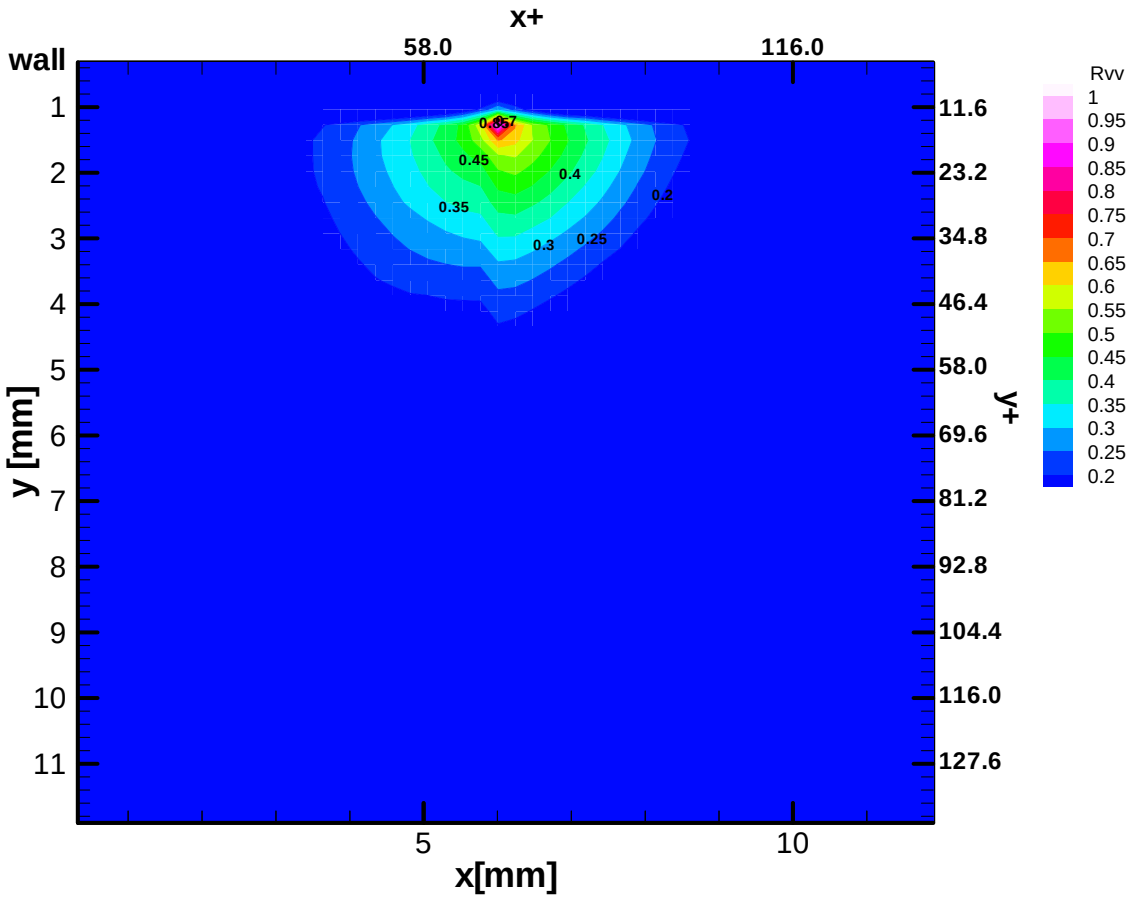

FIGURE 55. Two-dimensional two-point correlation coefficient at $x^+ = 69.7$, $y^+ = 14.7$ for normal fluctuating velocity for $\alpha = 4.4\%$, DR= 29.8%.

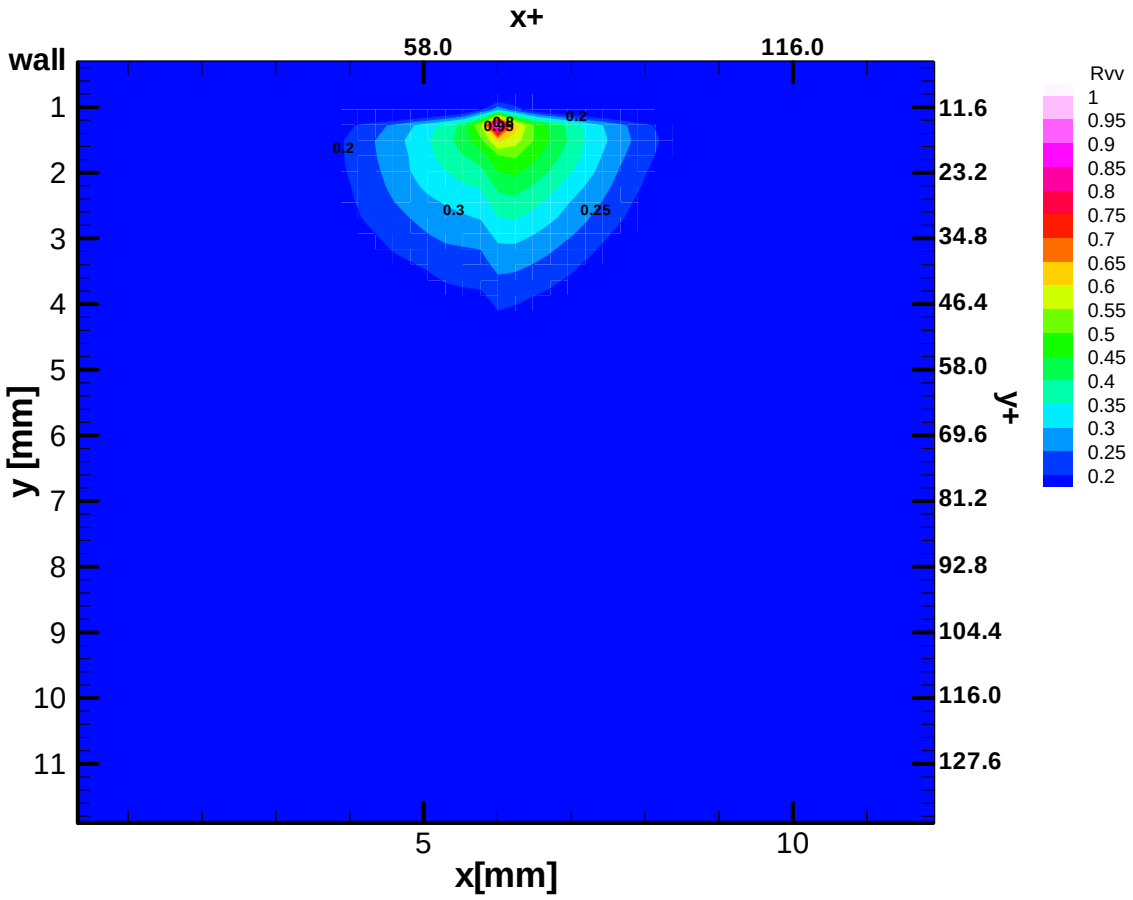

FIGURE 56. Two-dimensional two-point correlation coefficient at $x^+ = 69.7$, $y^+ = 14.7$ for normal fluctuating velocity for $\alpha = 4.9\%$, DR= 38.4%.

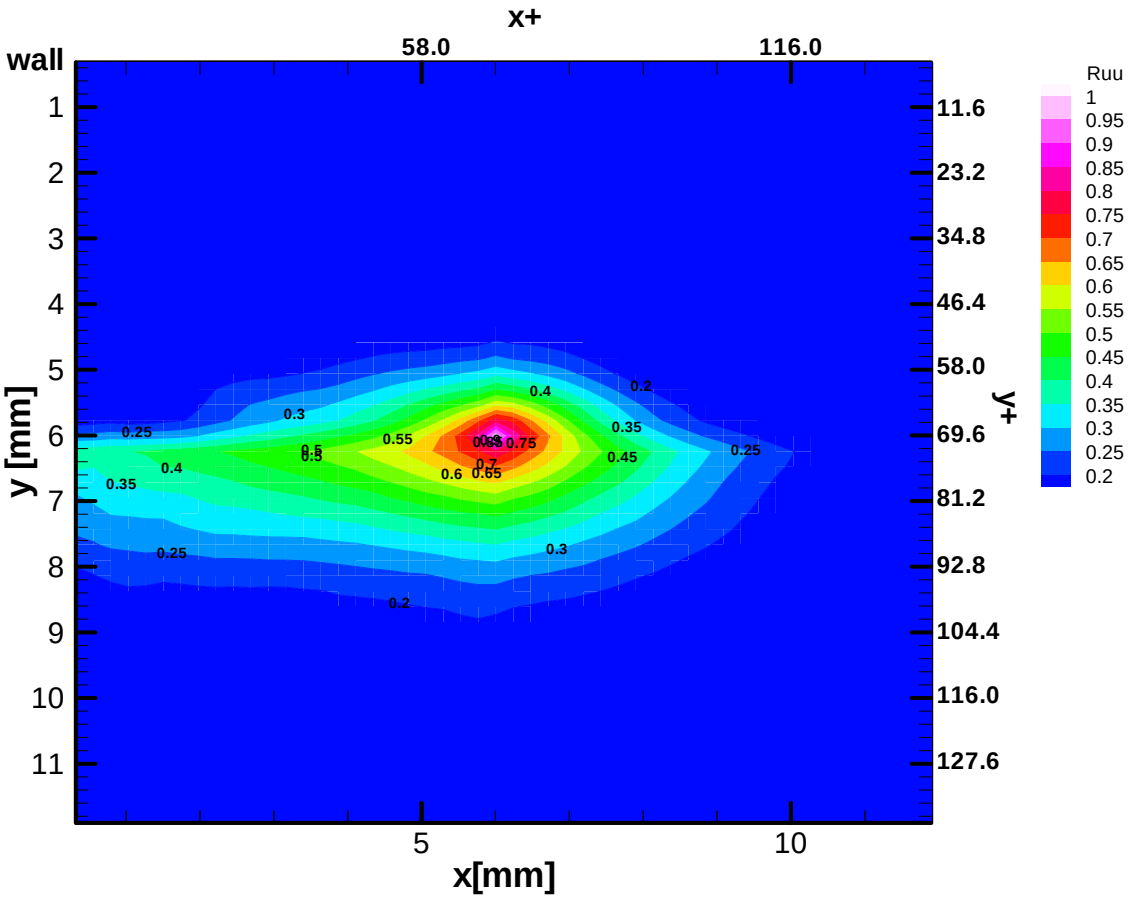

FIGURE 57. Two-dimensional two-point correlation coefficient at $x^+ = 69.7$, $y^+ = 69.7$ for streamwise fluctuating velocity for single phase.

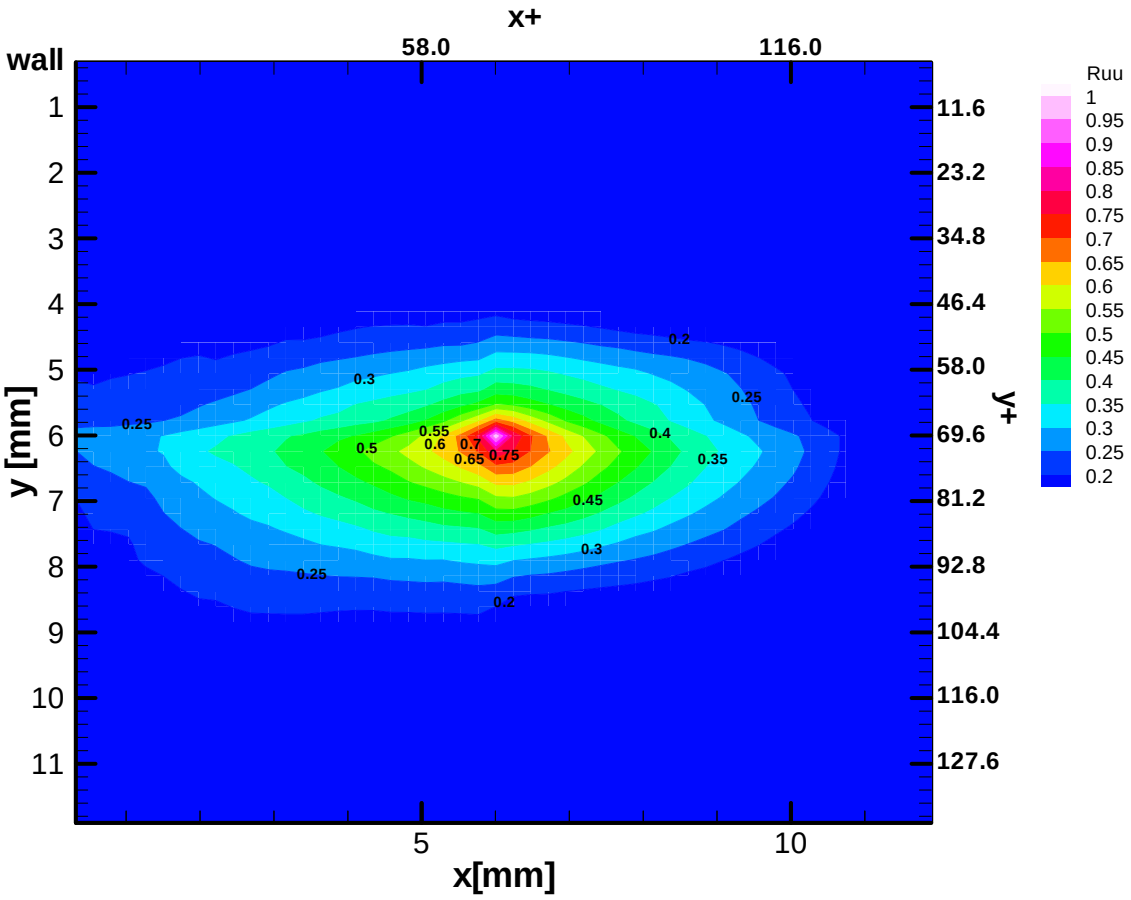

FIGURE 58. Two-dimensional two-point correlation coefficient at $x^+ = 69.7$, $y^+ = 69.7$ for streamwise fluctuating velocity for $\alpha = 2.4\%$, DR= 12.06%.

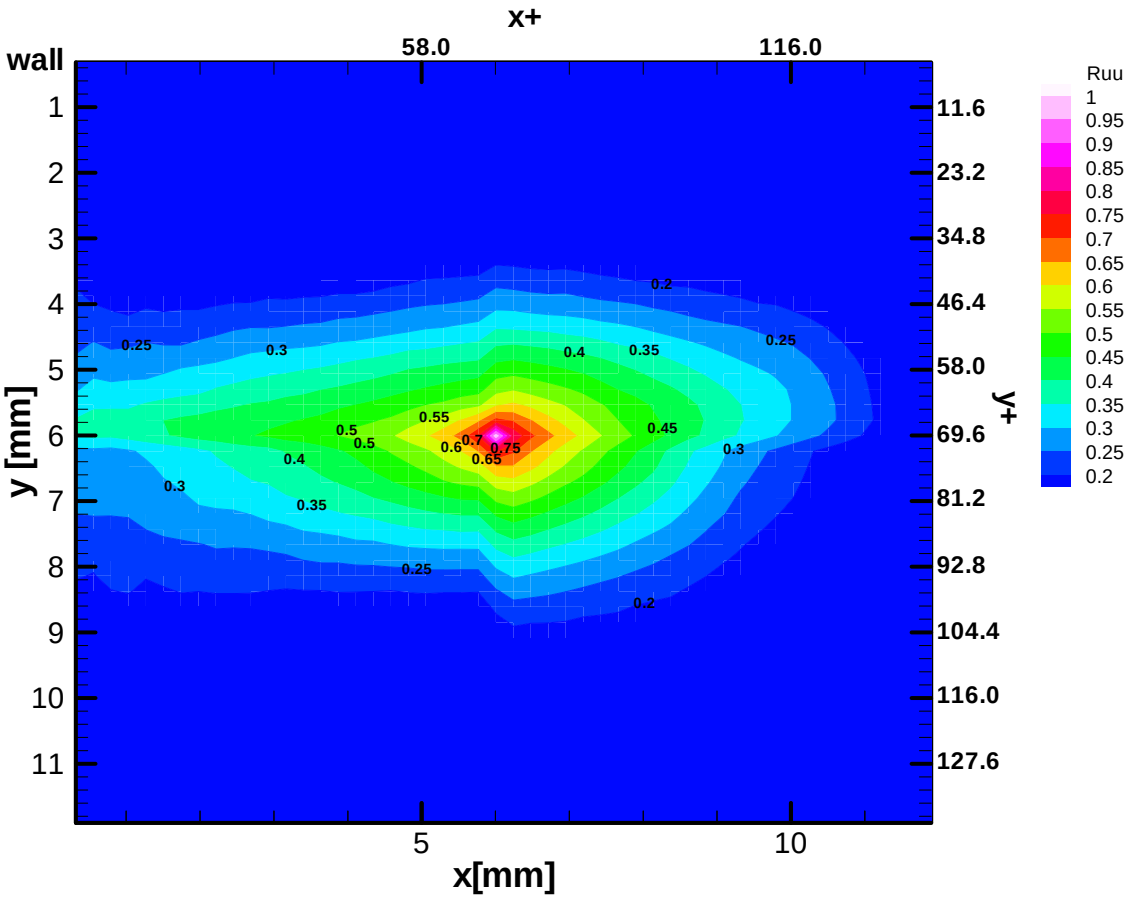

FIGURE 59. Two-dimensional two-point correlation coefficient at $x^+ = 69.7$, $y^+ = 69.7$ for streamwise fluctuating velocity for $\alpha = 3.4\%$, DR= 16.6%.

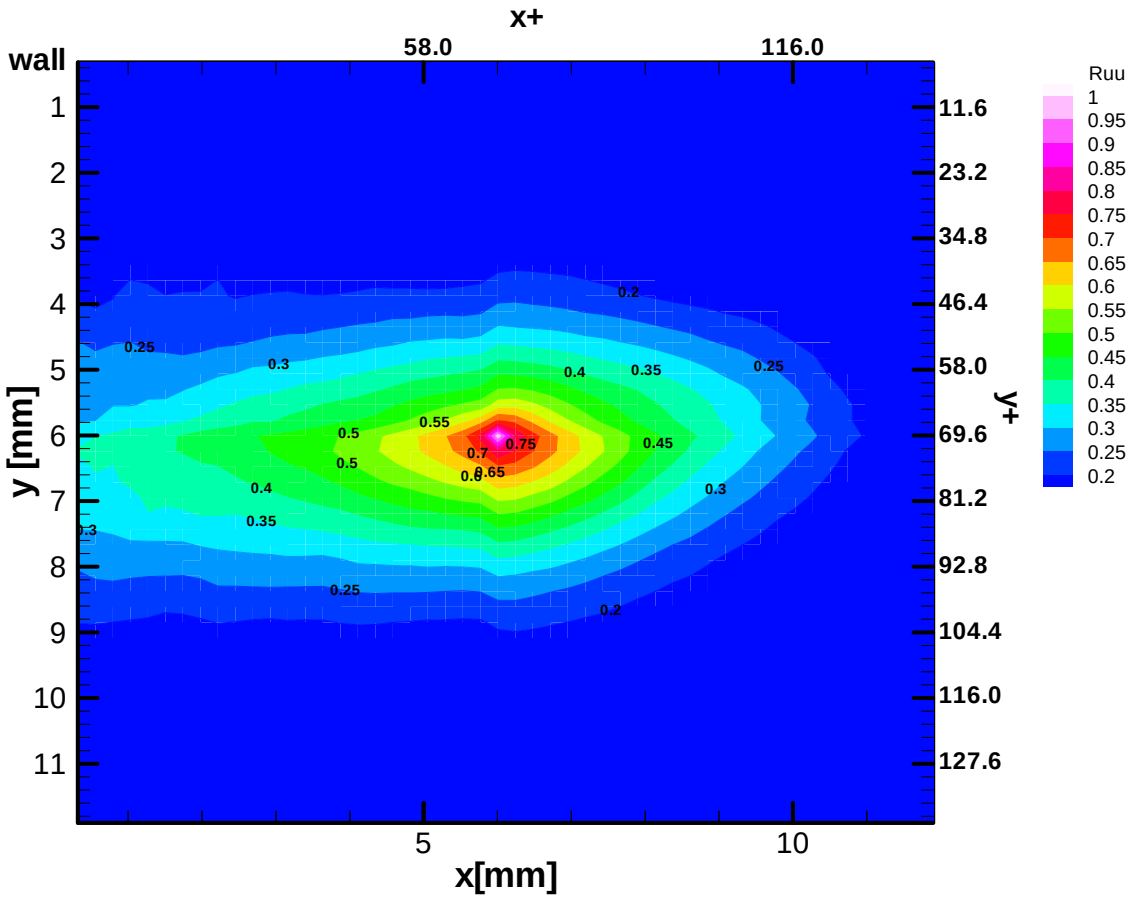

FIGURE 60. Two-dimensional two-point correlation coefficient at $x^+ = 69.7$, $y^+ = 69.7$ for streamwise fluctuating velocity for $\alpha = 4.4\%$, DR = 29.8%.

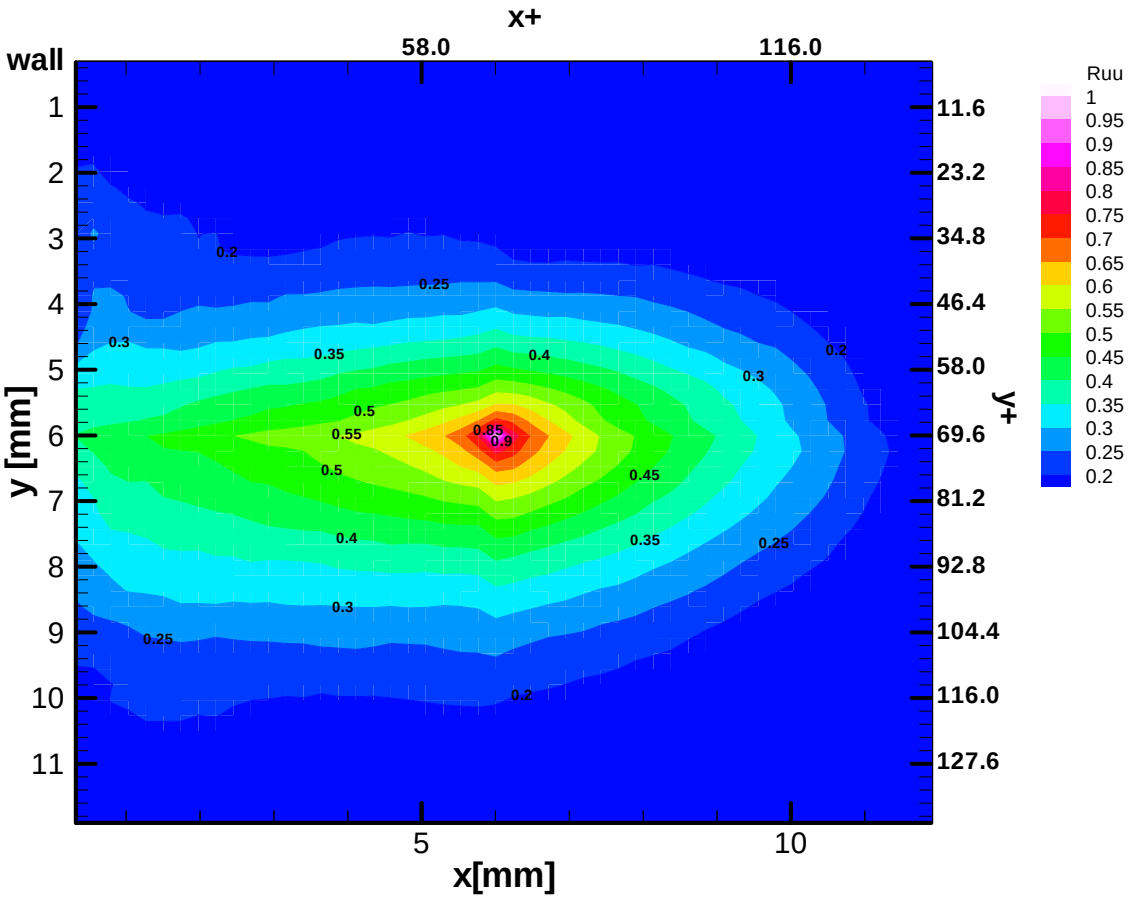

FIGURE 61. Two-dimensional two-point correlation coefficient at $x^+ = 69.7$, $y^+ = 69.7$ for streamwise fluctuating velocity for $\alpha = 4.9\%$, DR = 38.4%.

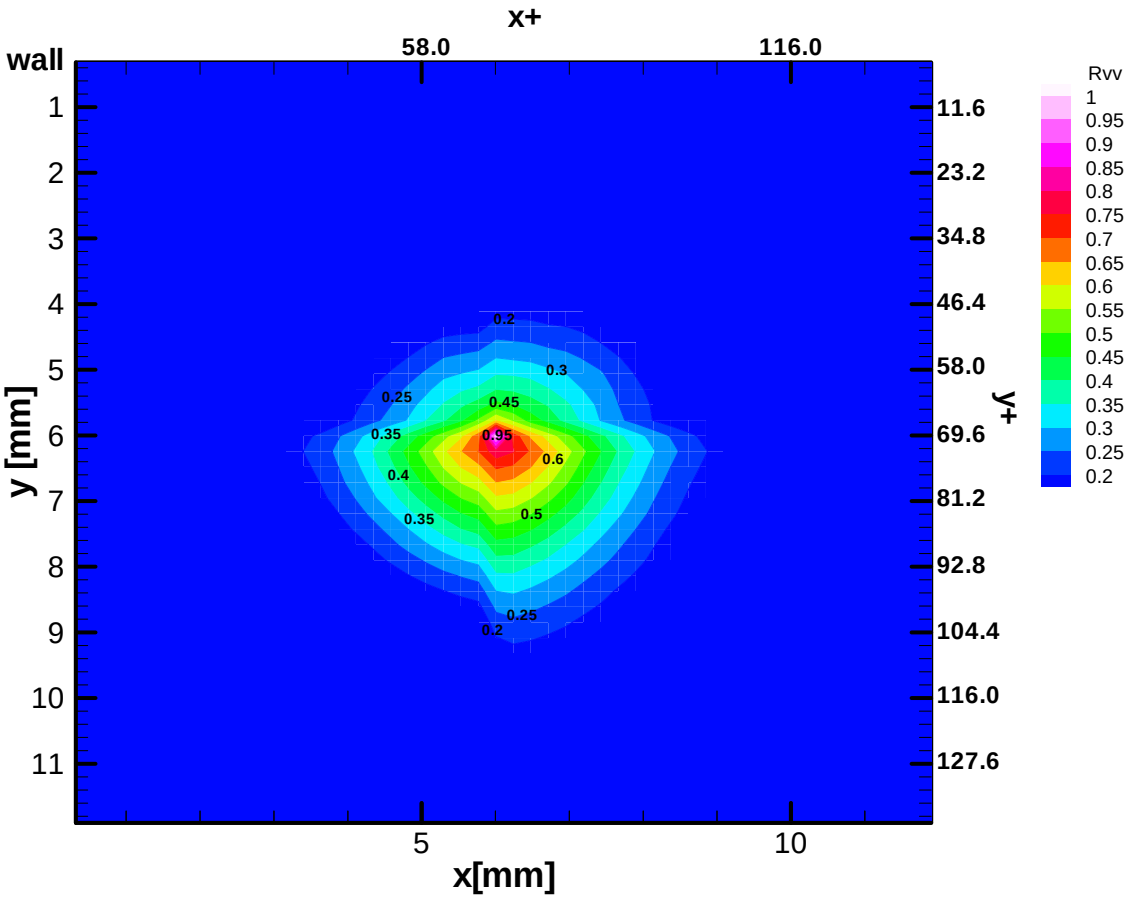

FIGURE 62. Two-dimensional two-point correlation coefficient at $x^+ = 69.7$, $y^+ = 69.7$ for normal fluctuating velocity for single phase.

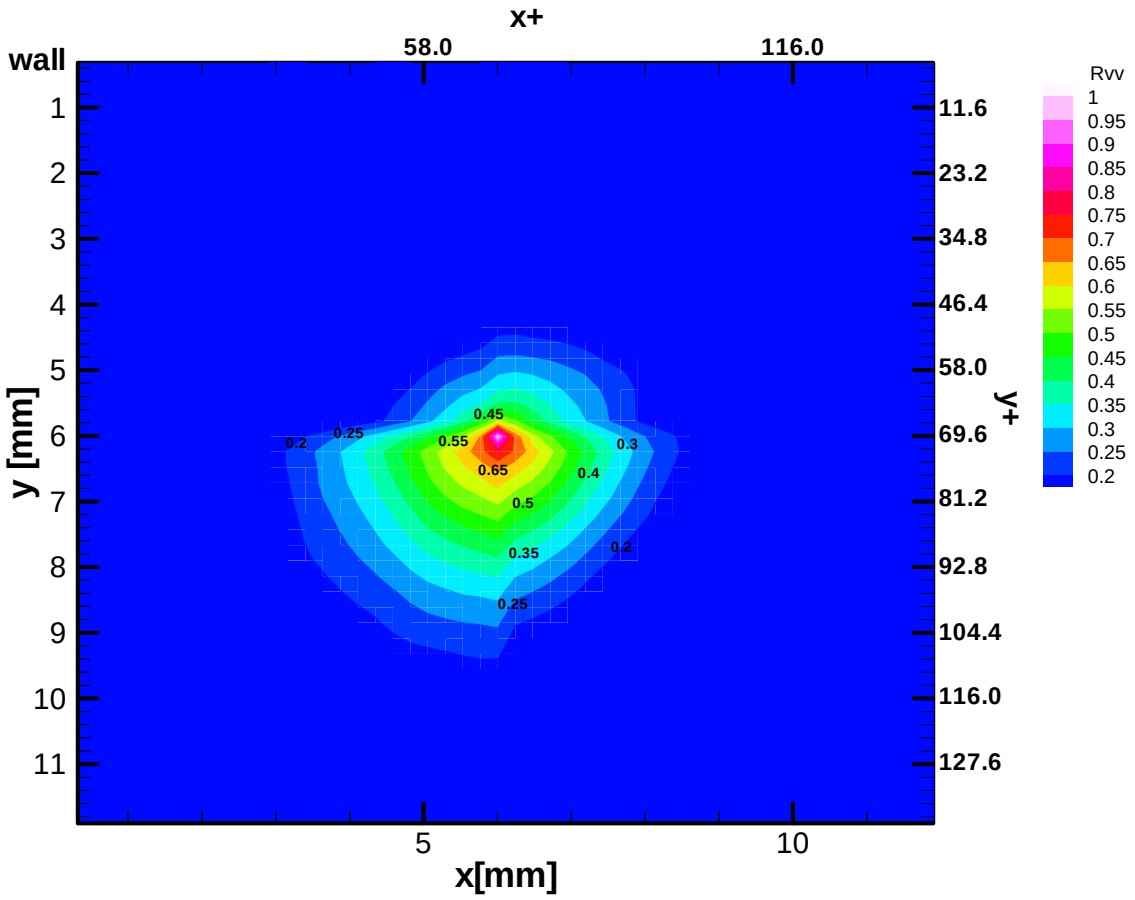

FIGURE 63. Two-dimensional two-point correlation coefficient at $x^+ = 69.7$, $y^+ = 69.7$ for normal fluctuating velocity for $\alpha = 2.4\%$, DR = 12.06%.

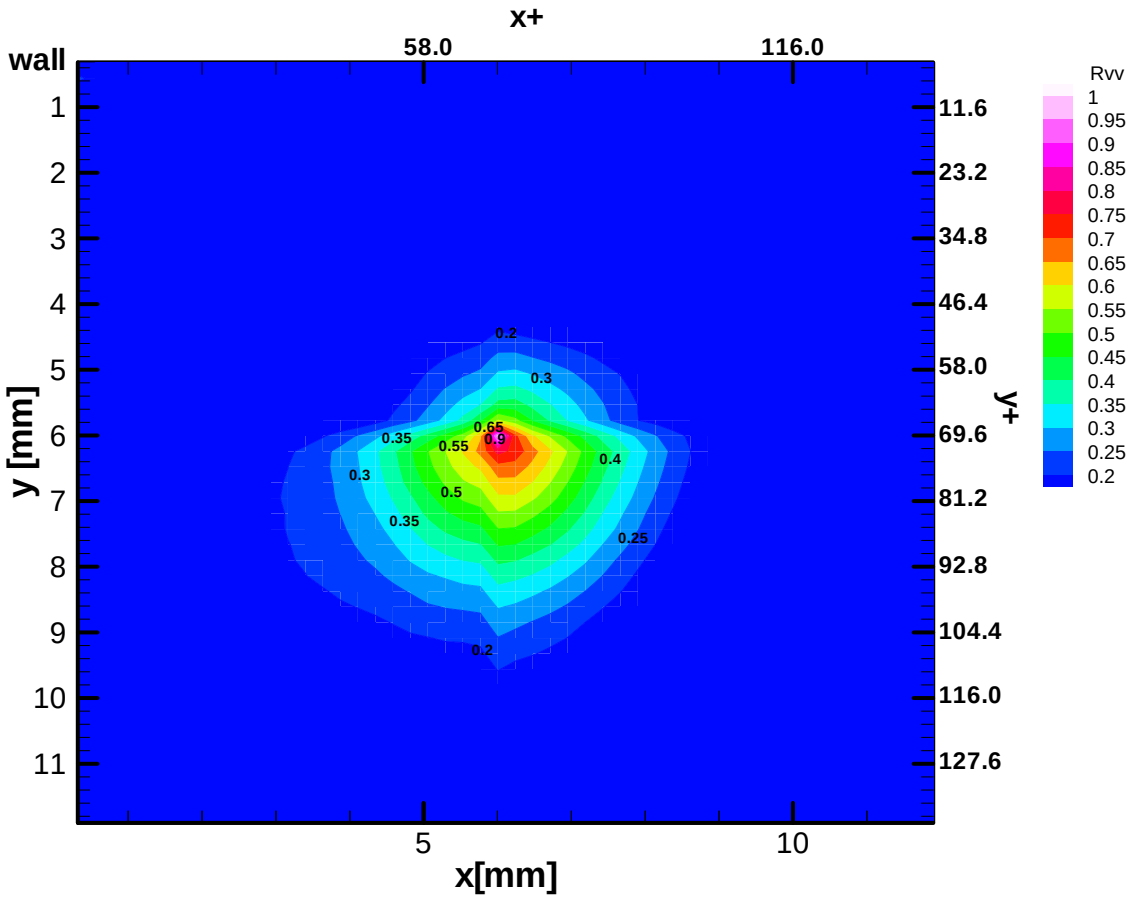

FIGURE 64. Two-dimensional two-point correlation coefficient at $x^+ = 69.7$, $y^+ = 69.7$ for normal fluctuating velocity for $\alpha = 3.4\%$, DR = 16.6%.

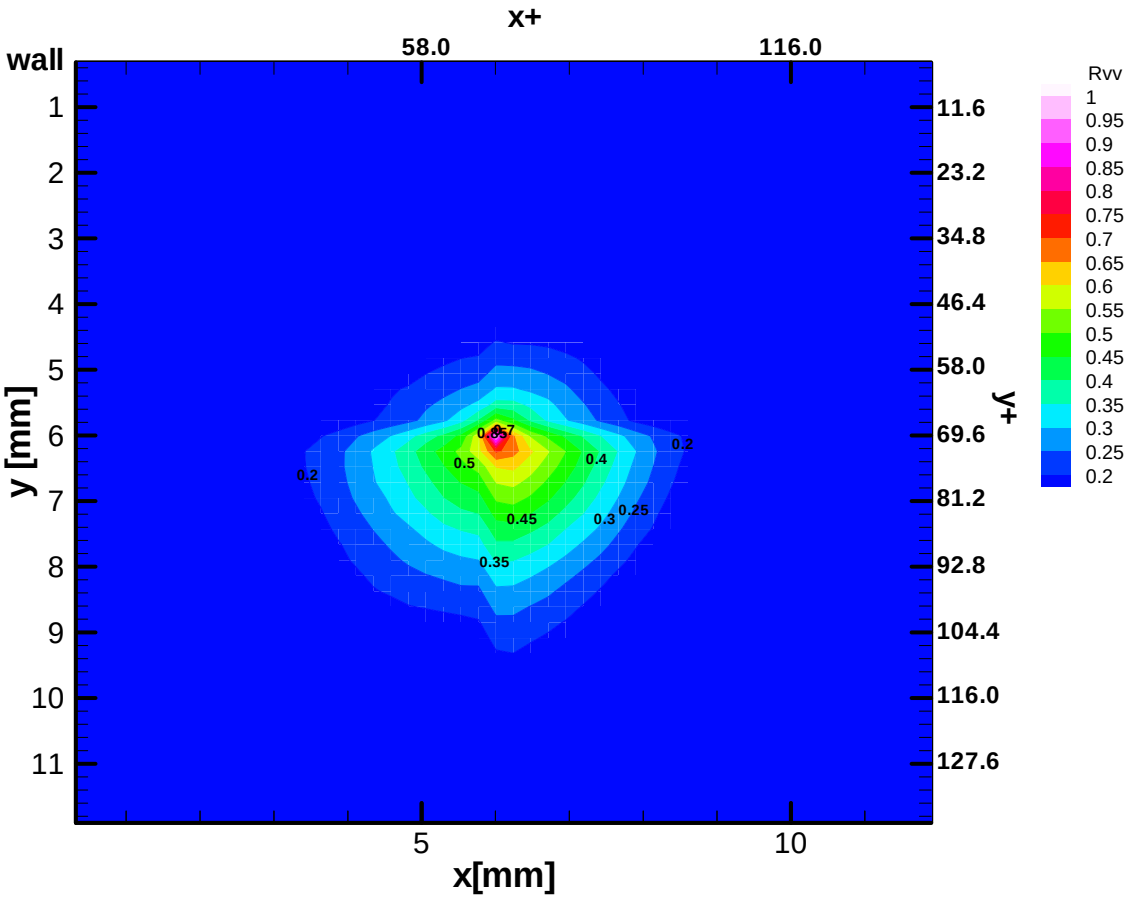

FIGURE 65. Two-dimensional two-point correlation coefficient at $x^+ = 69.7$, $y^+ = 69.7$ for normal fluctuating velocity for $\alpha = 4.4\%$, DR = 29.8%.

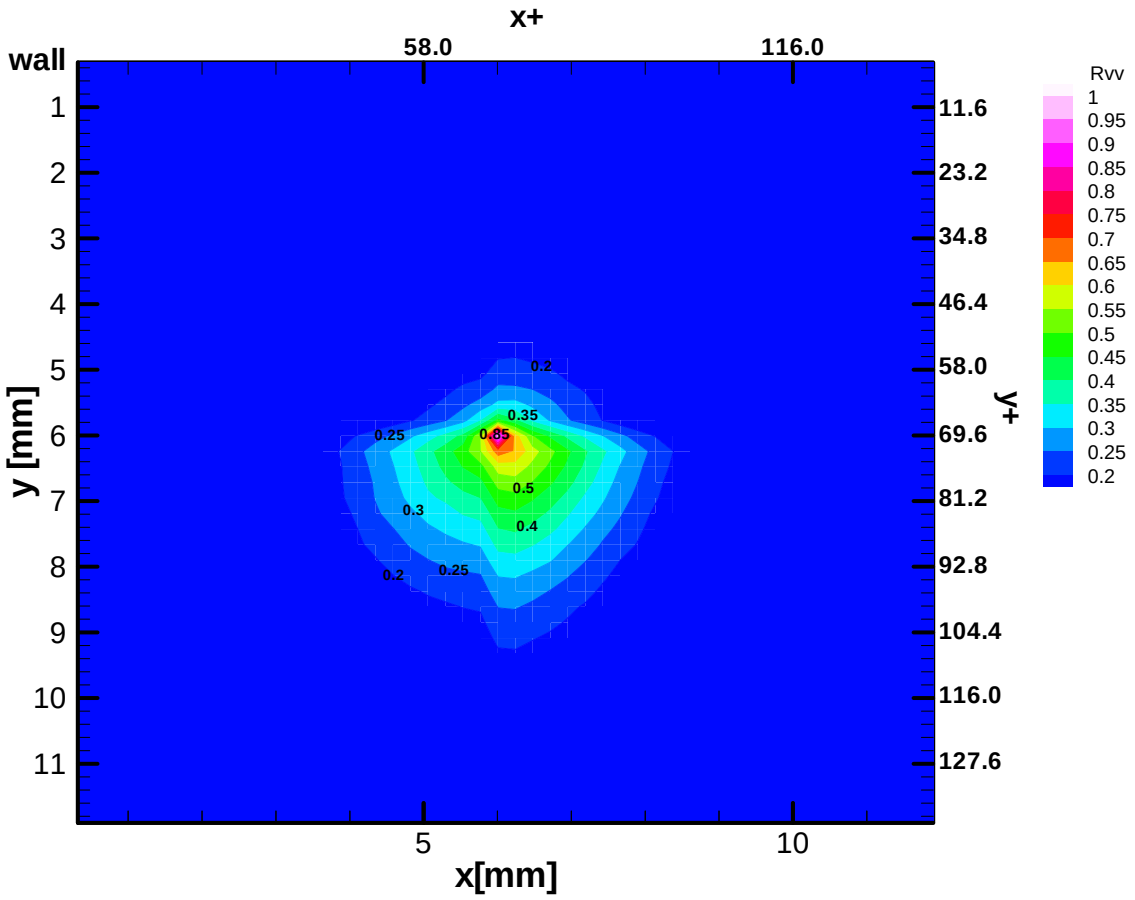

FIGURE 66. Two-dimensional two-point correlation coefficient at $x^+ = 69.7$, $y^+ = 69.7$ for normal fluctuating velocity for $\alpha = 4.9\%$, DR = 38.4%.

4.7 Vorticity and Rate of Strain

In turbulent flows, the existence of a high average vorticity is well known. This high level of vorticity is cause by the extension or "stretching" of vortex filaments (Taylor 1938; Lesiur 1990, Tennekes and Lumley 1972). Vortex stretching, which is mathematically expressed as $\omega_j s_{ij}$, has been regarded as the cause of the high rate of dissipation associated with turbulent motions. The injection of microbubbles within the boundary layer seems to produce an attenuation of this phenomenon. Although vorticity is always present in the flow, there seems to be a counteracting phenomenon that suppresses the stretching in the flow. Figures 67 to 71 show the average vorticity fields obtained for single phase and two-phase flow at different void fraction values. It is observed that the close to the wall, there is a pronounced decrease in the vorticity as the void fraction increases. In figures 72 to 76, instantaneous fields of the z-component of the fluctuating vorticity are shown. In two-phase flow cases, the instantaneous location of the microbubbles is also shown (microbubbles are not in scale). It is observed that the microbubbles act as a physical barrier that surrounds zones with the same vorticity value. This might be the source of a decrease in the decrease, and possibly total suppression of the vortex stretching phenomenon.

Since the vortex stretching is essentially a process of interaction of vorticity and rate of strain (Tsinober 2001), maps with the average or the squared fluctuating rate of strain are presented in figures 77 to 81 for single and two-phase flows.

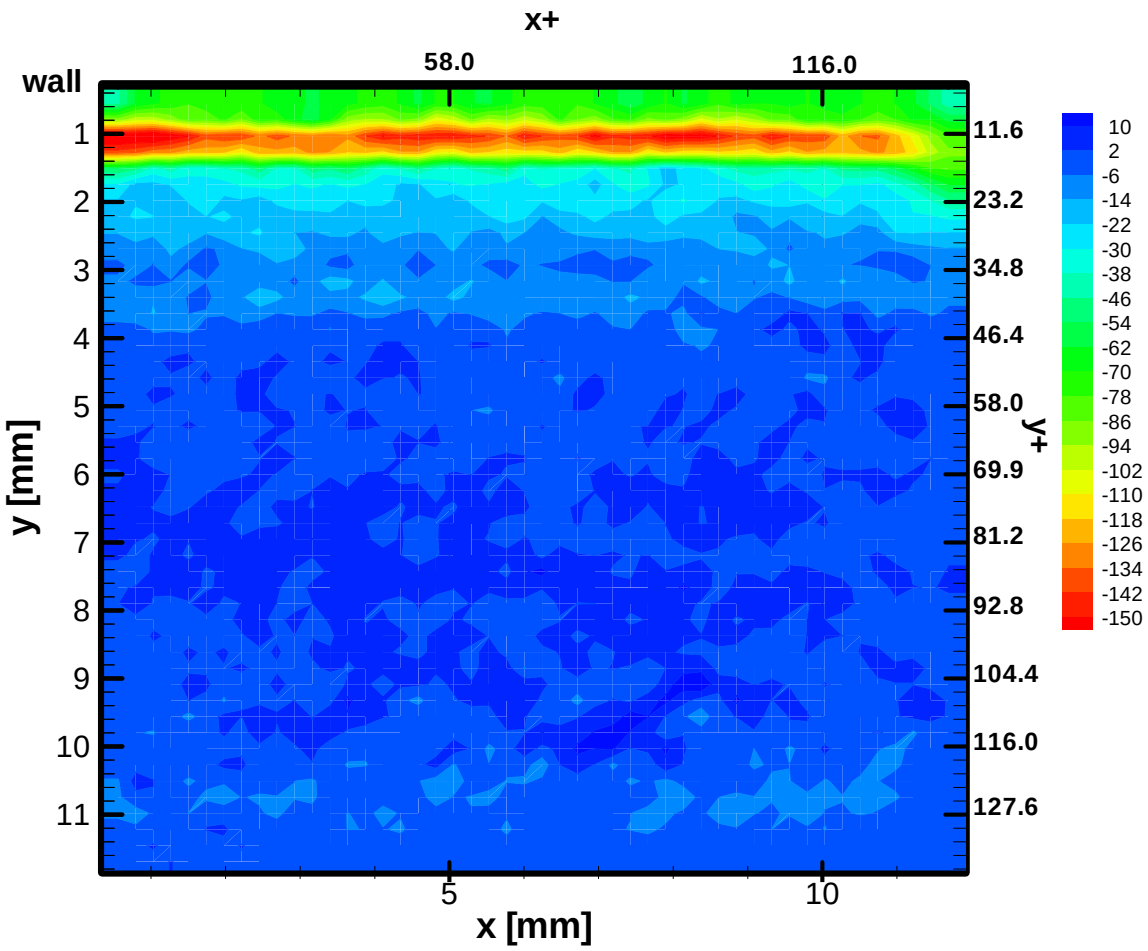

FIGURE 67. Average vorticity field for single phase flow.

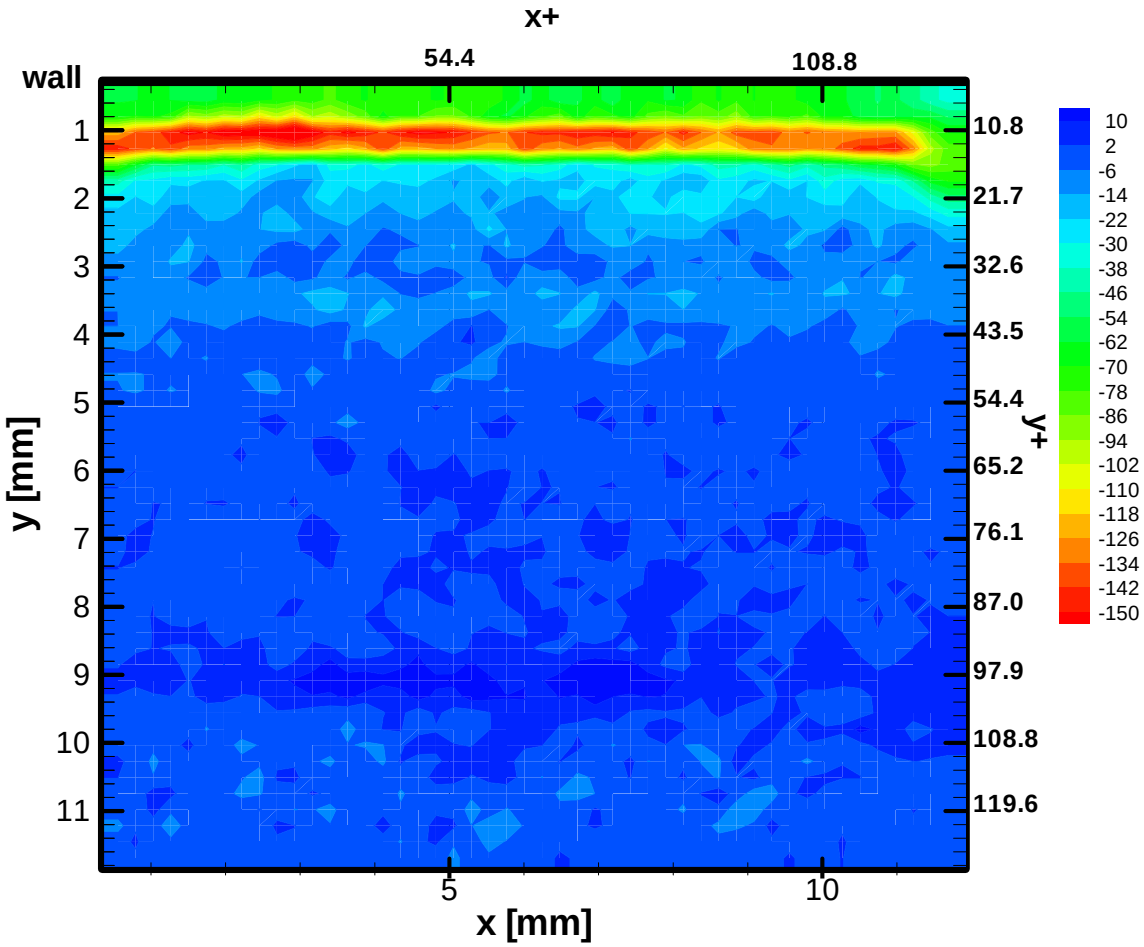

FIGURE 68. Average vorticity field for α = 2.4%, DR = 12.06%.

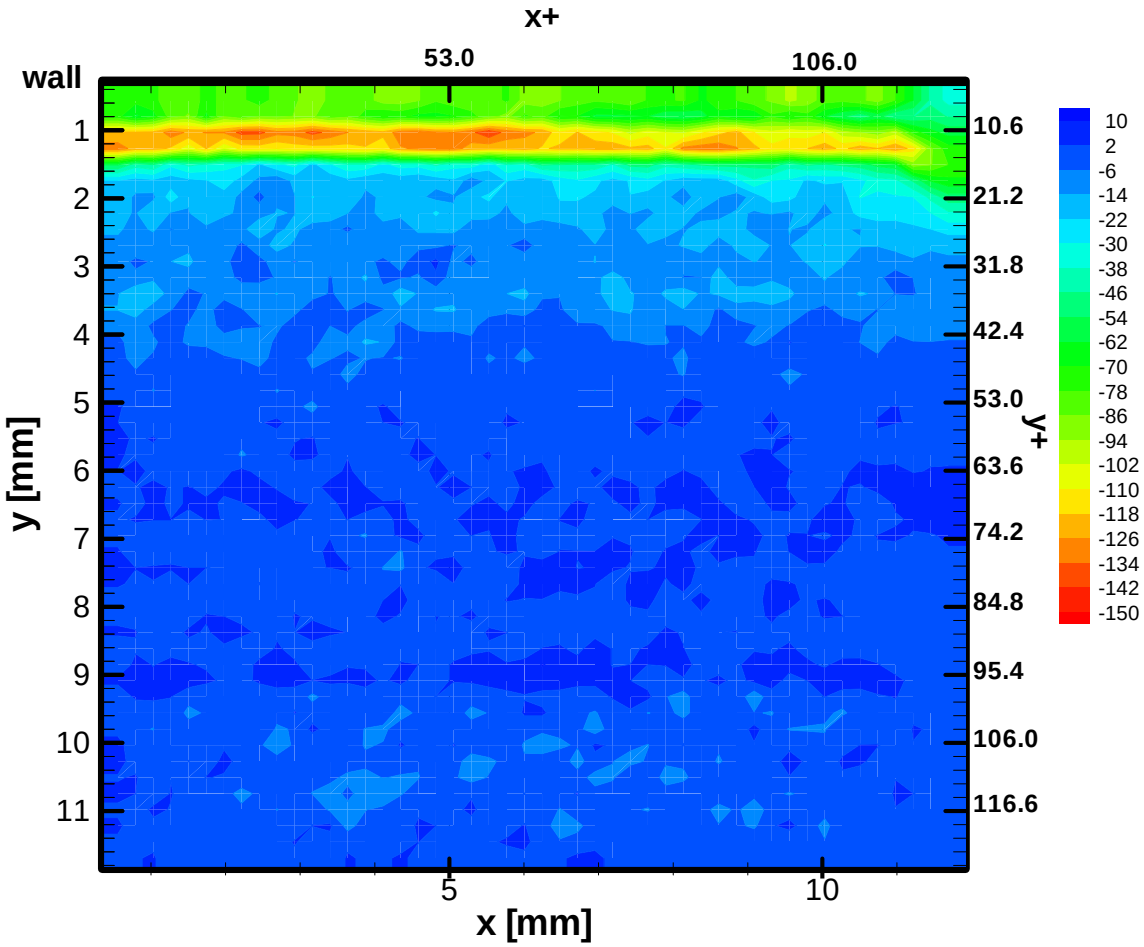

FIGURE 69. Average vorticity field for α = 3.4%, DR = 16.6%.

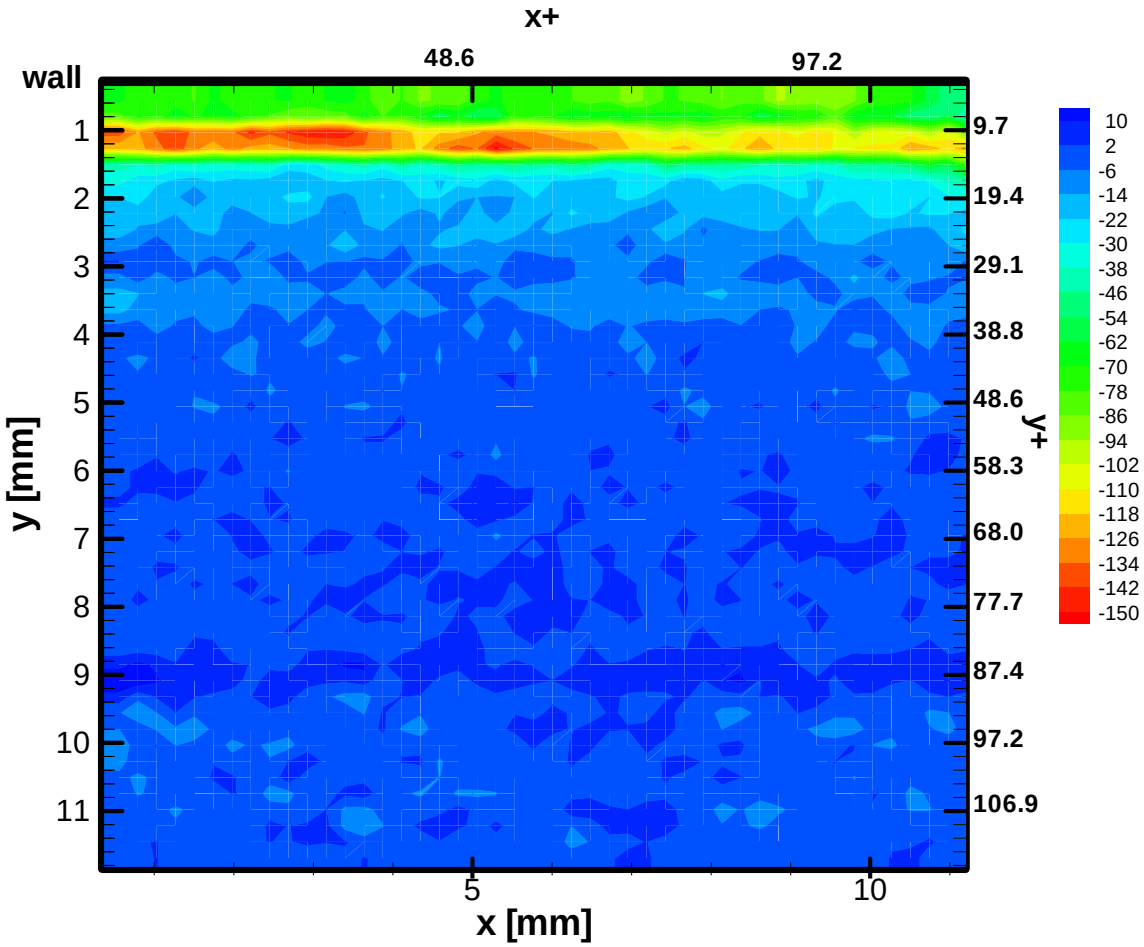

FIGURE 70. Average vorticity field for α = 4.4%, DR = 29.8%.

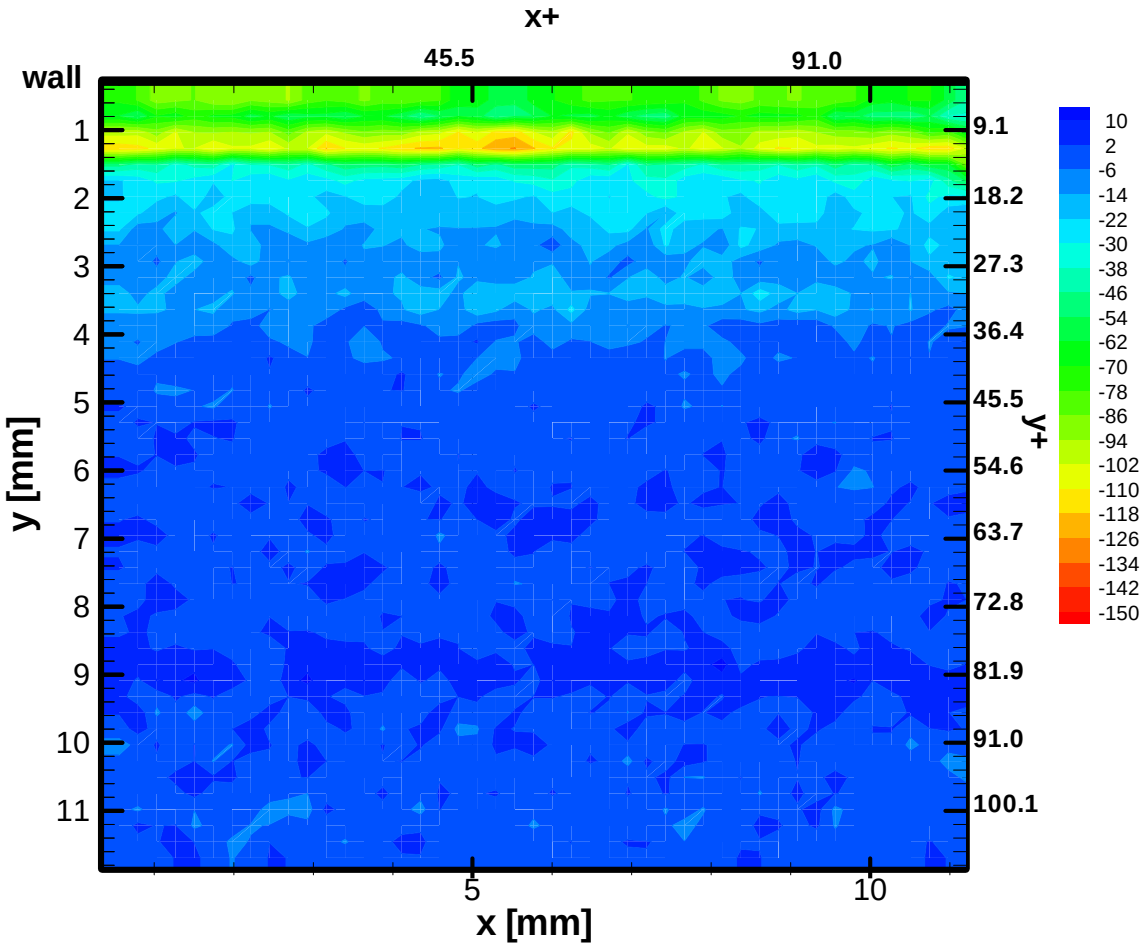

FIGURE 71. Average vorticity field for α = 4.9%, DR = 38.4%.

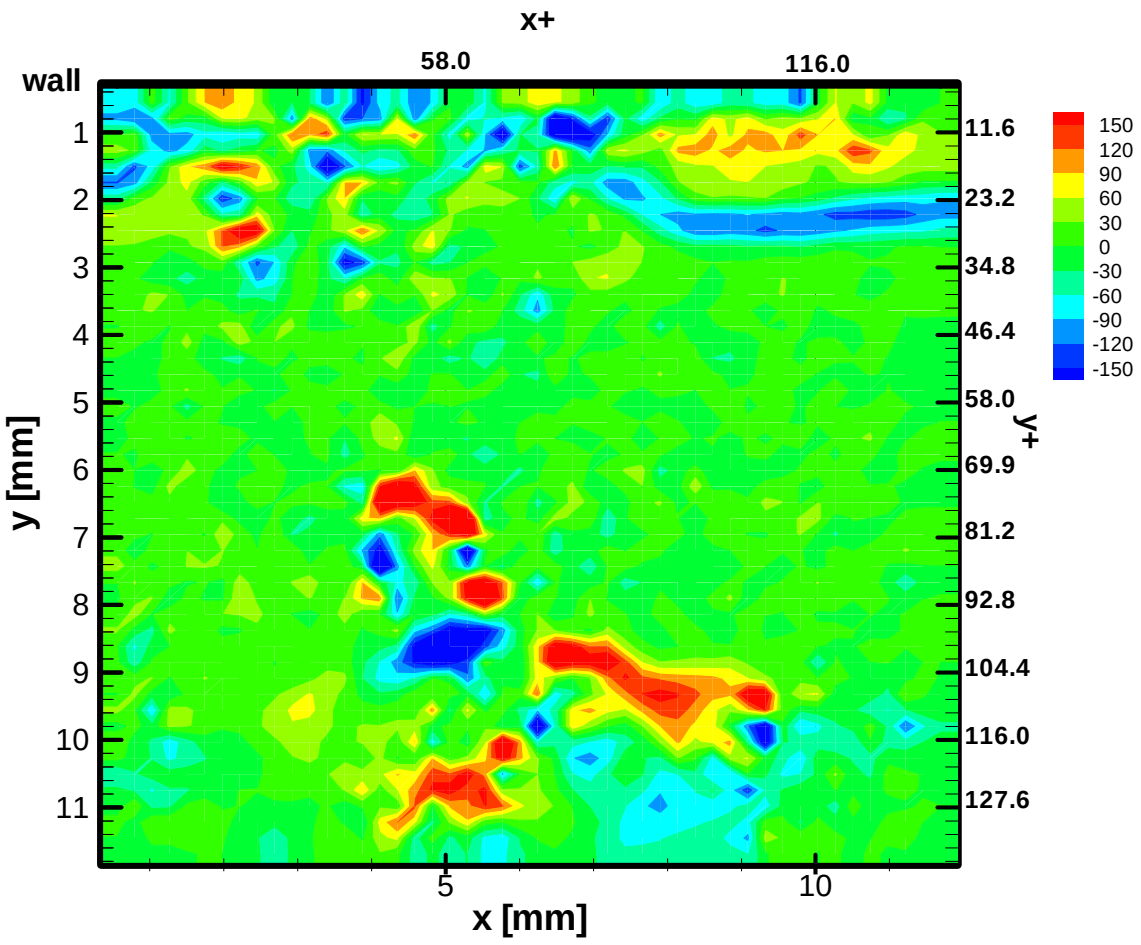

FIGURE 72. Instantaneous z-vorticity fluctuation field for single phase flow.

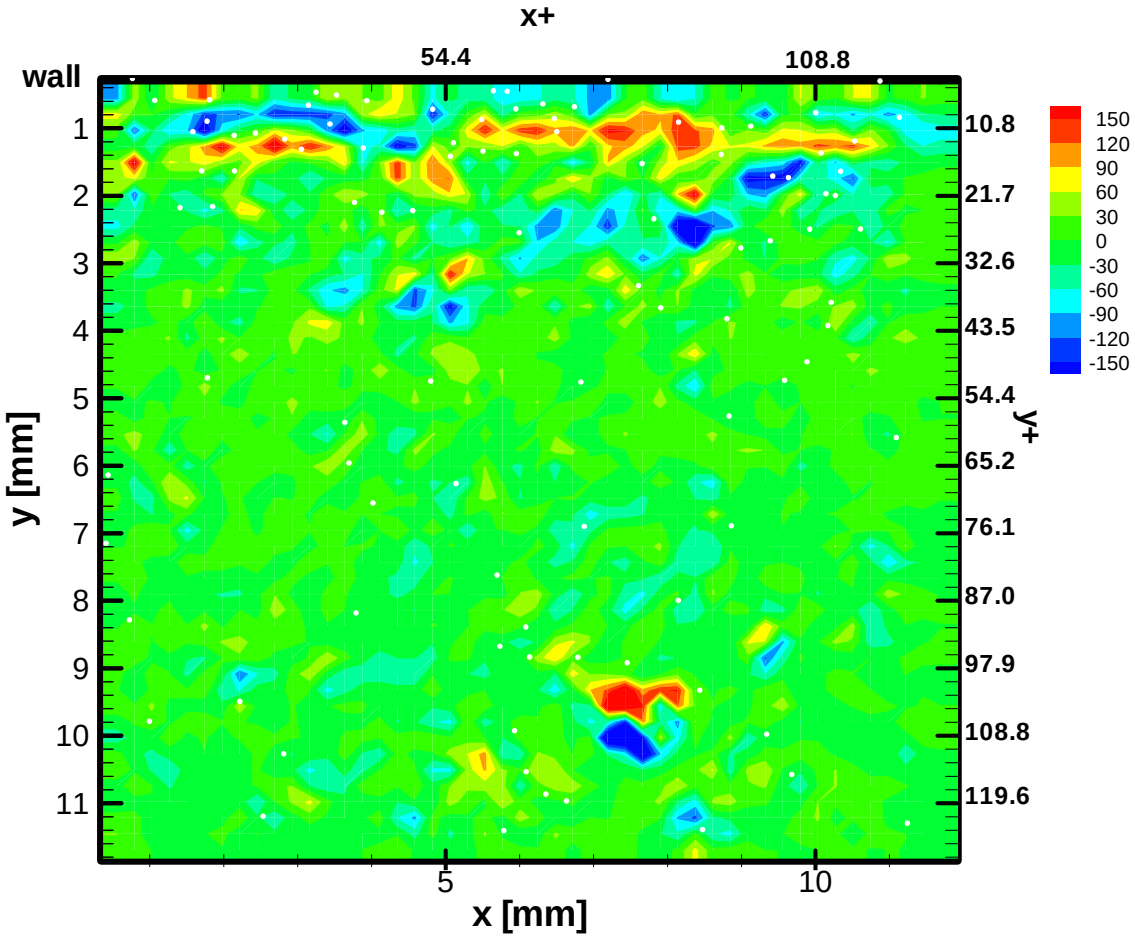

FIGURE 73. Instantaneous z-vorticity fluctuation field α = 2.4%, DR = 12.06%.

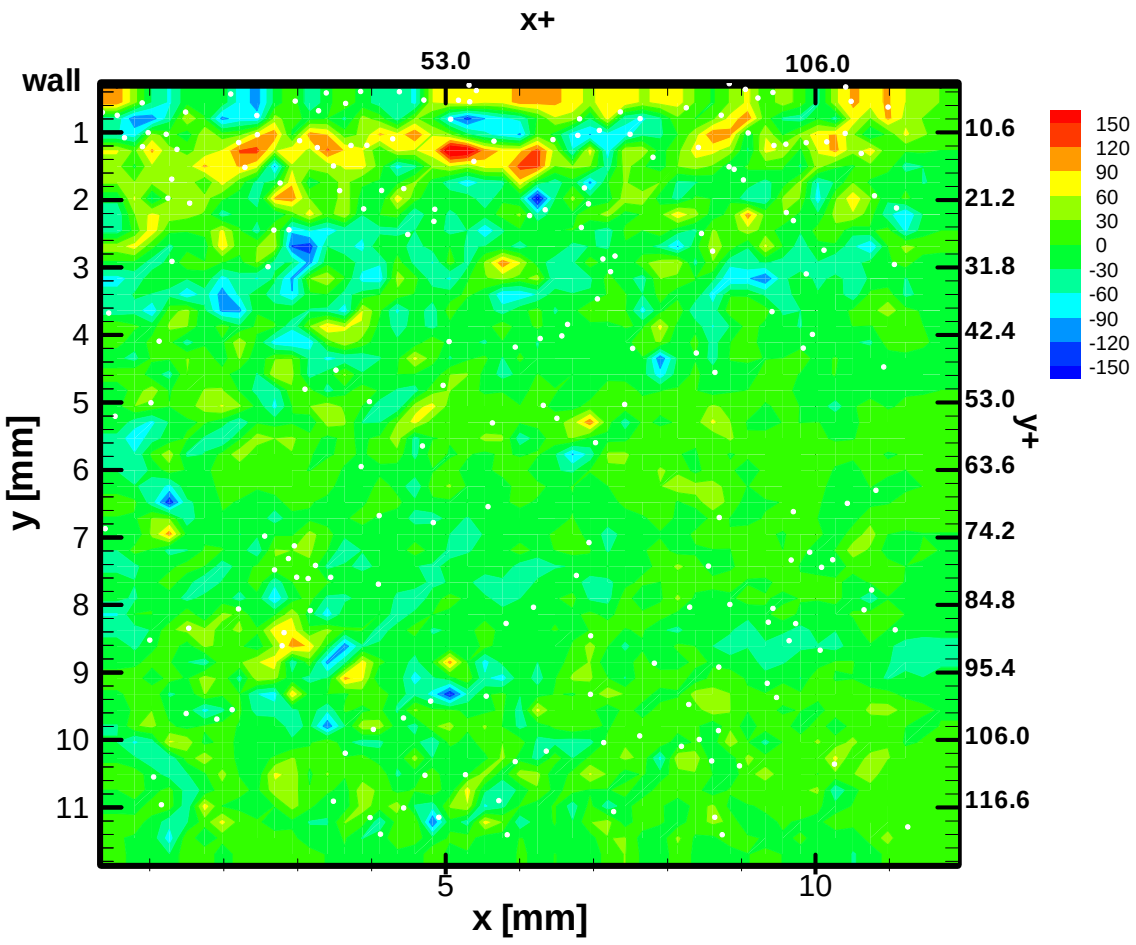

FIGURE 74. Instantaneous z-vorticity fluctuation field α = 3.4%, DR = 16.6%.

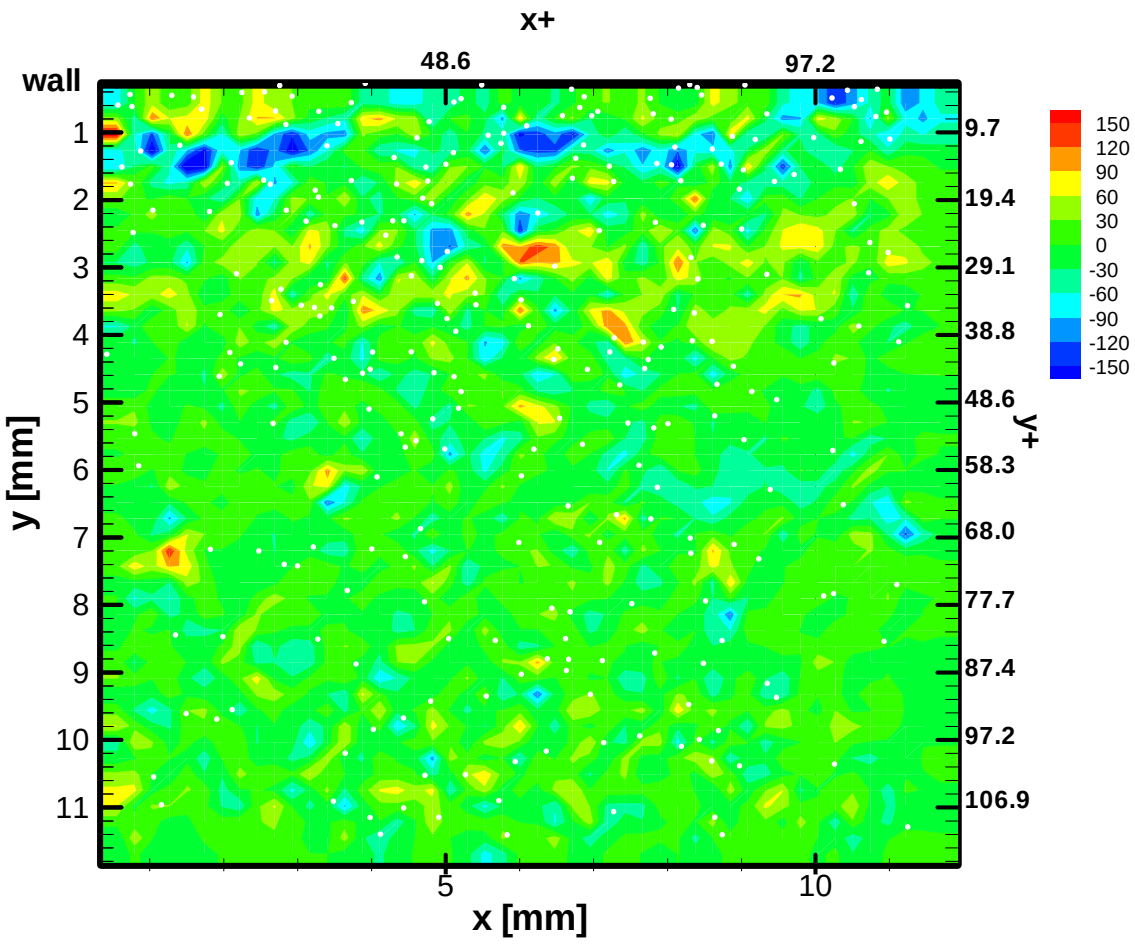

FIGURE 75. Instantaneous z-vorticity fluctuation field α = 4.4%, DR = 29.8%.

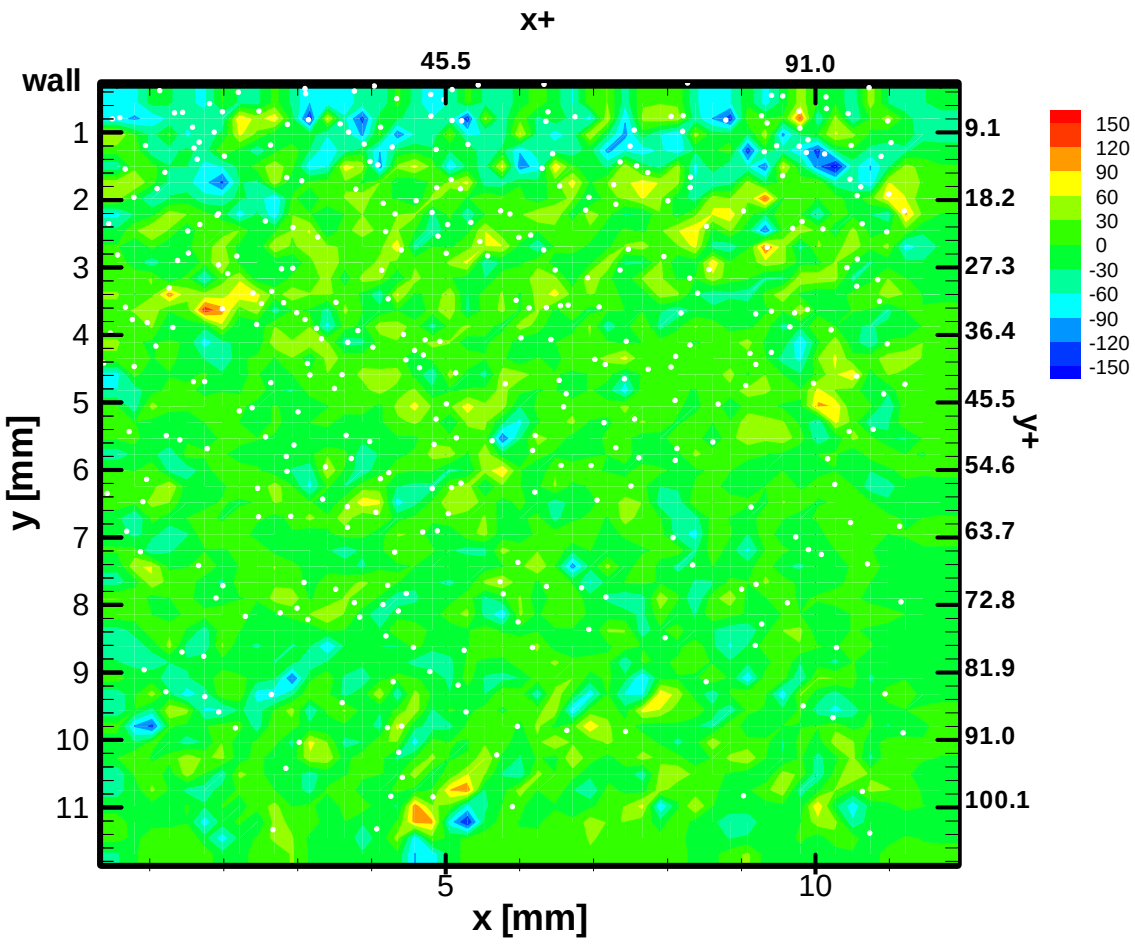

FIGURE 76. Instantaneous z-vorticity fluctuation field α = 4.9%, DR = 38.4%.

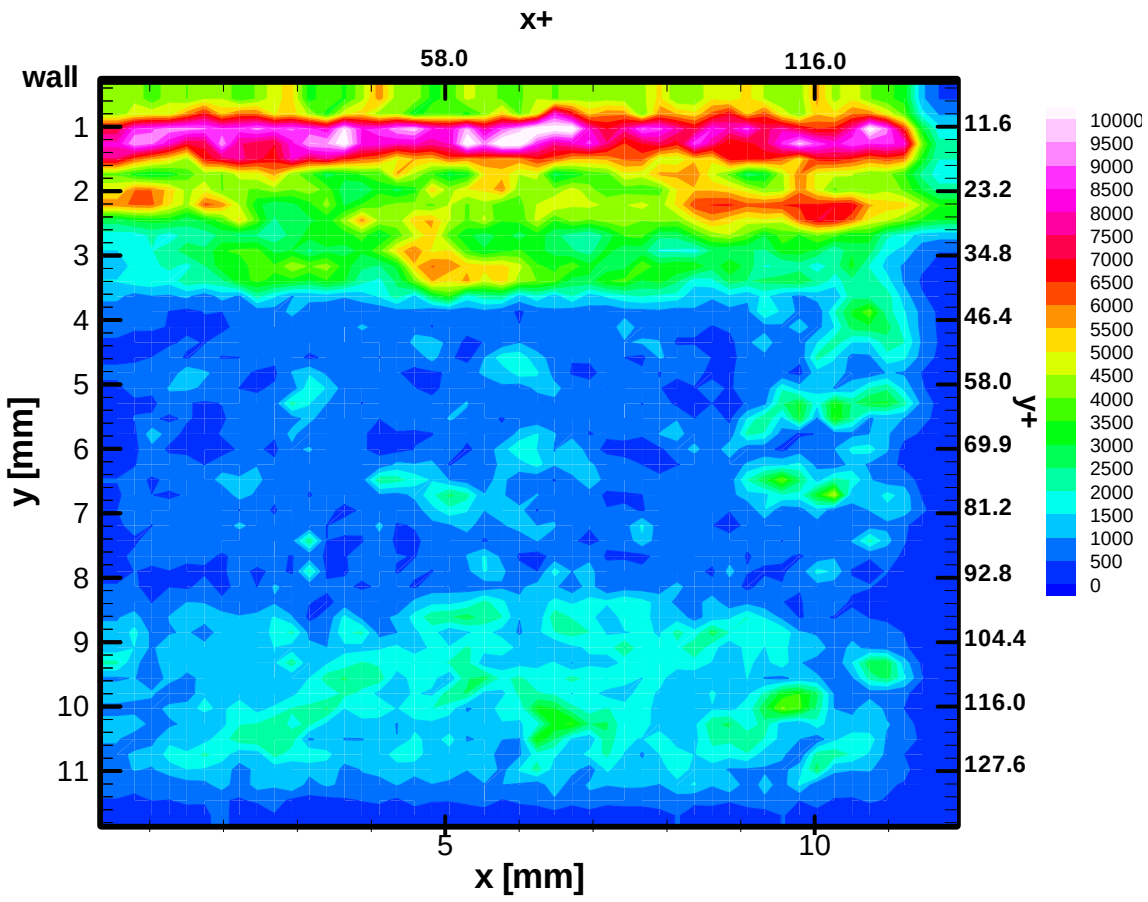

FIGURE 77. $\overline{s_{12}s_{12}}$ field for single phase flow.

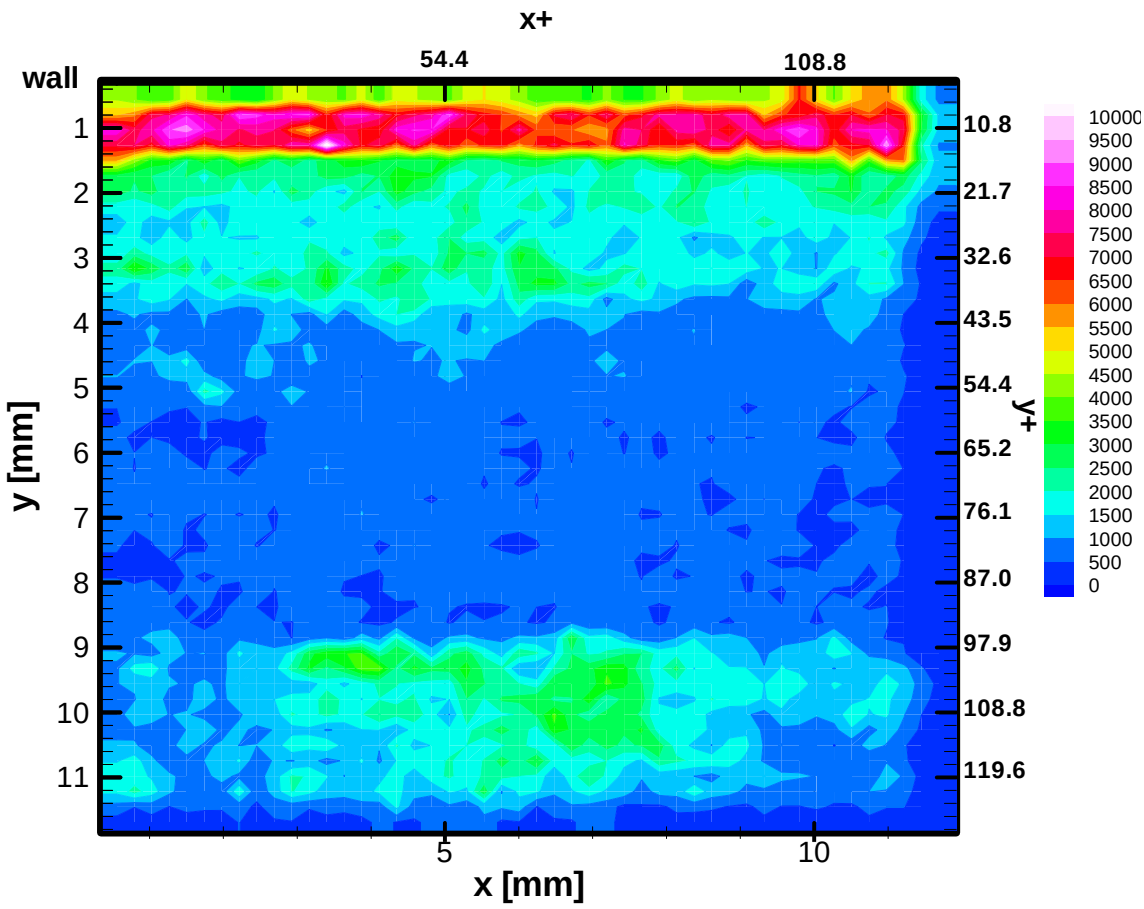

FIGURE 78. $\overline{s_{12}s_{12}}$ field for α = 2.4%, DR = 12.06%.

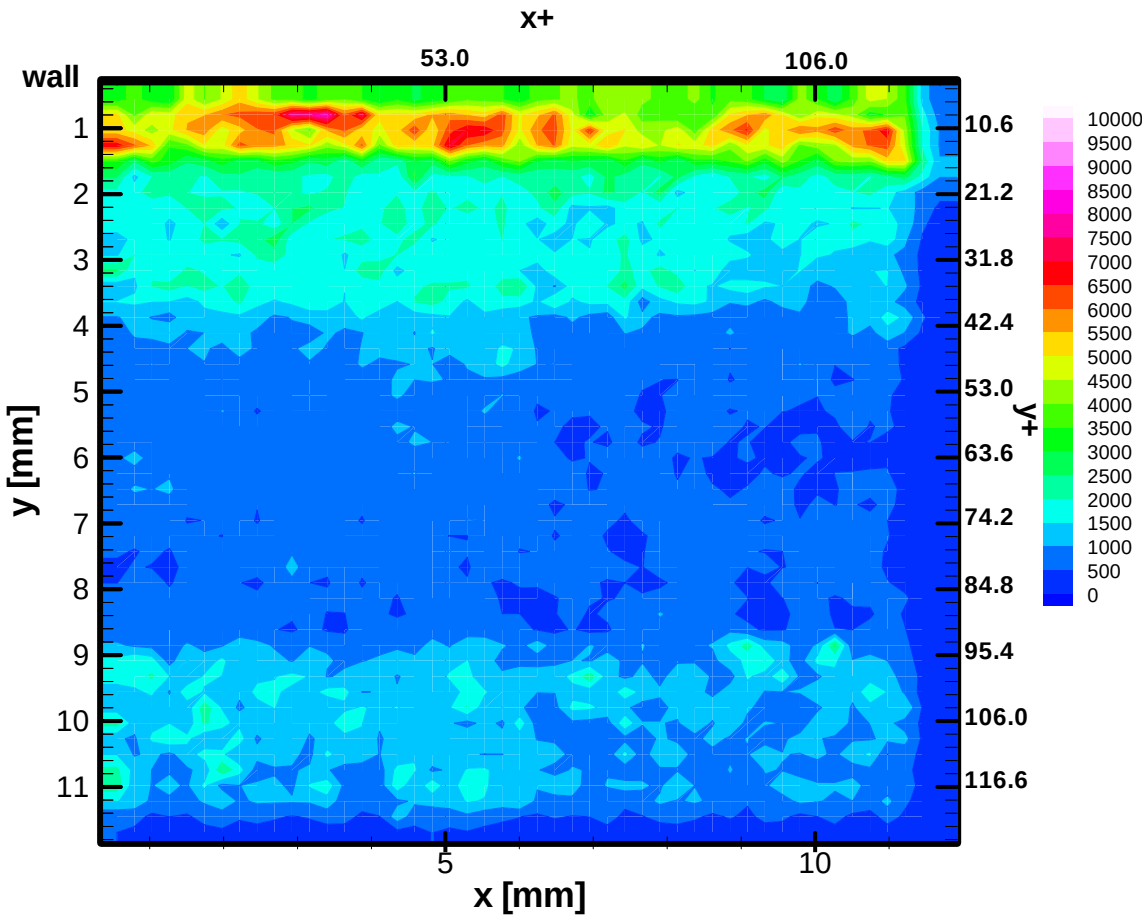

FIGURE 79. $\overline{s_{12}s_{12}}$ field for α = 3.4%, DR = 16.6%.

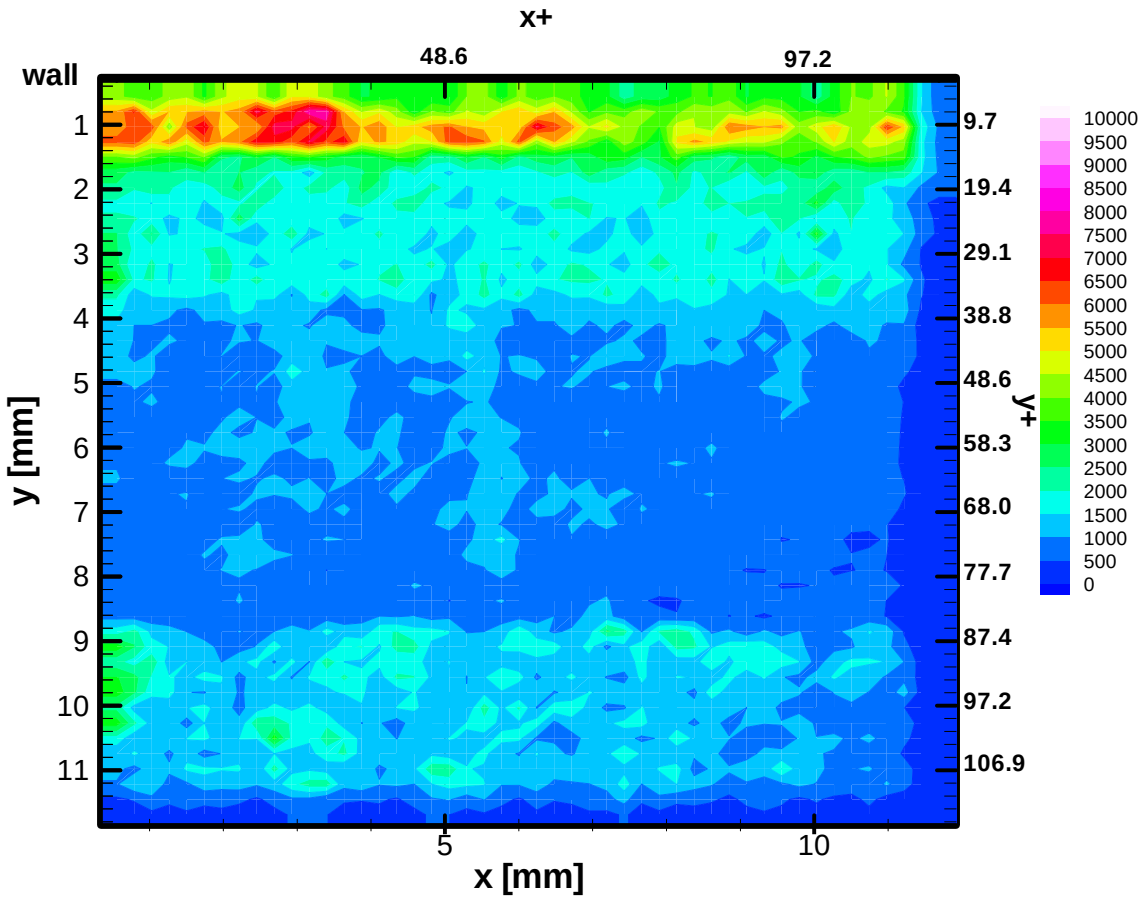

FIGURE 80. $\overline{s_{12}s_{12}}$ field for α = 4.4%, DR = 29.8%.

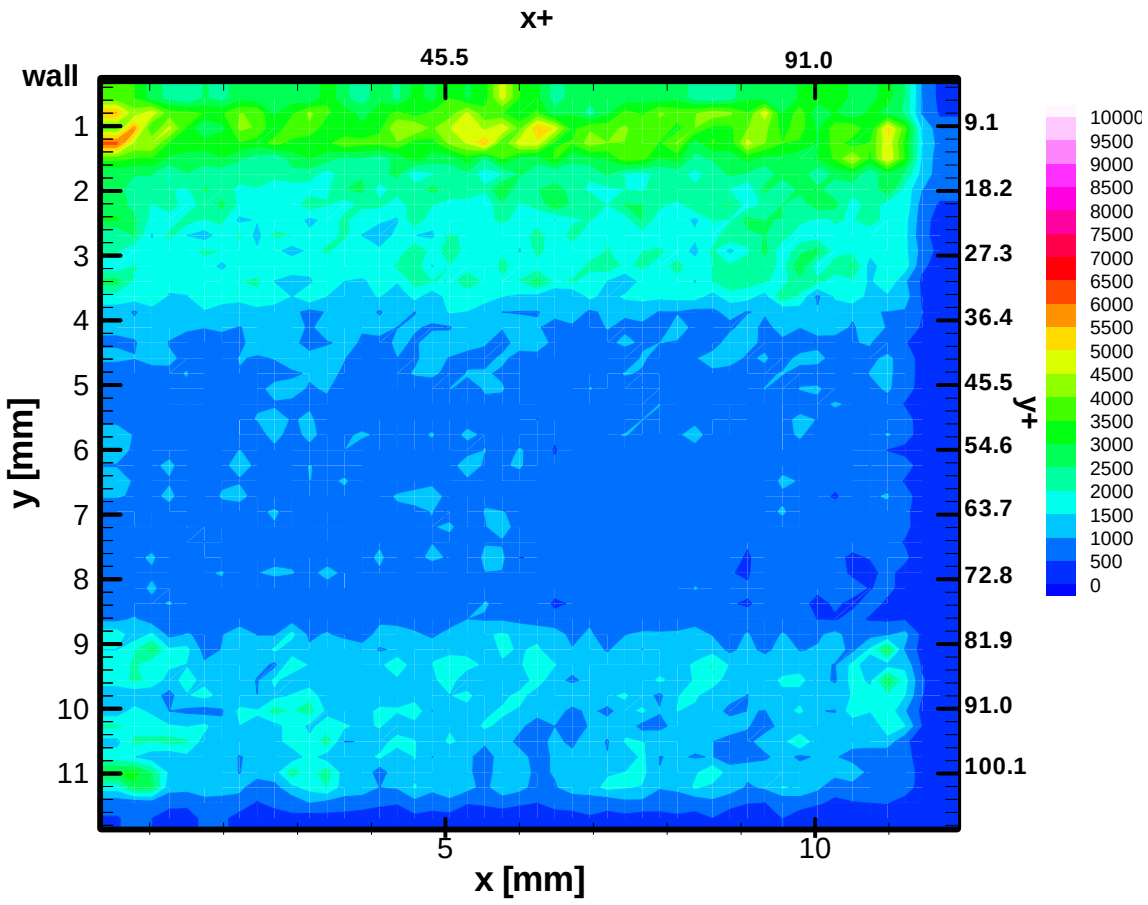

FIGURE 81. $\overline{s_{12}s_{12}}$ field for α = 4.9%, DR = 38.4%.

Energy dissipation is directly associated with strain, not with vorticity. In the present case, there is a palpable decrease in the rate of strain as the value of the void fraction increases. Since, in this research just the plane x-y was studied, just one term of the dissipation $\left(\varepsilon = 2\nu\overline{s_{ij}s_{ij}}\right)$ can be calculated. However, from the calculated term of the rate

of strain tensor, it can be observed that a decrease in the turbulent dissipation is expected as the local void fraction increases.

4.8 Turbulence Energy Production

The turbulence energy production $\left(-\overline{u'v'}\frac{\partial U}{\partial y}\right)$ was computed for single phase flow and different cases of two-phase flow with various void fraction values and it is presented in figure 82.

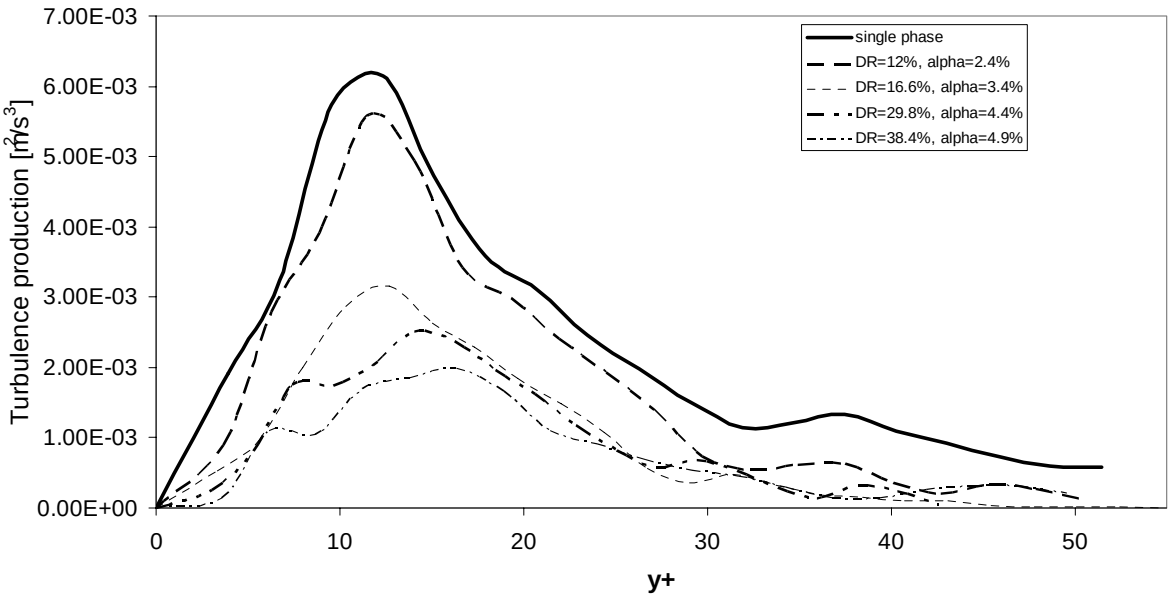

FIGURE 82. Turbulent energy production for single phase flow and two phase flow at several void fraction conditions.

As the local void fraction increases, the turbulence production decreases. This is originated from both, a decrease in the Reynolds stresses and a decrease in the average velocity gradient in the y-direction due to the microbubbles presence in the boundary layer.

4.9 Bursting Phenomena

Wall turbulence is maintained by a cycle in which streamwise vortices extract energy from the mean flow to create alternating streaks of longitudinal velocity and these streaks in turn give rise to the vortices, presumable by inflectional instabilities (Jimenez and Pinelli 1997). This cycle is local to the region below $y^+ \approx 60$ and above $y^+ \approx 20$ Jimenez and Pinelli 1999).

This process of turbulence production has been described as follows: Low- and high-speed streaks, which consist mostly of a spanwise modulation of the streamwise velocity are occasionally lifted away form the wall region (ejection). They start to oscillate, and eventually go through a violent breakup, during which approximately 70% of the total turbulence production takes place. The sequence of events –liftup, oscillation, and breakup- is referred as bursting process. Typically, a bursting process is followed by an inrush of high-speed fluid originated away from the wall into the wall region (sweep) (Kim and Spalart 1987). Sweeps are considered to contribute to the generation of skin friction (Kawahara *et al.* 1998).

The quadrant decomposition technique is used to detect the turbulence producing events Q_2 (ejection or burst) and Q_4 (sweeps). Figures 83 and 84 show instantaneous velocity fields where color is used to point out the streaks of streamwise velocity. Burst (u' < 0, v' > 0)and sweeps (u' > 0, v' < 0) are encircled by a solid line for single phase and two-phase flow respectively.

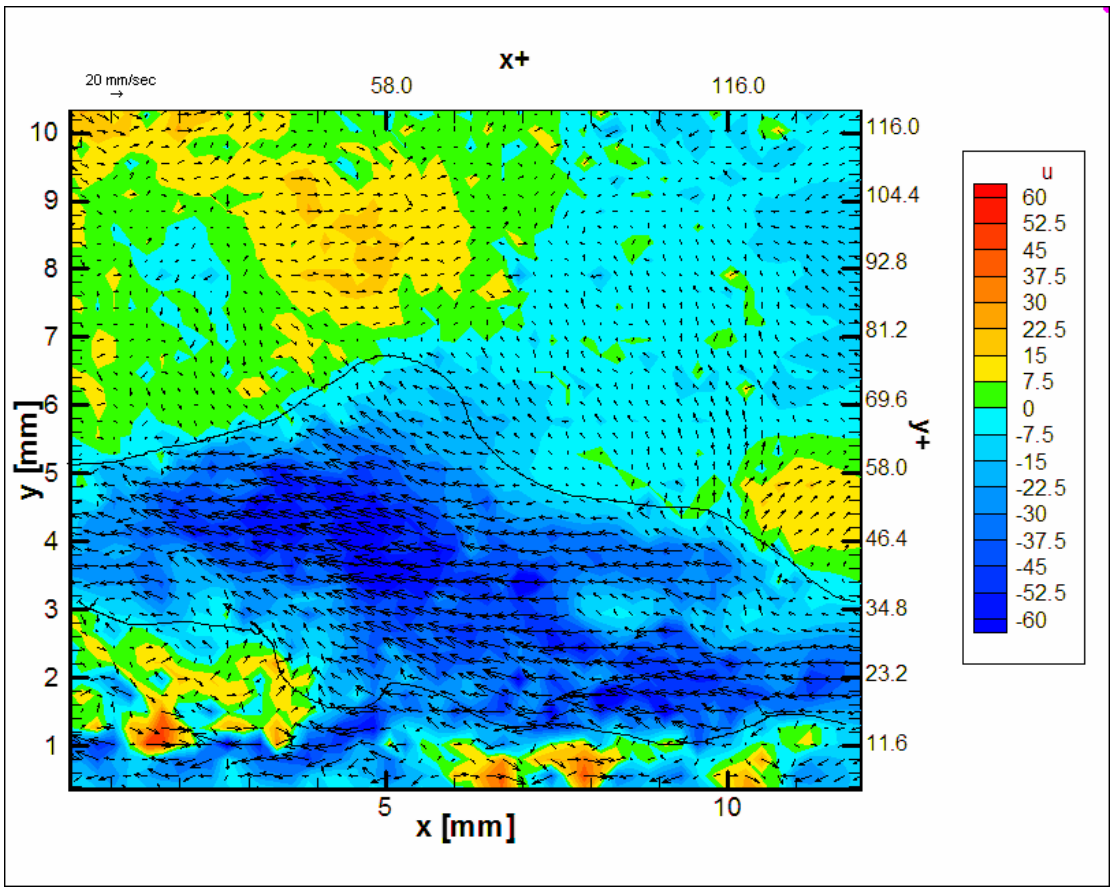

FIGURE 83. Burst and sweeps in a fluctuating velocity field for single phase.

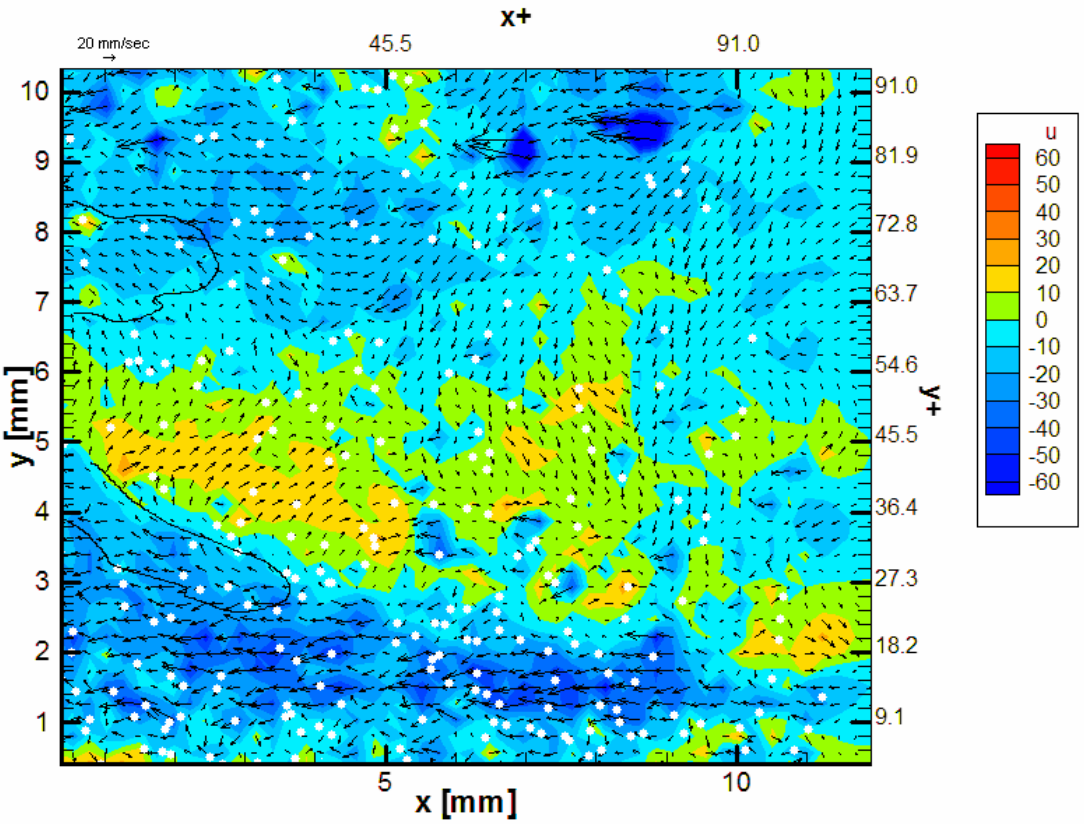

FIGURE 84. Burst and sweeps in a fluctuating velocity field for α = 4.9%, DR = 38.4%.

In can be observed a strong suppression of turbulence producing events were microbubbles are present. Since the quadrant analysis technique has been traditionally used for velocity measurements made by hot wire anemometry, they are performed in stationary point in space. Using PIV measurements, a complete velocity field can be used to carry out such kind of analysis. In this work, a modification of the traditional methods implemented for quadrant analysis is proposed. Such method is called “Dominant event”

detection. In this method, the fluctuating components of the velocity are discriminated using the traditional quadrant analysis. However, the dominant event i.e. the event that has the larger incidence is recorded for the final statistics.

The use of a threshold value (H) for better classification of events is also used. An optimum value of 4.5 for burst and 2.5 for sweeps was recommended by Lu and Willmarth (1973) and are used in this work. Figures 85 to 88 show the quadrant distribution for single phase flow using the three different variants of the quadrant analysis.

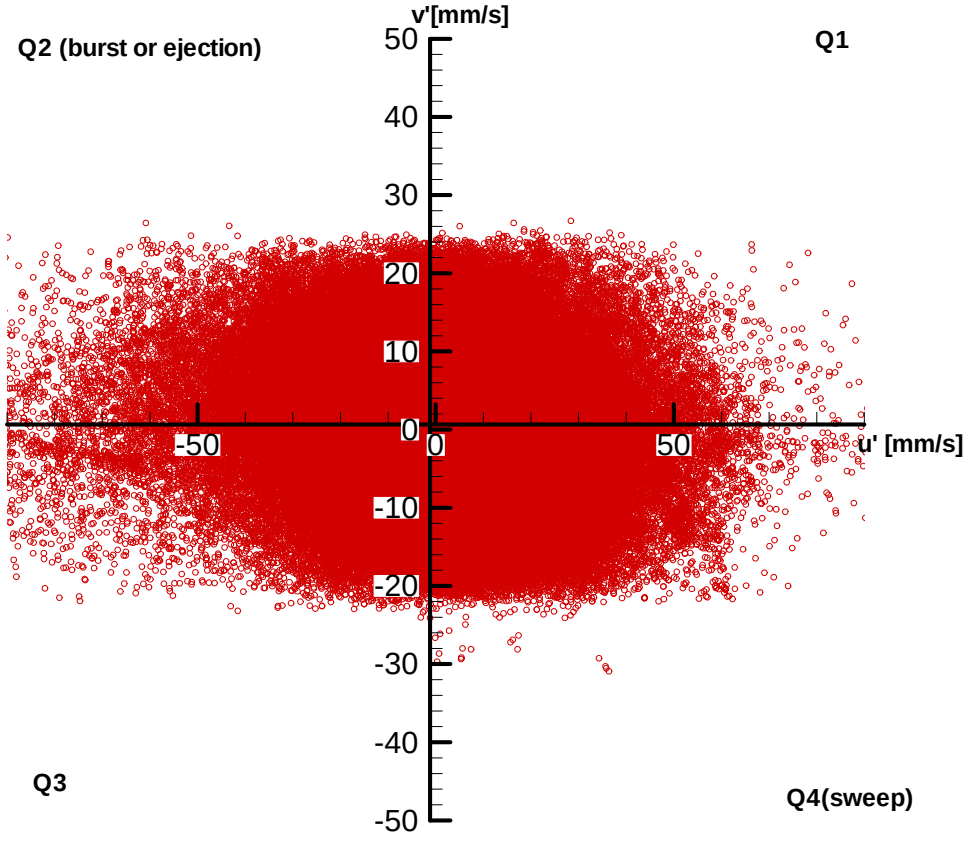

FIGURE 85. Quadrant analysis discrimination for single phase flow.

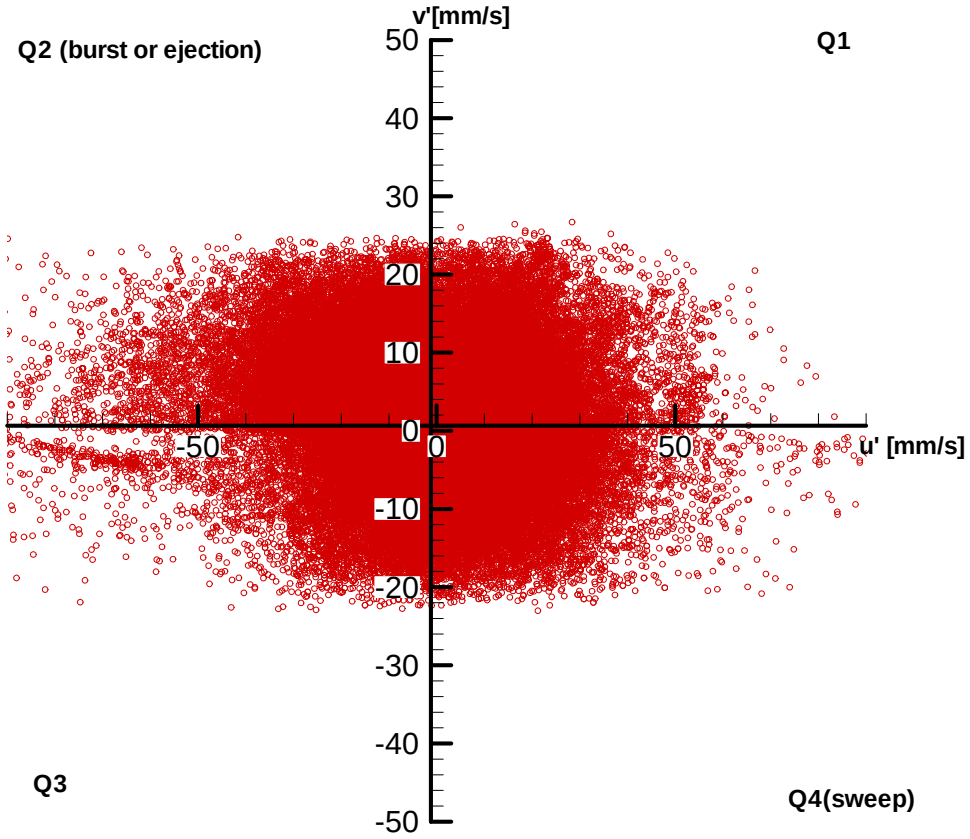

FIGURE 86. Quadrant analysis discrimination using the “dominant event” criterion for single phase flow.

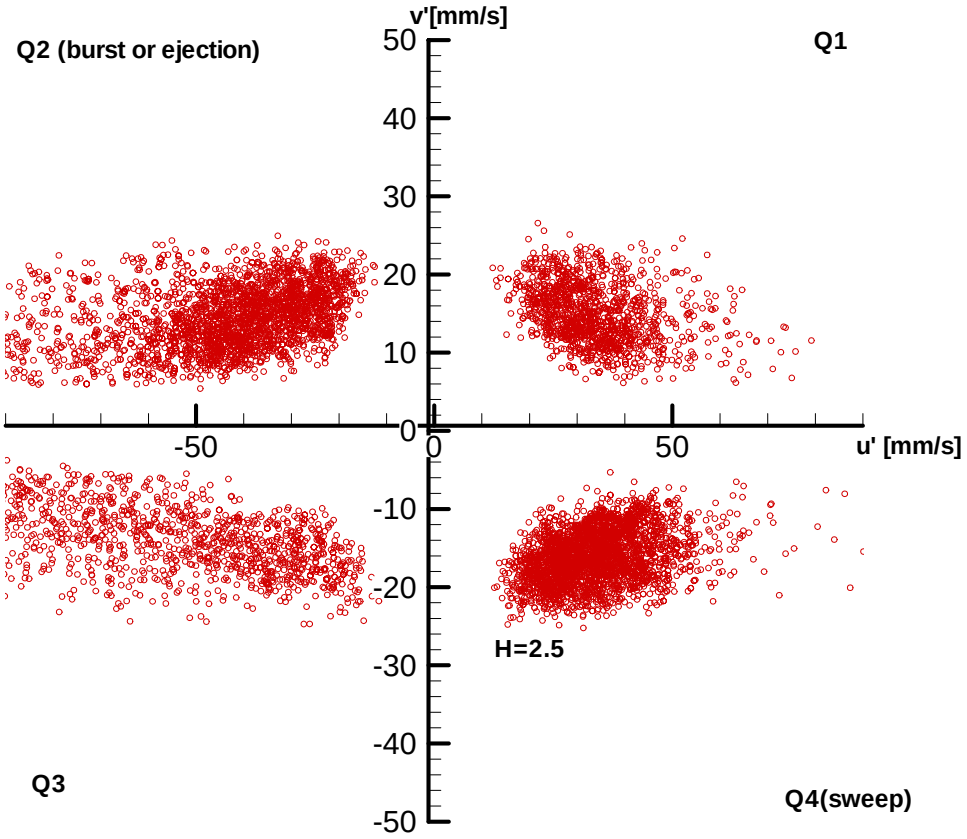

FIGURE 87. Quadrant analysis discrimination using a threshold value (H = 2.5) for single phase flow.

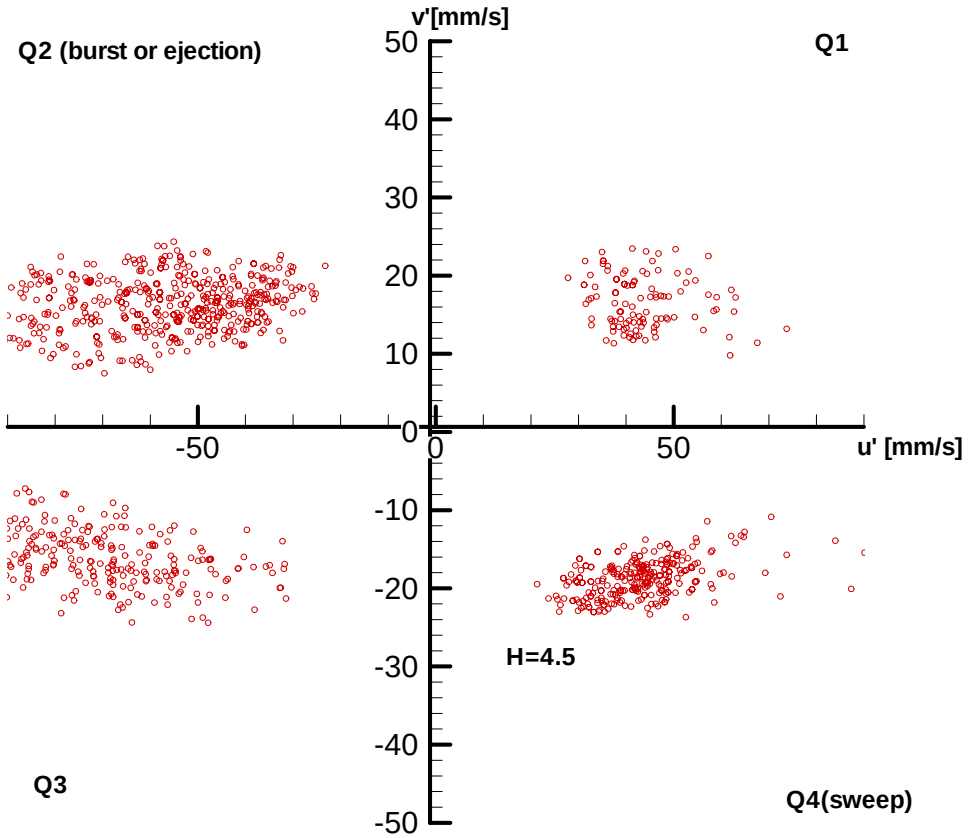

FIGURE 88. Quadrant analysis discrimination using a threshold value (H = 4.5) for single phase flow.

The average distribution of the events in percentage for the different techniques used is presented in table 22.

	Q_1[%]	Q_2[%]	Q_3[%]	Q_4[%]
Quadrant analysis	22.9	27.5	21.6	28
Dominant event	17.2	35.5	14.6	32.7
H = 2.5	14.4	31.6	18.7	35.3
H = 4.5	6.5	40.2	36.6	16.7

TABLE 22. Quadrant analysis results for single phase flow

Fraction contribution from each event is plotted versus time for each technique in figures 89 to 91.

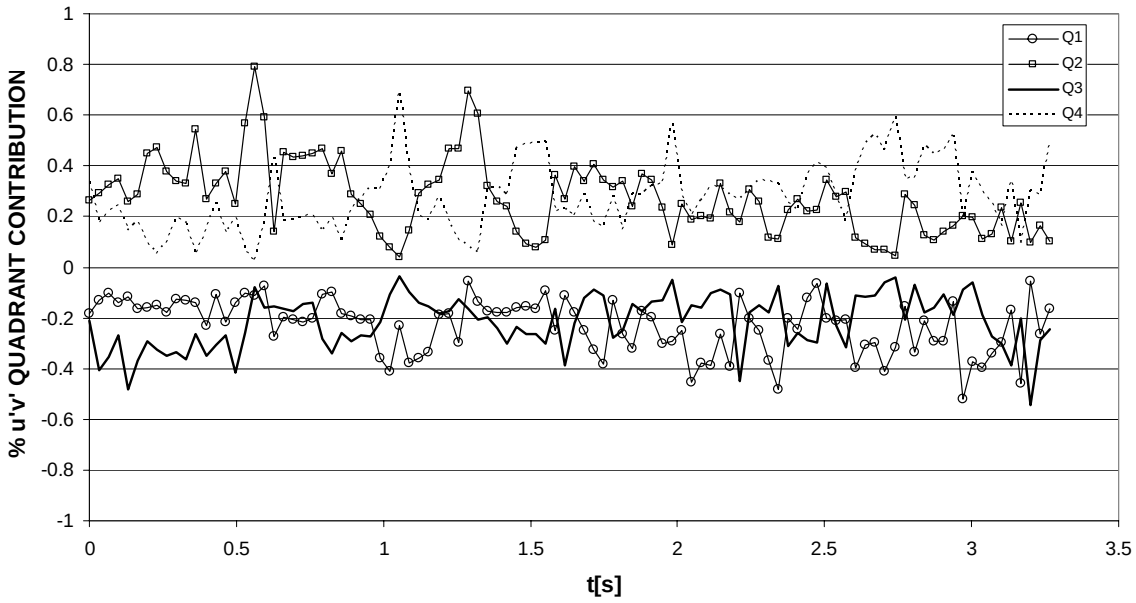

FIGURE 89. Quadrant contribution to Reynolds stress vs. time for single phase flow.

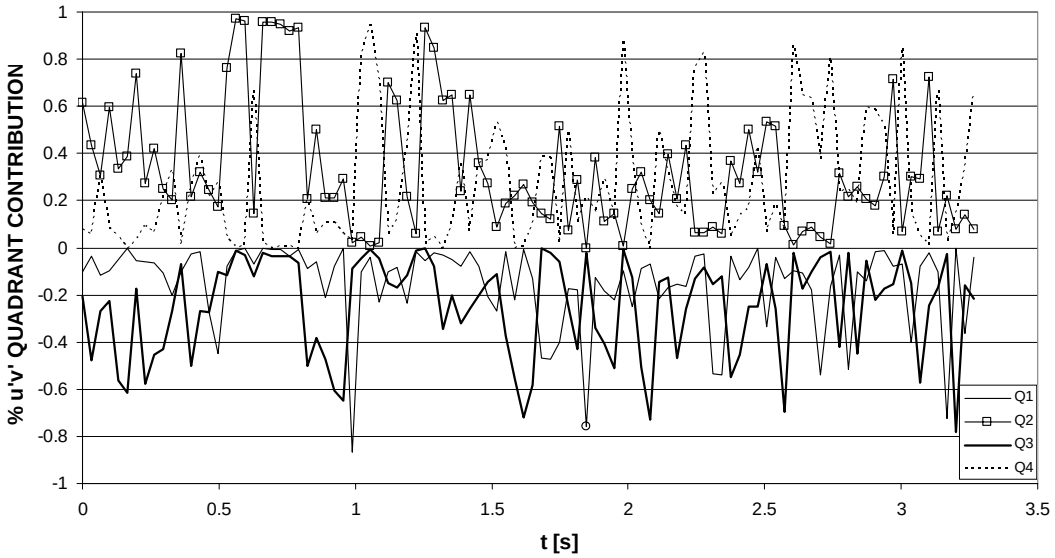

FIGURE 90. Quadrant contribution to Reynolds stress vs. time for single phase flow (H = 2.5).

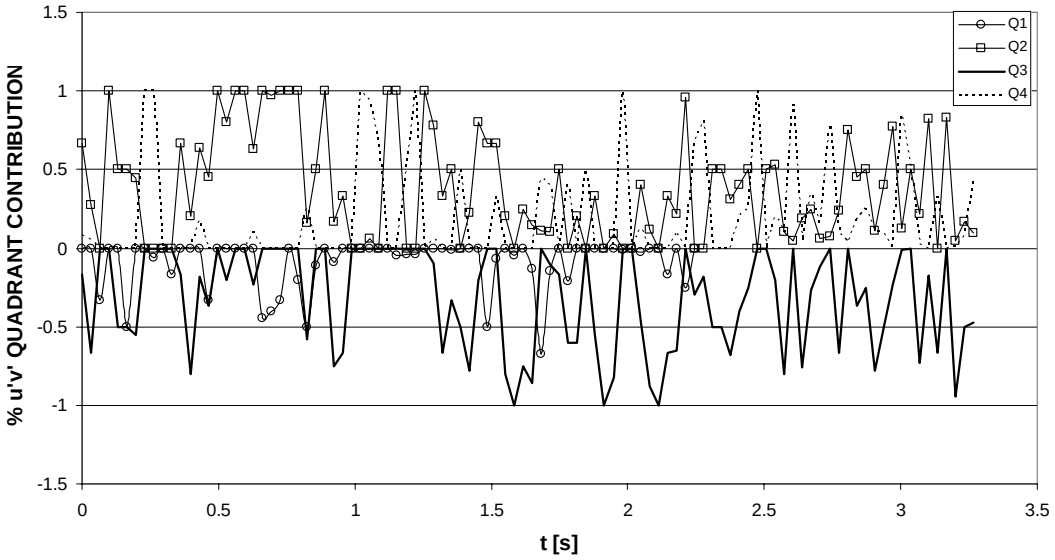

FIGURE 91. Quadrant contribution to Reynolds stress vs. time for single phase flow (H = 4.5).

All the techniques used show that burst (Q_2) and sweeps (Q_4) are the predominant events for single phase flow. Using a threshold value of 2.5, a larger percentage of sweeps is found as was expected. On the other hand the use of H = 4.5 gives a larger percentage of bursts. No big difference between the number of burst and sweeps is found using neither the traditional quadrant analysis nor the dominant event criterion. Figures 92 to 95 show the quadrant distribution for α = 4.9%, DR = 38.4% flow using the three different variants of the quadrant analysis.

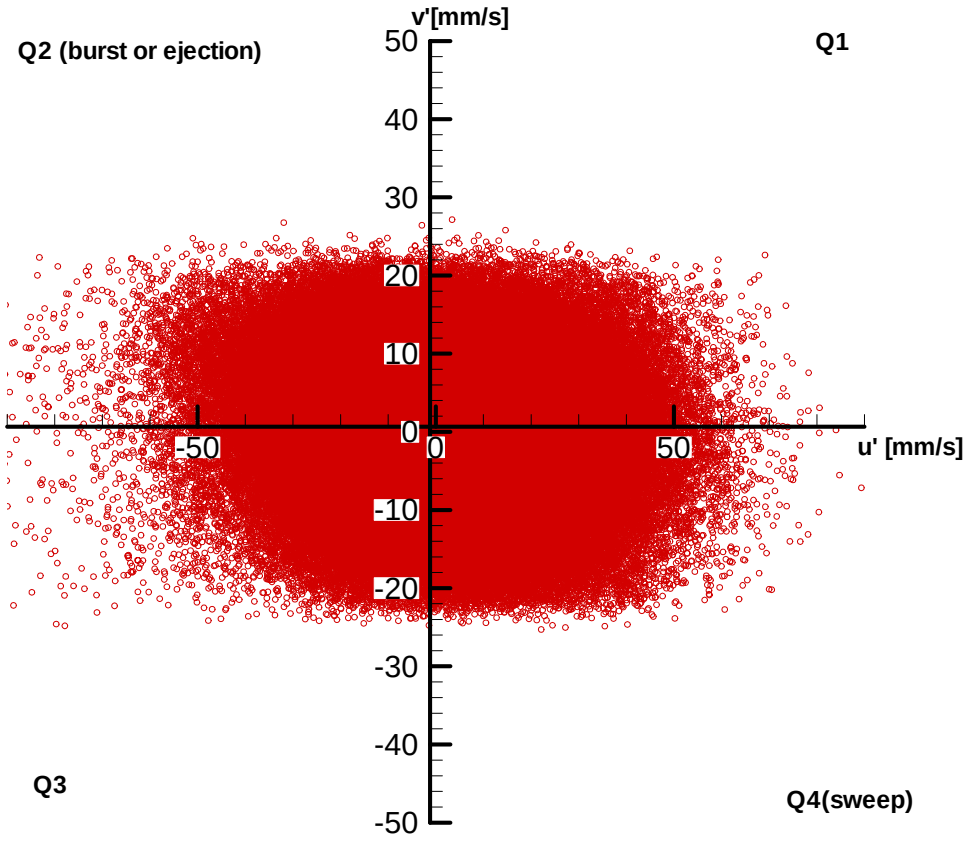

FIGURE 92. Quadrant analysis discrimination for α = 4.9%, DR = 38.4%.

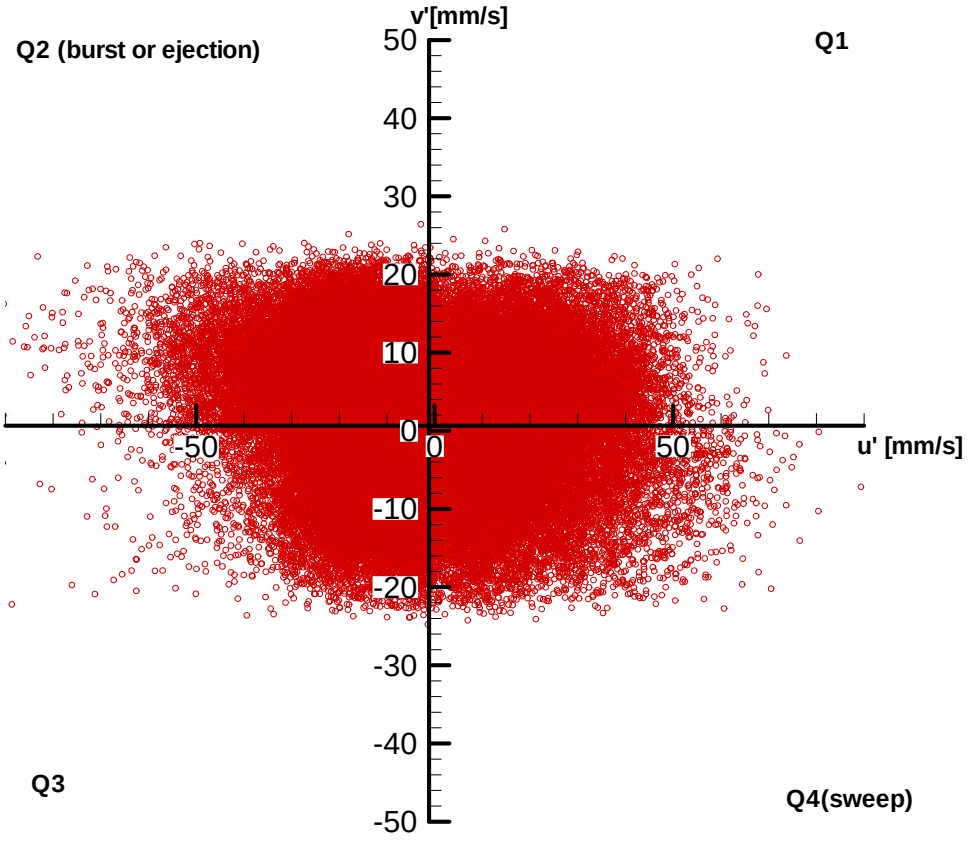

FIGURE 93. Quadrant analysis discrimination using the “dominant event” criterion for α = 4.9%, DR = 38.4%.

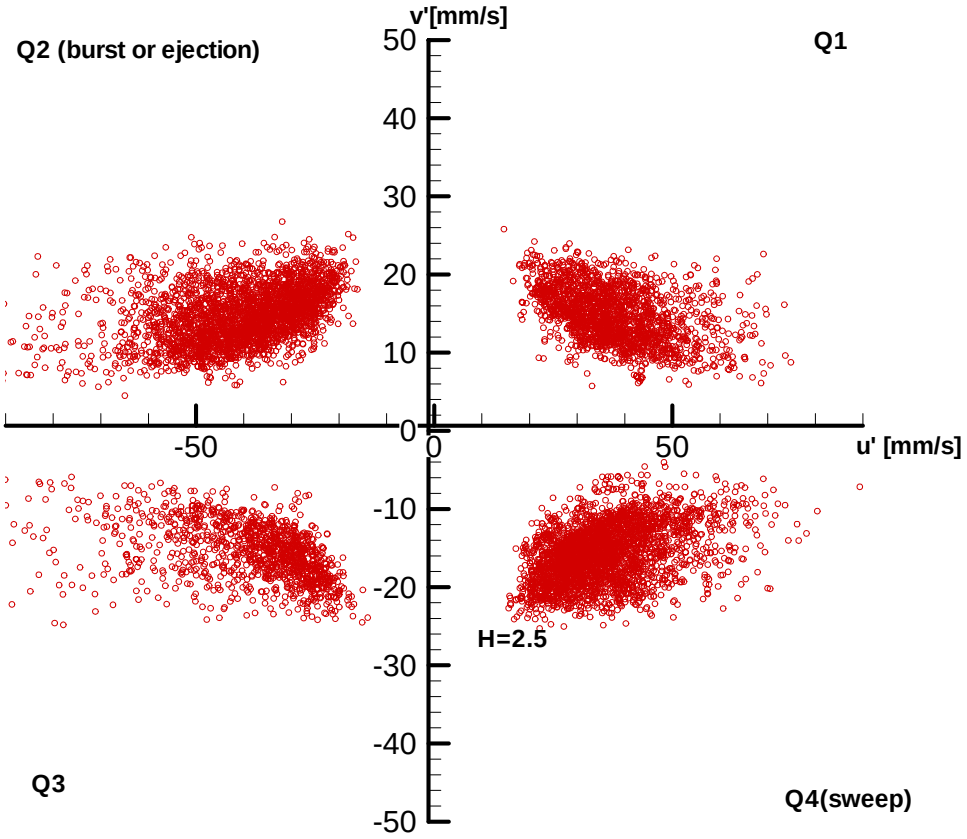

FIGURE 94. Quadrant analysis discrimination using H = 2.5 criterion for α = 4.9%, DR = 38.4%.

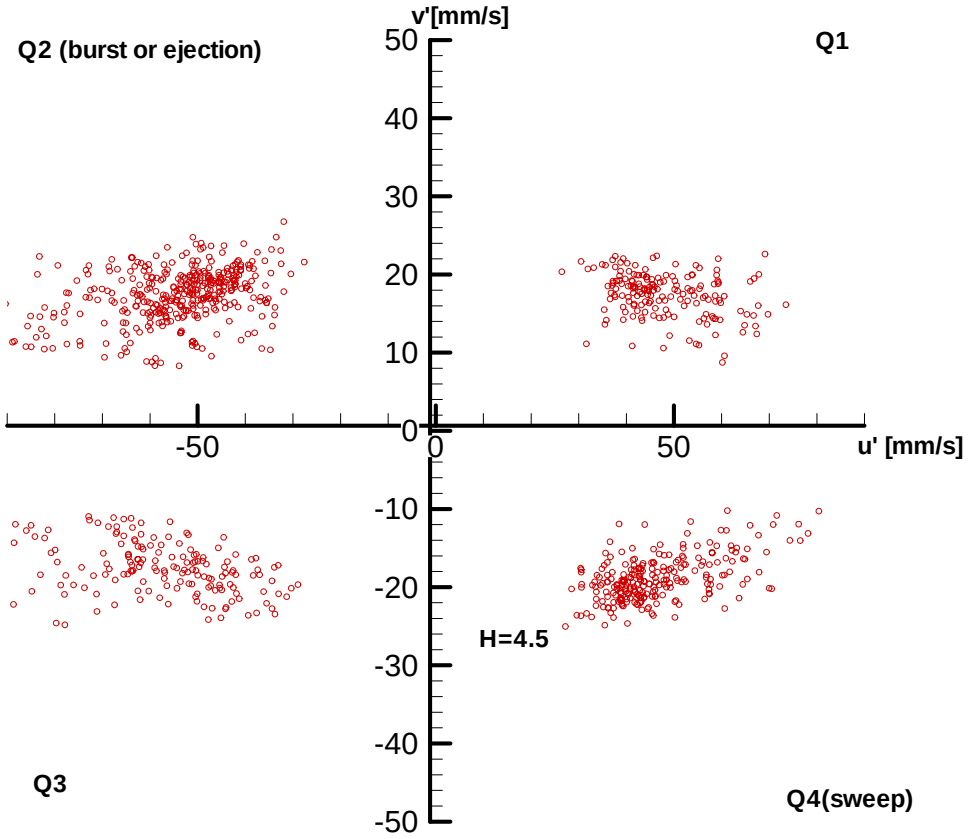

FIGURE 95. Quadrant analysis discrimination using H = 4.5 criterion for α = 4.9%, DR = 38.4%.

The average distribution of the events in percentage form different techniques used for α = 4.9%, DR = 38.4% is presented in table 23.

	Q_1[%]	Q_2[%]	Q_3[%]	Q_4[%]
Quadrant analysis	22.7	28.2	23.2	25.8
Dominant event	16.4	36.7	15.2	31.7
H = 2.5	23	31.2	14	31.7
H = 4.5	17	38.8	19.6	24.6

TABLE 23. Quadrant analysis results for α = 4.9%, DR = 38.4%

Fraction contribution from each event is plotted versus time for each technique in figures 96 to 98.

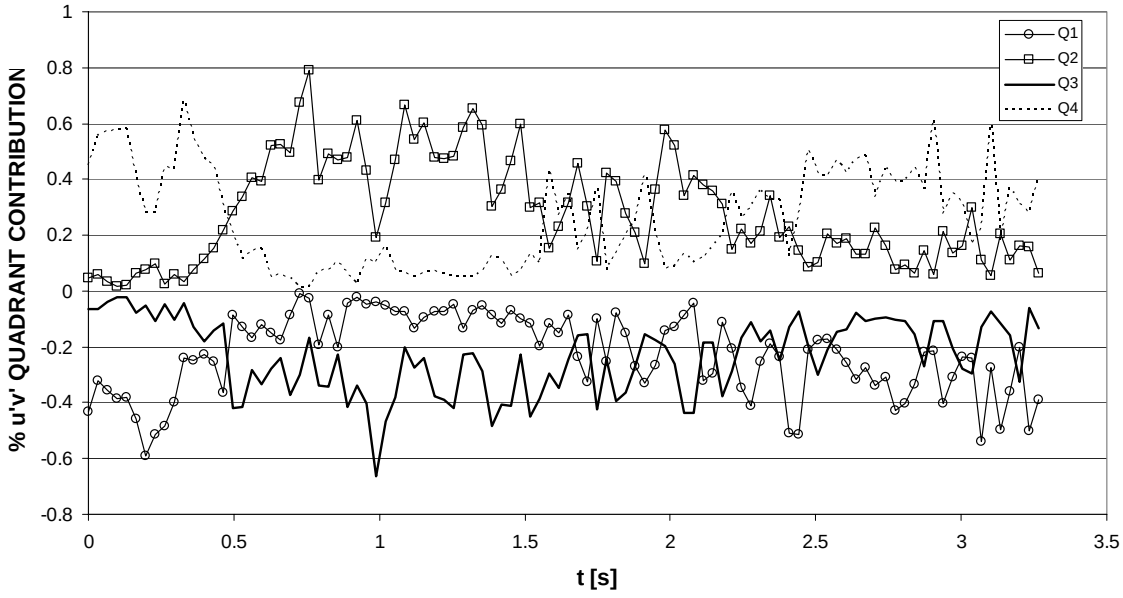

FIGURE 96. Quadrant contribution to Reynolds stress vs. time for α = 4.9%, DR = 38.4%.

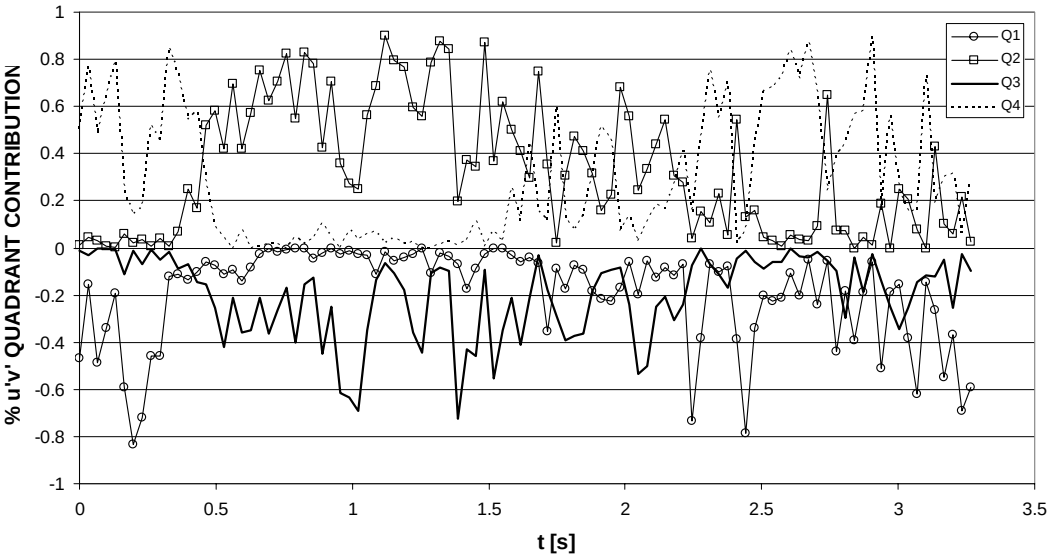

FIGURE 97. Quadrant contribution to Reynolds stress vs. time for α = 4.9%, DR = 38.4% (H = 2.5).

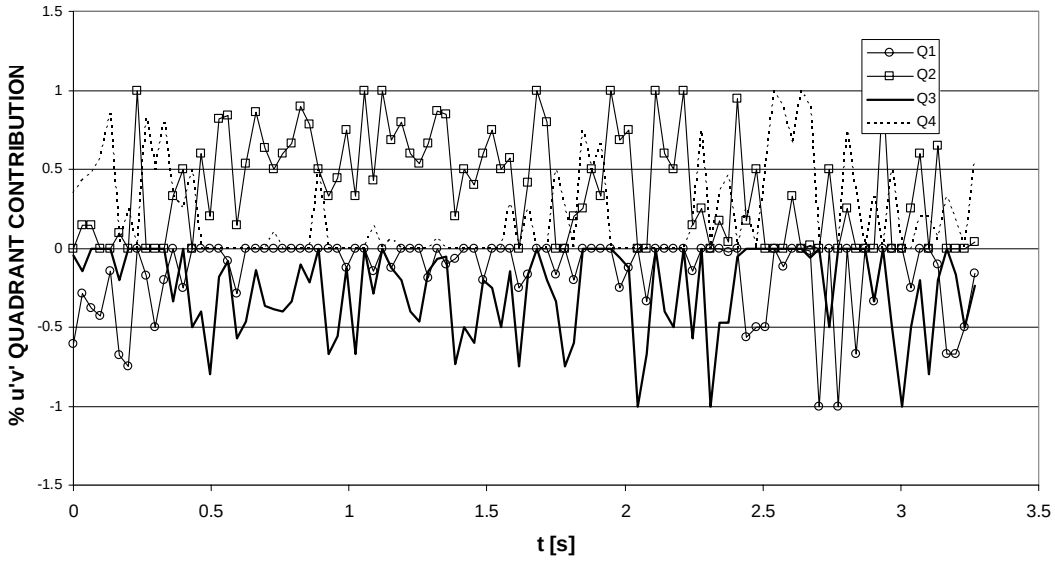

FIGURE 98. Quadrant contribution to Reynolds stress vs. time for α = 4.9%, DR = 38.4% (H = 4.5).

For two-phase flow, a decrease in the Q_4 events (sweeps) is observed, as well as an increase in the Q_2 events (burst). This decrease in the sweeps events can help to explain the drag reduction effect or the microbubbles presence within the boundary layer since those events (sweeps) are the principal facilitators of the skin friction production.

As was stated before, the quadrant analysis for bursting detection has been traditionally used in measurements performed by hot wire anemometry. In the case of PIV, there is a complete velocity field available that can be analyzed in the time domain. Considering a fixed point in the velocity field, and following its velocity variations in time, a technique analogous to hot wire measurements can be implemented.

Several wire lengths have been used in different experiments to detect turbulent producing events. Willmarth and Sharma (1984) used wires with lengths that varied from 25 μm to 100 μm. Antonia and Krogstad (2001) used a wire with 0.5 mm length. Krogstad *et al.* (1992) used a wire with 0.35 mm length, and Bogard and Tiederman (1986) used a wire of 0.5 mm length. In this case, the grid size for our PIV measurements has 0.24 mm length. Results for the quadrant analysis technique using this method are shown in figures 99 to 102.

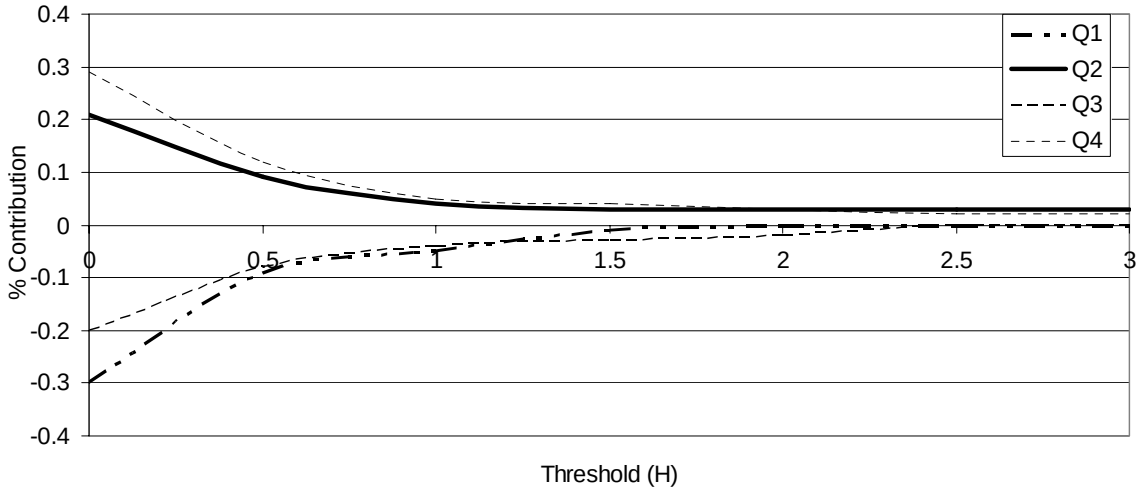

FIGURE 99. Quadrant contribution at different threshold values at $x^+ = 69.7$ and $y^+ = 9.2$ for single phase.

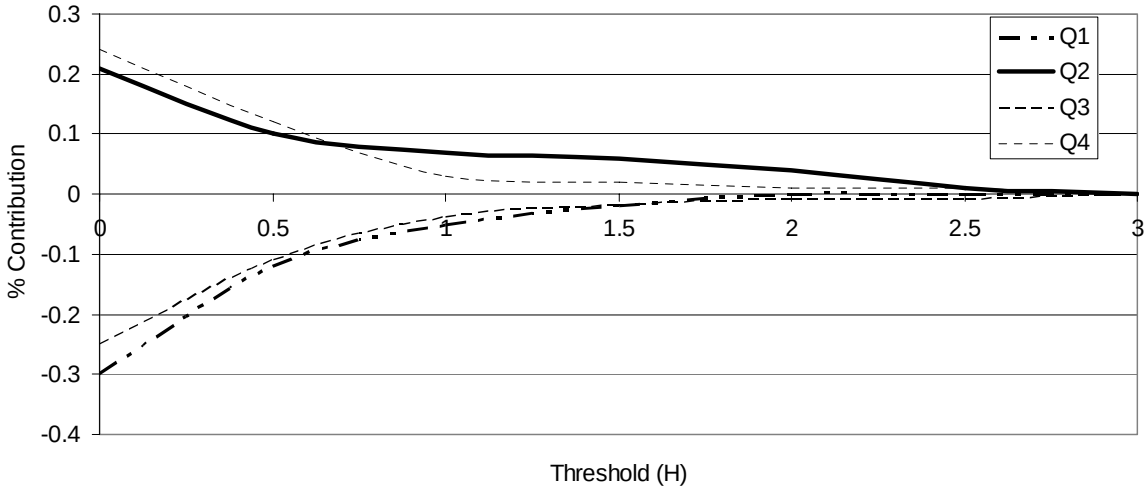

FIGURE 100. Quadrant contribution at different threshold values at $x^+ = 69.7$ and $y^+ = 9.2$ for $\alpha = 4.9\%$, DR = 38.4%.

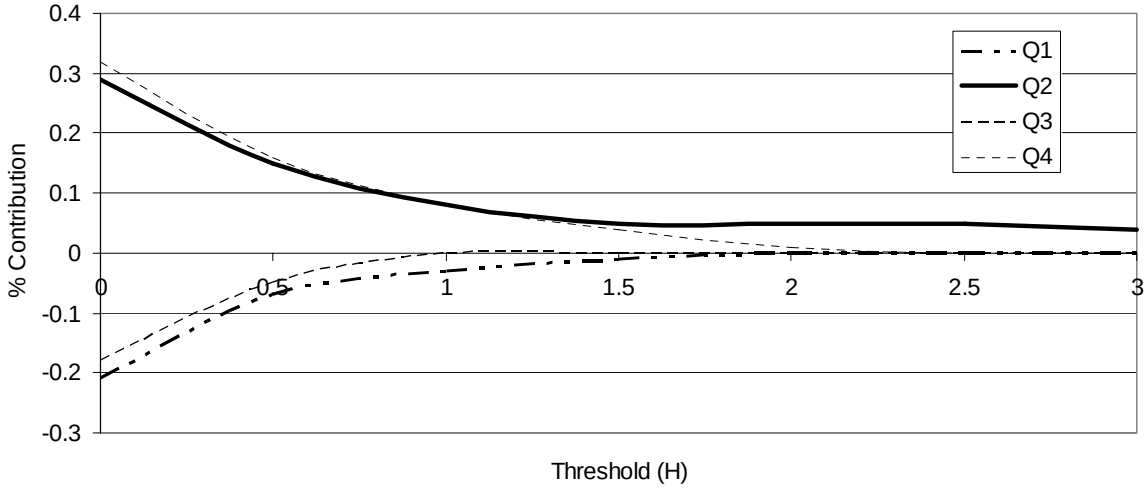

FIGURE 101. Quadrant contribution at different threshold values at $x^+ = 69.7$ and $y^+ = 25.7$ for single phase.

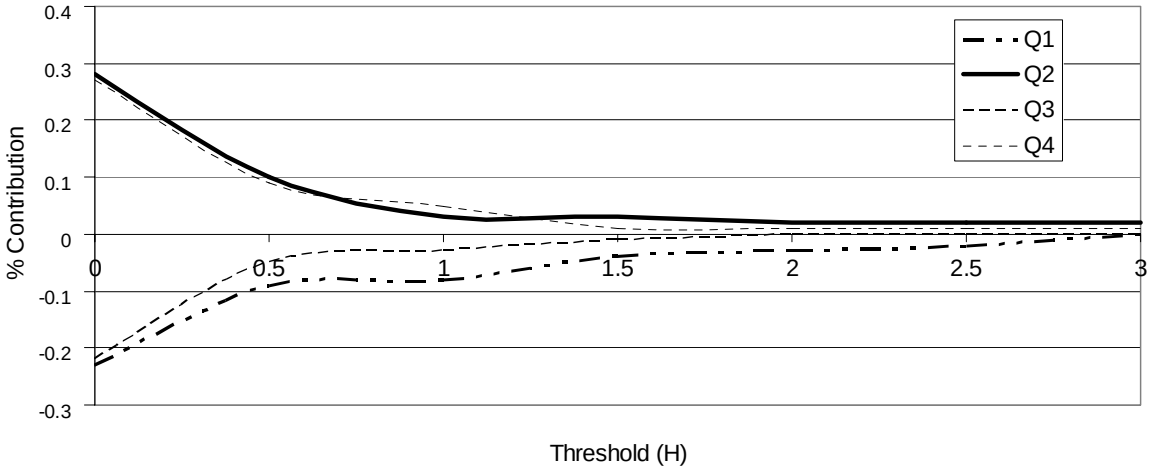

FIGURE 102. Quadrant contribution at different threshold values at $x^+ = 69.7$ and $y^+ = 25.7$ for $\alpha = 4.9\%$, DR = 38.4%.

4.10 Visualization Techniques

Three different visualization techniques were used to try to elucidate the presence of coherent structures in the velocity fields. Four instantaneous fluctuating velocity fields for single phase flow are presented in figures 103 to 106. The traditional Reynolds decomposition, a modified Reynolds decomposition and spatial decomposition techniques were used to obtain these fields.

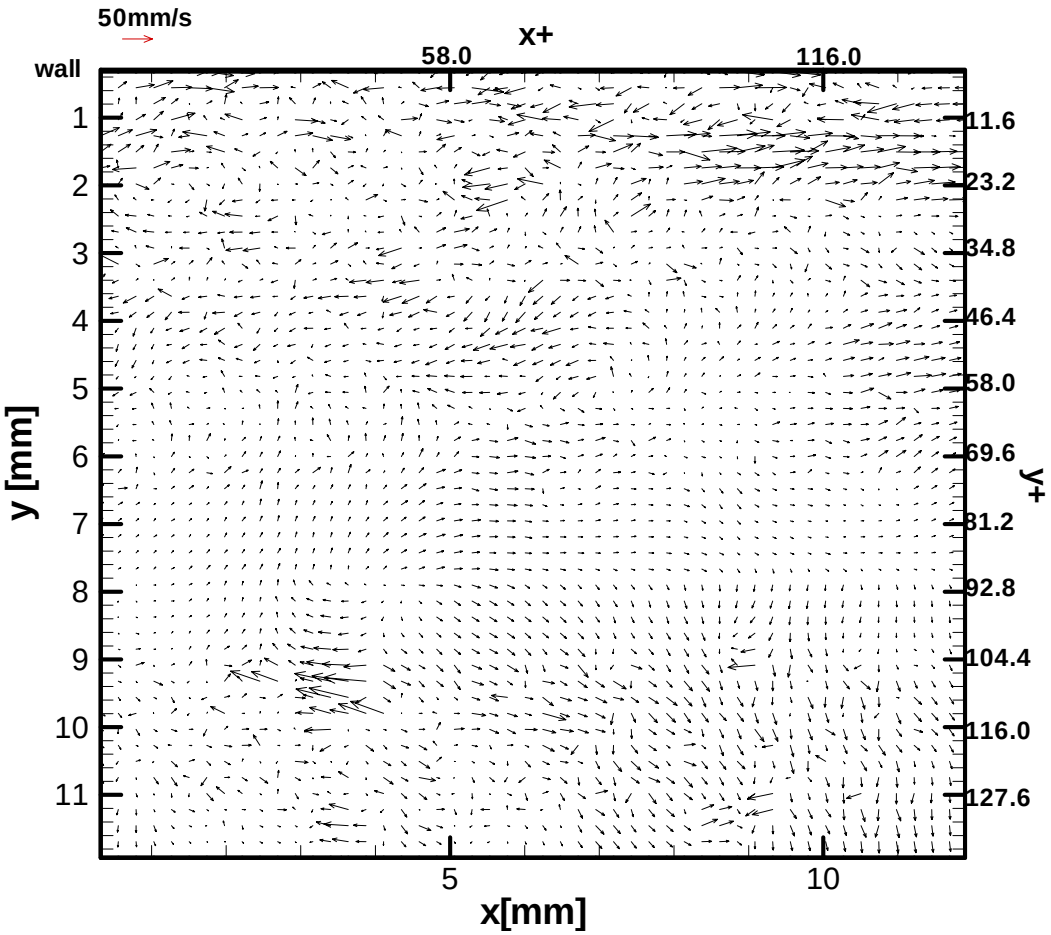

FIGURE 103. Instantaneous fluctuating velocity field for single phase obtained using the Reynolds decomposition.

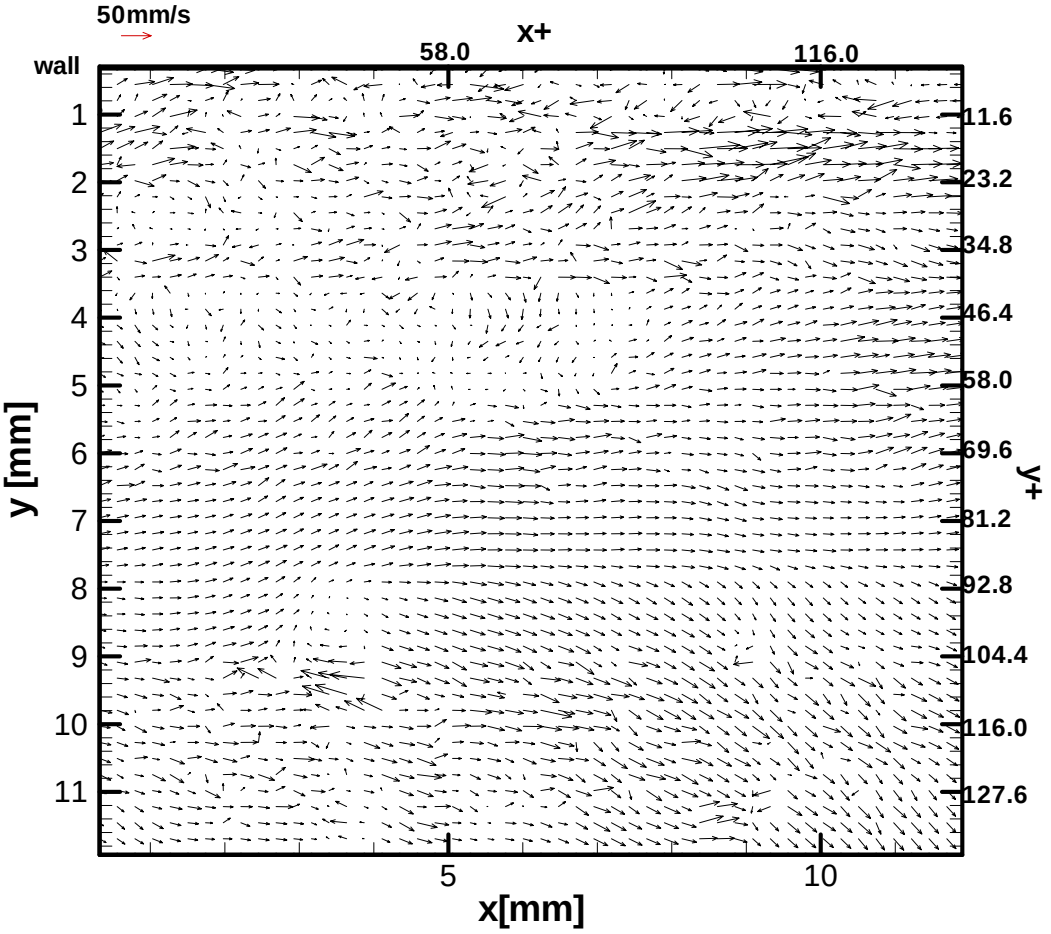

FIGURE 104. Instantaneous fluctuating velocity field for single phase obtained using the modified Reynolds decomposition (-0.92U).

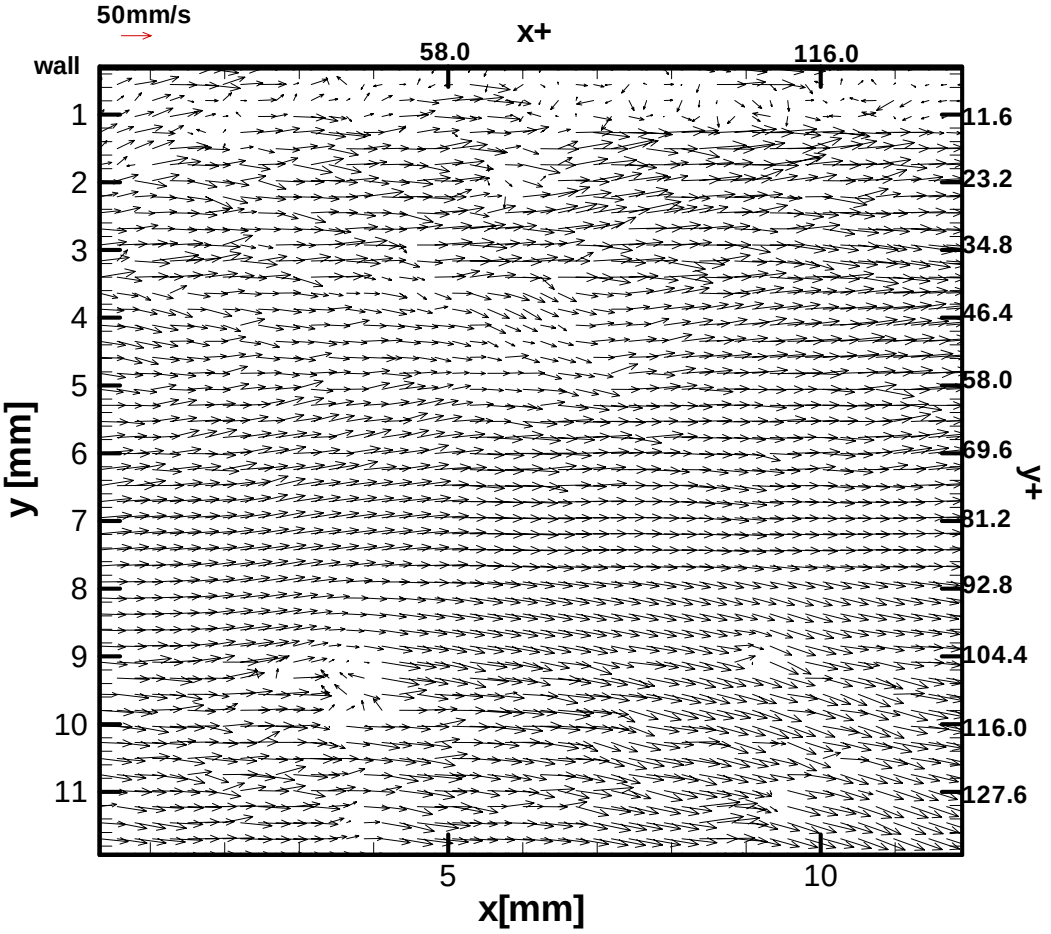

FIGURE 105. Instantaneous fluctuating velocity field for single phase obtained using the modified Reynolds decomposition (-0.75U).

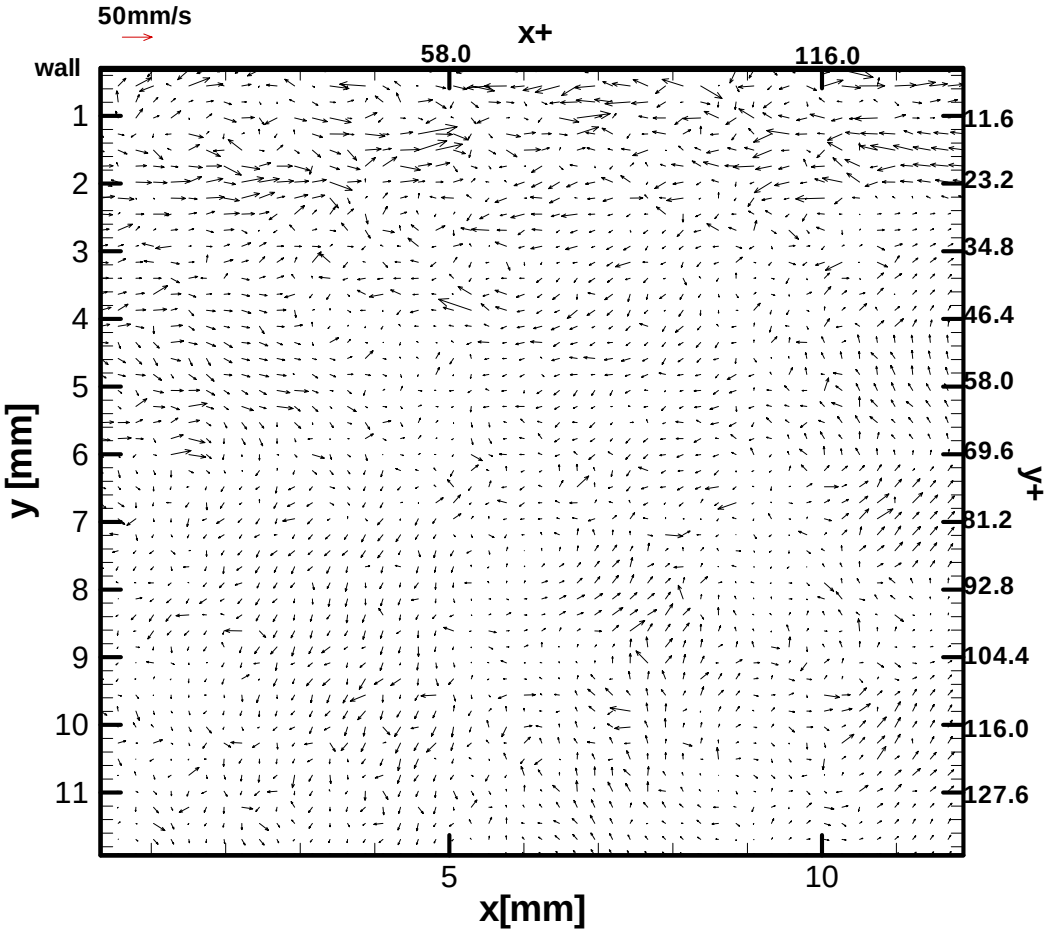

FIGURE 106. Instantaneous fluctuating velocity field for single phase obtained using the spatial decomposition.

For two-phase flow, results using the same techniques are presented in figures 107 to 110. It is evident that for flow structure visualization, the traditional Reynolds decomposition is not the best option. The spatial decomposition appears to be the best one for flow structure visualization in instantaneous velocity fields.

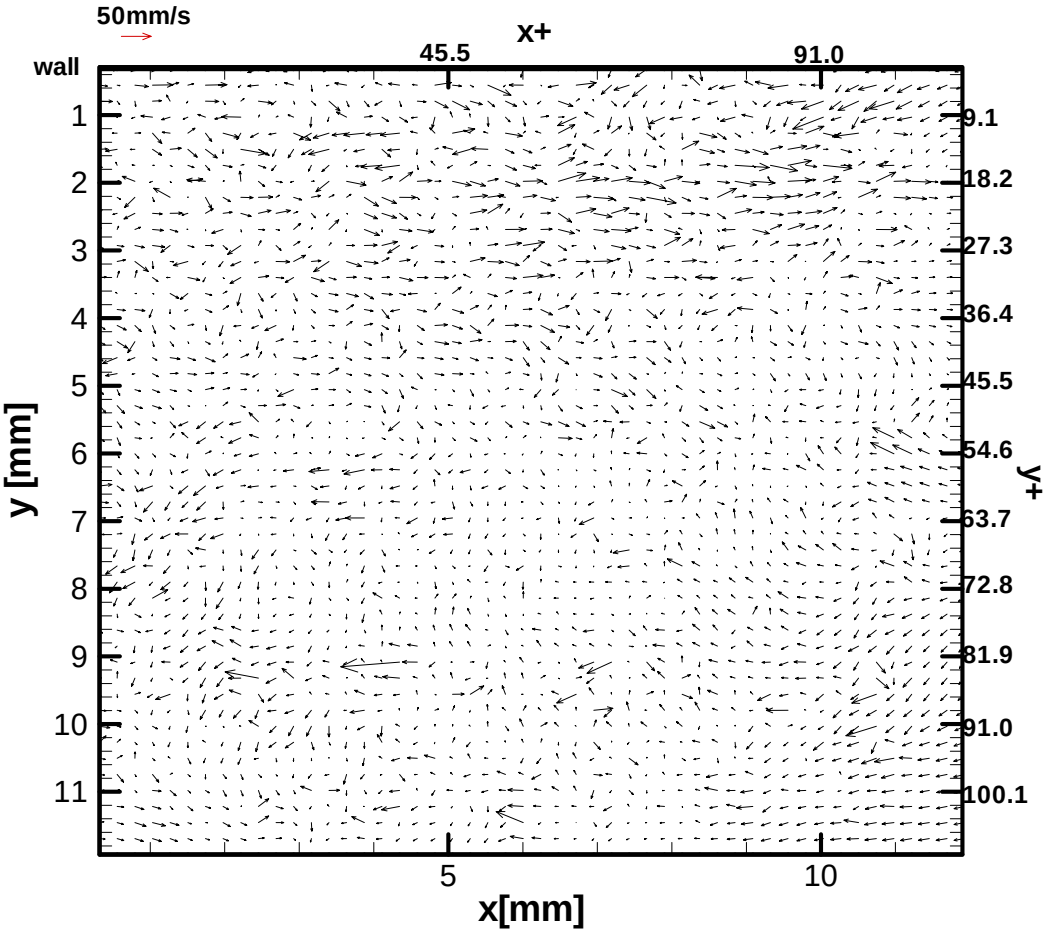

FIGURE 107. Instantaneous fluctuating velocity field for α = 4.9%, DR = 38.4%.obtained using the Reynolds decomposition.

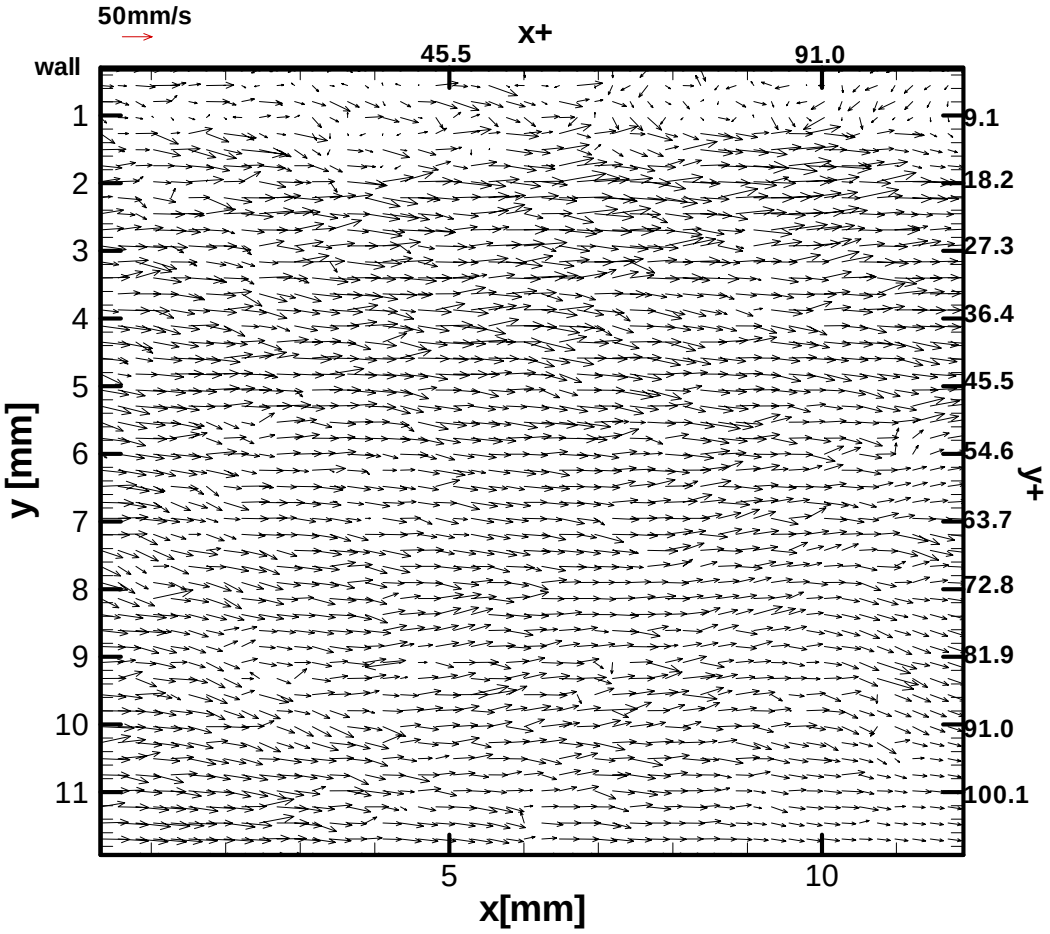

FIGURE 108. Instantaneous fluctuating velocity field for α = 4.9%, DR = 38.4%.obtained using the modified Reynolds decomposition (-0.75U).

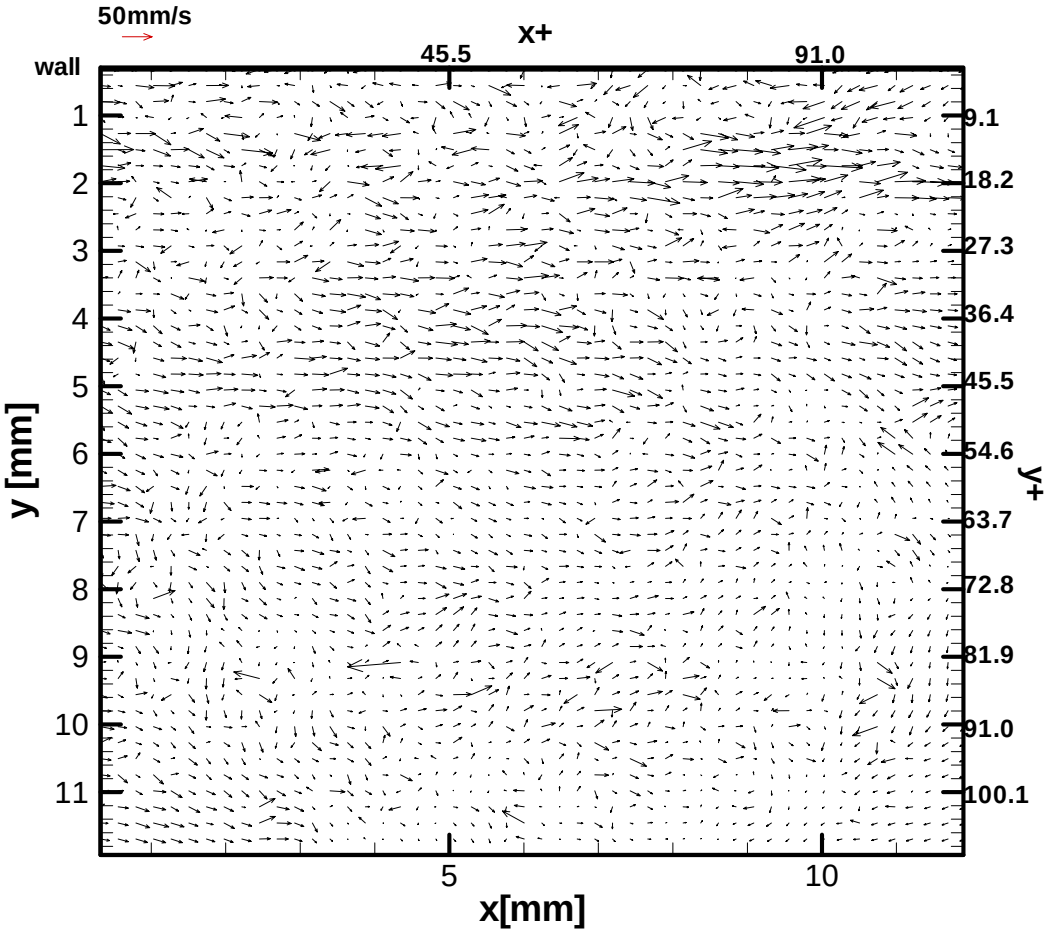

FIGURE 109. Instantaneous fluctuating velocity field for α = 4.9%, DR = 38.4%.obtained using the modified Reynolds decomposition (-0.9U).

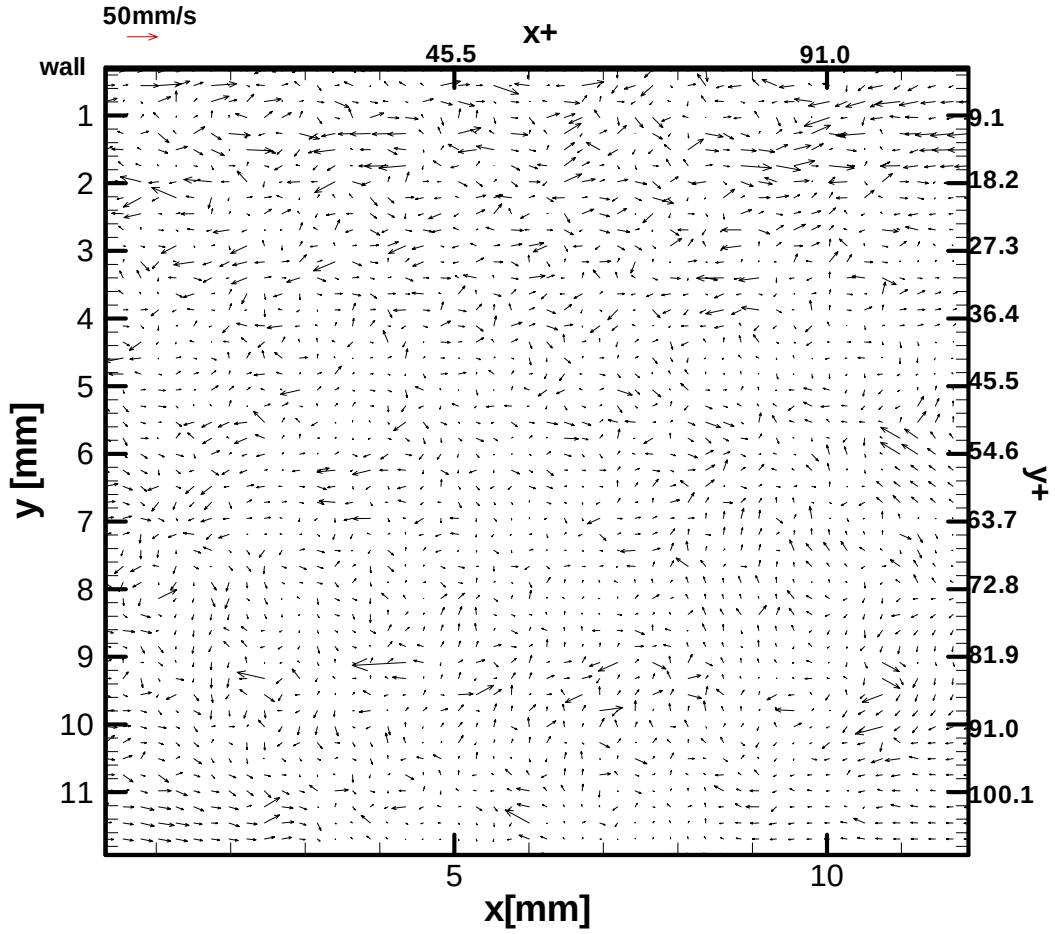

FIGURE 110. Instantaneous fluctuating velocity field for α = 4.9%, DR = 38.4% obtained using the spatial decomposition.

Vortex identification is a very important since in a boundary layer, any vortex with an orientation different from wall normal has the potential to “pump” mass and momemtum across the mean velocity gradient (Robinson 1991). The vortex strength

technique was used to identify vortices in single phase and two-phase flow. These results are shown in figures 111 and 112.

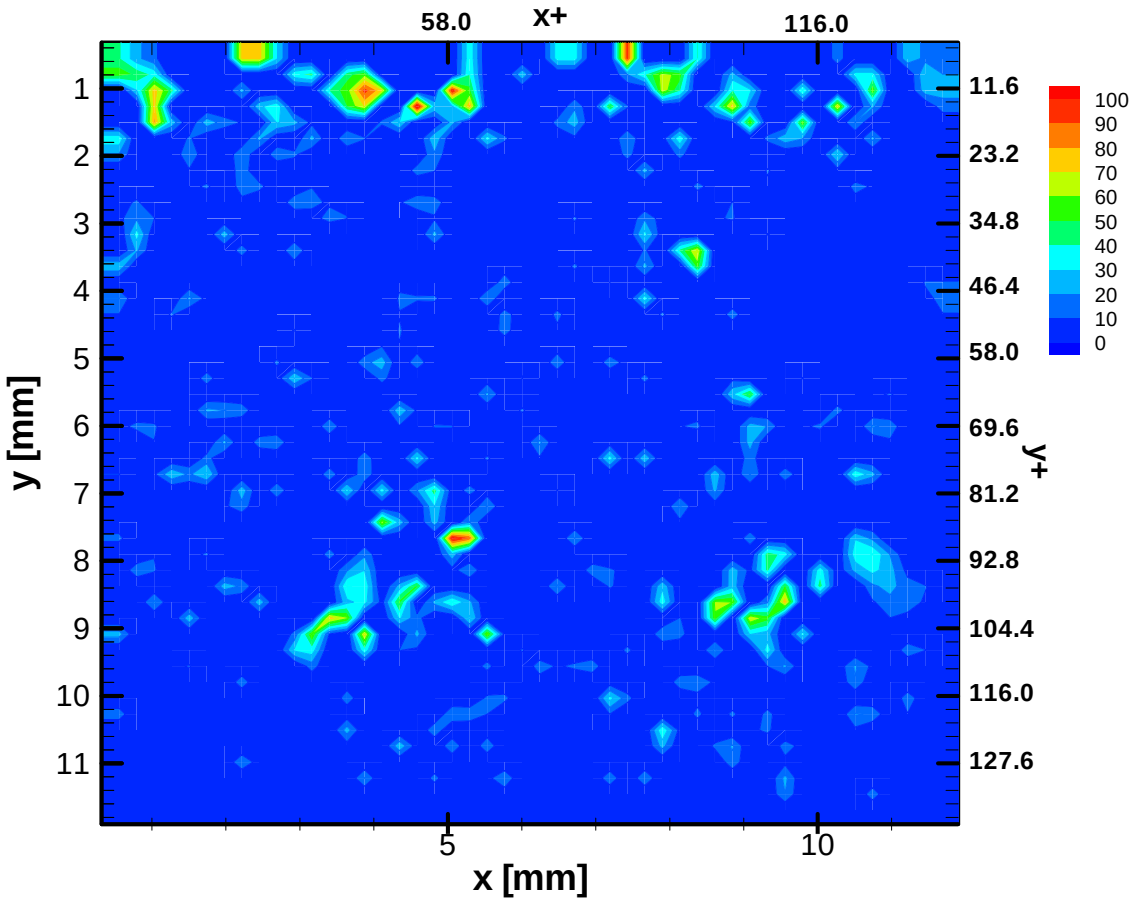

FIGURE 111. Swirling strength field for single phase flow.

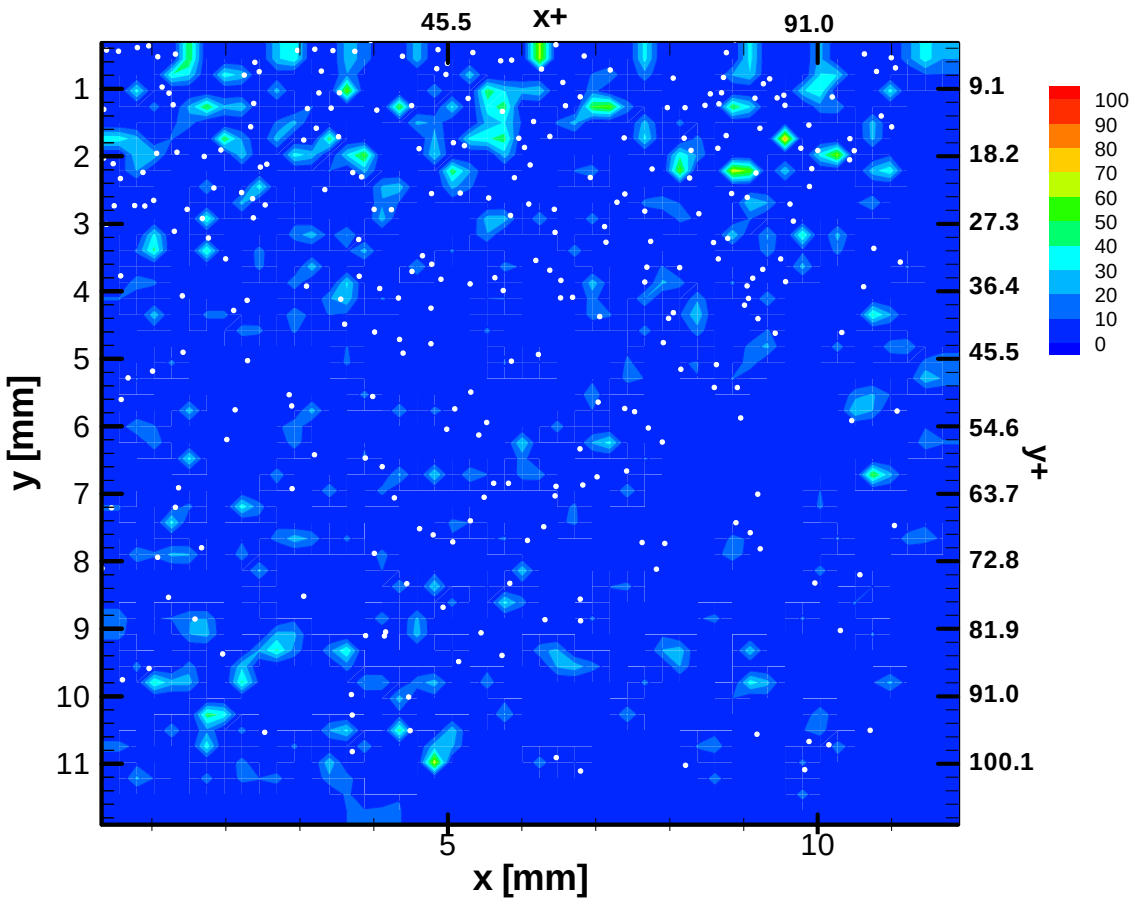

FIGURE 112. Swirling strength field for α = 4.9%, DR = 38.4%.

The presence of microbubbles (not in scale) acts as a physical barrier to reduce or destroy the swirling strength in the two-phase flow. This reinforces the idea that profound changes take place in the boundary layer once microbubbles are injected. All this information shed new light on the effects that the presence of microbobbles has in the boundary layer apart from the reduction of drag.

CHAPTER V

CONCLUSIONS

In this investigation, boundary layer modifications in a channel flow with microbubbles injection was studied using PIV measurements in an x-y plane close to the upper wall of a channel. Several changes took place in the turbulent boundary layer after the injection of microbubbles, which were observed and studied to gain a better understanding of this phenomenon.

1) The streamwise and normal non-dimensional turbulent intensities, which are normalized with the wall friction velocity increased when the values of the local void fraction increased. For the non-dimensional streamwise turbulence intensity, this effect has been observed previously in polymer and surfactant drag reduction investigations. However, for the non-dimensional normal turbulence intensity, this increase is opposite to the trend found in drag reduction by polymers and surfactants studies.

2) The Reynolds shear stresses decreased as the values of the local void fraction increased. This is due to a “decorrelation” or decoupling between the streamwise and normal fluctuating velocity components produced in the microbubbles’ presence. The fact that both non-dimensional turbulent intensities (streamwise and normal) increase with the increase of the local void fraction strengthens the notion that the decrease in the Reynolds stresses is not produced by a decrease in one or both turbulent intensities, but the decrease in the correlation between the velocity components. The decrease in the Reynolds shear stress leads to a reduction in the turbulence production.

3) A change in the shape and size of the large turbulence structures (energy containing eddies) is elucidated from the two-point correlation calculations in the x-direction (longitudinal) at different distances from the wall, y and also in the y-direction (transverse) at different x positions. Two-point correlation coefficients were also calculated in the r-direction at different inclination angles from the wall, as well as two-dimensional two-point correlation coefficients at different location within the test area. An increase in the values of the two-point correlation coefficients for the streamwise fluctuating velocity components was as the local void fraction increases. On the other hand, the two-point correlation coefficients calculated from the normal velocity component showed a decrease in value as the local void fraction increases.

4) The computation of the integral length scale in both cases gives a clear indication of changes in size and intensity of the coherent structures within the boundary layer. As the integral length scales in the longitudinal and normal direction for the streamwise velocity component increases, the length scales of the normal velocity component decrease. This again is a result of the decoupling between the two velocity components in presence of microbubbles.

5) An increase in the integral time scale for the streamwise fluctuating velocity component is also obtained using the autocorrelation function at different locations in the viewing area. This indicates a shift to lower frequencies when microbubbles are injected. However, the integral time scales of the normal fluctuating velocity component show a decrease as the value of the void fraction increases.

6) A decrease in the strain rate is observed as the local void fraction value is increased, this leads directly to a decrease in the vorticity magnitude. Microbubbles seem to disrupt zones with large strain acting as a physical barrier. This effect is observed in the instantaneous fluctuating z-vorticity fields, where groups of microbubbles seem to encircle iso-vorticity zones. The decrease in the rate of strain is also directly related to a decrease in the turbulence dissipation. However, the fact that our test zone is located in the x-y plane does not allow us to calculate all the terms in the dissipation equation.

Quadrant analysis was used to analyze the production of Q_2 (bursts) and Q_4 (sweeps) events. This tool was first implemented to analyze the measurements of the whole velocity field at the same time. A decrease in the fraction of sweeps, known for their contribution to the generation of skin friction, is observed as microbubbles are injected. When this analysis is implemented for a single point in the velocity field, which is analyzed in the time domain, a decrease in the contribution to generation of the Reynolds stresses from both, burst and sweeps is observed.

The modification of the vortical structures within the boundary layer was also analyzed using different visualization methods, the calculation of the swirling strength was effective in the localization of vortices and showed a decrease in their strength when microbubbles are present.

An important effect of the microbubbles presence within the boundary layer is the reduction of drag. This reduction might be explained by a reduction of momentum exchange at the wall. The presence of microbubbles within the boundary layer inhibits

the momentum exchange at the wall. They act as a physical barrier that disables the interaction between the zones of low velocity and the high velocity zones, absorbing energy from the fluid. The diameter of the bubbles is crucial to attain the drag reduction effect, since very small bubbles do not produce large disturbances in the flow that promote the production or enhancement of turbulence. The location or microbubbles in the boundary layer is also very important, they need to be injected in the buffer layer that is where the majority of turbulence production takes place. Measurements in the x-z plane at different distances from the wall need to be carried out to verify these hypotheses.

REFERENCES

ADRIAN, R. J. 1991 Particle-imaging techniques for experimental fluid mechanics. *Annu. Rev. Fluid Mech.* **23**, 261-304.

ADRIAN, R. J., CHRISTENSEN, K. T. & LIU, Z. –C. 2000 Analysis and interpretation of instantaneous turbulent velocity fields. *Experiments in Fluids* **29**, 275-290.

ANTONIA, R. A. 1981 Conditional sampling in turbulence measurement. *Ann. Rev. Fluid Mech.*, **13**, 131-156.

ANTONIA, R. A. & KROGSTAD, P., -Å. 2001 Turbulence structure in boundary layers over different types of surface roughness. *Fluid Dynamics Research* **28**, 139-157.

BERNARD, P. S. & WALLACE, J. M. 2002 *Turbulent Flow. Analysis, Measurement and Prediction.* John Wiley & Sons, Inc.

BOGARD, D. G. & TIEDERMAN, W. G. 1986 Burst detection with single-point velocity measurements. *J. Fluid Mech.*, **162**, 389-413.

BOGDEVICH, V. G., EVSEEV, A. R., MALYUGA, A. G. & MIGIRENKO, G. S. 1977 Gas-saturation effect on near-wall turbulence characteristics. In *Drag Reduction, Papers presented at the Second International Conference on Drag Reduction*, pp. D2-25 – D2-37, University of Cambridge, England.

BRODKAY, R. S. 1995 *The Phenomena of Fluid Motions,* Dover Publications.

CHONG, M. S., PERRY, A. E. & CANTWELL, B. J. 1990 A general classification of three-dimensional flow fields. *Phys. Fluids* **2**, 765-777.

DE ANGELIS, E., CASCIOLA, C. M. & PIVA, R. 2002 DNS of wall turbulence: dilute polymers and self sustaining mechanisms. *Computer & Fluids* **31**, 495-507.

DEAN, R. B. 1978 Reynolds number dependence of skin friction and other bulk flow variables in two-dimensional rectangular duct flow. *Trans. ASME*: *J. Fluids Engng.* **100**, 215.

DEN TOONDER, J. M. J., HULSEN, M. A., KUIKEN, G. D. C. & NIEUWSTADT, F. T. M. 1997 Drag reduction by polymer additives in a turbulent pipe flow: numerical and laboratory experiments. *J. Fluid Mech*. **337**, 193-231.

DURST, F., KIKURA, H., LEKAKIS, I., JOVANOVIĆ, J. & YE, Q. 1996 Wall shear stress determination from near-wall mean velocity data in turbulent pipe and channel flows. *Experiments in Fluids* **20**, 417-428.

FERNHOLZ, H. H., JANKE, G., SHOBER, M., WAGNER, P. M. & WARNACK, D. 1996 New developments and applications of skin-friction measuring techniques. *Meas. Sci. Technol.* **7**, 1396-1409.

FISCHER, M., JOVANOVIĆ, J. & DURST, F. 2001 Reynolds number effects in the near-wall region of turbulent channel flows. *Phys. Fluids* **13**, 1755-1767.

FONTAINE, A. A., DEUTSCH, S., BRUNGART, T. A., PETRIE, H. L. & FENSTERMACKER, M. 1999 Drag reduction by coupled systems: microbubble injection with homogeneous polymer and surfactant solutions. *Experiments in Fluids* **26**, 397-403.

FORTUNA, G. & HANRATTY, T. J. 1972 The influence of drag-reducing polymers on turbulence in the viscous sublayer. *J. Fluid Mech*. **53**, 575-586.

FOX, R. W. & McDONALD, A. T. 1998 *Introduction to Fluid Mechanics*, 5th Edn. John Wiley and Sons.

FUKAGATA, K., IWAMOTO, K. & KASAGI, N., 2002 Contribution of Reynolds stress distribution to the skin friction in wall-bounded flows. *Phys. Fluids* **14**, L73-L76.

GASLJEVIC, K. & MATTHYS, E. F. 1999 Improved quantification of the drag reduction phenomenon through turbulence reduction parameters. *J. Non-Newtonian Fluid Mech.* **84**, 123-130.

GORDON, C. M. 1975 Period between bursts at high Reynolds number. *Phys. Fluids* **18**, 141-143.

GUIN, M. M., KATO, H., YAMAGUCHI, H., MAEDA, M. & MIYANAGA, M. 1996 Reduction of skin friction by microbubbles and its relation with near-wall bubble concentration in a channel. *J. Mar. Sci. Technol*. **1**, 241-254.

GÜNTHER, A., PAPAVASSILIOU, D. V., WARHOLIC, M. D. & HANRATTY, T. J. 1998 Turbulent flow in a channel at a low Reynolds number. *Experiments in Fluids* **25**, 503-511.

GYR, A. 1977 Burst cycle and drag reduction. *Phys. Fluids* **20**, s287.

HANRATTY, T. J., CHORN, L. G. & HATZIAVRAMIDIS, D. T. 1977 Turbulent fluctuations in the viscous wall region for Newtonian and drag reducing fluids. *Phys. Fluids* **20**, s112-s119.

HASSAN, Y. A., BLANCHAT, T. K. & SEELEY, C. H. Jr. 1992 PIV flow visualization using particle tracking techniques. *Meas. Sci. Technol.* **3**, 633-642.

HWANG, D. P. 1997 A proof of concept experiment for reducing skin friction by using a micro-blowing technique. *AIAA Paper 97-0546*.

JIMENEZ, J. & PINELLI, A. 1997 Wall turbulence: how it works and how to damp it. *AIAA Paper* 97-2112.

JIMENEZ, J. & PINELLI, A. 1999 The autonomous cycle of near-wall turbulence. *J. Fluid Mech*., **389**, 335-359.

KANAI, A. & MIYATA, H. 2001 Direct numerical simulation of wall turbulent flows with microbubbles. *Int. J. Numer. Meth Fluids* **35**, 593-615.

KARNIADAKIS, G. E. & CHOI, K-S. 2003 Mechanisms on transverse motions in turbulent wall flows. *Annu. Rev. Fluid Mech*. **35**, 45-62.

KATO, H., MIYANAGA, M., HARAMOTO, Y. & GUIN, M. M. 1994 Frictional drag reduction by injecting bubbly water into turbulent boundary layer. In *FED-Vol. 190, Cavitation and Gas-Liquid Flow in Fluid Machinery and Devices* (ed. O'Hern, T. J., Kim, J. H., Morgan, W. B. & Furaya, O.), pp. 185-194 ASME, Lake Tahoe, NV.

KAWAGUCHI, Y. & FENG, Z. 2001 Turbulent spatial structure in a drag-reducing flow with surfactant additives investigated by PIV system. In *Proceedings of the Second Symposium on Smart Control of Turbulence* (ed. Ohashi, H. & Kasagi, N.), [CD-ROM], University of Tokio.

KAWAGUCHI, Y., SEGAWA, T., FENG, Z. & LI, P. 2002 Experimental study on drag-reducing channel flow with surfactant additives – spatial structure of turbulence investigated by PIV system. *Int. J. Heat and Fluid Flow* **23**, 700-709.

KAWAHARA, G., AYUKAWA, K., OCHI, J. & ONO, F. 1998 Bursting phenomena in a turbulent square-duct flor. *JSME International Journal. Series B.* **41**, 245-253.

KIM, J., MOIN, P. & MOSER, R. 1987 Turbulence statistics in fully developed channel flow at low Reynolds number. *J. Fluid Mech*., **177**, 133-166.

KIM, J. & SPALART, P. R. 1987 Scaling of bursting frequency in turbulent boundary layers at low Reynolds numbers. *Phys. Fluids* **30**, 3326-3328.

KIM, J. 2003 Control of turbulent boundary layers. *Phys. Fluids* **15**, 1093-1105.

KIM, S-Y. & CLEAVER, J. W. 1995 The persistence of drag reduction following the injection of microbubbles into a turbulent boundary layer. *International Communications in Heat and Mass Transfer* **22**, 353-357.

KITAGAWA, A., SUGIYAMA, K., ASHIHARA, M., HISHIDA, K. & KODAMA, Y. 2003 Measurement of turbulence modification by microbubbles causing frictional drag reduction. In *Proc. of ASME FEDSM'03*, [CD-ROM], Honolulu, HI.

KLINE, S. J., REYNOLDS, W.C., SCHRAUB, F. A. & RUNSTADLER, P. W. 1967 The structure of turbulent boundary layers. *J. Fluid Mech*. **30**, 741.

KODAMA, Y., KAKUGAWA, A., TAKAHASHI, T. & KAWASHIMA, H. 2000 Experimental study on microbubbles and their applicability to ships for skin friction reduction. *International Journal of Heat and Fluid Flow* **21**, 582-588.

KOZIVKI, W. & TIU, C. 1968 Anomalous wall effects and associated drag reduction in turbulent flow. *Chemical Engineering Science* **23**, 231-242.

KROGSTAD, P., -Å., ANTONIA, R. A. & BROWNE, L. W. B. 1992 Comparison between rough- and smooth-wall turbulent boundary layers. *J. Fluid Mech*., **245**, 599-617.

KROGSTAD, P-A. & KOURAKINE, A. 2000 Some effects of localized injection on the turbulence structure in a boundary layer. *Phys. Fluids* **12**, 2990-2999.

LARSON, R. G. 2003 Analysis of polymer turbulent drag reduction in flow past a flat plate. *J, Non-Newtonian Fluid Mech.* **111**, 229-250.

LATORRE, R. 1997 Ship hull drag reduction using bottom air injection. *Ocean Engng*. **24**, 161-175.

LESIEUR, M. 1990 *Turbulence in Fluids,* 2nd Edn. Kluwer Academic Publishers.

LU, S. S. & WILLMARTH, W. W. 1973 Measurements of the structure of the Reynolds stress in a turbulent boundary layer. *J. Fluid Mech*. **60**, 481-512.

LUMLEY, J. L. 1977 Drag reduction in two phase and polymer flows. *Phys. Fluids* **20**, s64-s71.

MADAVAN, N. K., MERKLE, C.L. & DEUTSCH, S. 1985 Numerical investigations into the mechanisms of microbubble drag reduction. *Journal of Fluids Engineering. Transactions of ASME* **107**, 370-377.

McCOMB, W. D. 1990 *The Physics of Fluid Turbulence*. Oxford University Press.

McCORMICK, M. E. & BHATTACHARYYA, R. 1973 Drag reduction of a submersible hull by electrolysis. *Naval Engineers Journal* **April**, 11-16.

MERKLE, C. L. & DEUTSCH, S. 1989 Microbubble drag reduction. In: *Frontiers in Experimental Fluid Mechanics Sen. Lecture Notes in Engineering* (ed. Gad-el-Hak, M.) **46**, 291-335. Springer-Verlag.

MORIGUCHI, Y. & KATO, H. 2002 Influence of microbubble diameter and distribution on frictional resistance reduction. *J. Mar. Sci. Technol*. **7**, 79-85.

PANTON, R. L. 1996 *Incompressible Flow*, 2nd. Ed. John Wiley and Sons.

PARK, Y.-S., PARK, S. –H. & SUNG H. J. 2003 Measurement of local forcing on a turbulent boundary layer using PIV. *Experiments in fluids* **34**, 697-707.

PIIRTO, M., IHALAINEN, H., ELORANTA, H. & SAARENRINNE, P. 2001 2D Spectral and turbulence length scale estimation with PIV. *Journal of Visualization* **4**, 39-49.

POPE, S. B. 2000 *Turbulent Flows*, Cambridge University Press.

RAFFEL, M., WILLERT, C. E. & KOMPENHANS, J. 1998 *Particle Image Velocimetry. A Practical Guide*, Springer.

ROBINSON, S. K. 1991 Coherent motion in the turbulent boundary layer. *Ann. Rev. Fluid Mech.* **23**, 601-639.

SCHLICHTHING, H. & GERSTEN, K. 2000 *Boundary Layer Theory*. Springer.

SREENIVASAN, K. R. 1988 A unified view of the origin and morphology of the turbulent boundary layer structure. In *Turbulence Management and Relaminarization*. (eds Liepmann H.W. and Narasimha R.), pp. 37-61. Springer-Verlag.

TARDU, S. F. 2001 Active control of near-wall turbulence by local oscillating blowing. *J. Fluid Mech*. **439**, 217-253.

TAYLOR, G. I. 1935 Statistical theory of turbulence. *Proceedings of the Royal Society of London, Series A, Mathematical and Physical Sciences* **151**, 421-444.

TAYLOR, G. I. 1938 Production and dissipation of vorticity in a turbulent fluid. *Proceedings of the Royal Society of London, Series A, Mathematical and Physical Sciences* **164**, 15-23.

TENNEKES, H. & LUMLEY, J. L. 1972 *A First Course in Turbulence.* The MIT Press.

TOMS, B. A. 1977 On the early experiments on drag reduction by polymers. *Phys. Fluids* **20**, s3-s5.

TSINOBER, A. 2001 *An Informal Introduction to Turbulence*. Kluwer Academic Publishers.

VIRK, P. S. 1975 Drag reduction fundamentals. *AIChE Journal* **21**, 625-656.

WALLACE, J. M., ECKELMANN, H. & BRODKEY, R. S. 1972 The wall region in turbulent shear flow. *J. Fluid Mech*., **54**, 39-48.

WARHOLIC, M. D. 1997 Modification of turbulent channel flow by passive and additive devices. PhD thesis, University of Illinois, Urbana-Champaign.

WARHOLIC, M. D., HEIST, D. K., KATCHER, M. & HANRATTY, T. J. 2001 A study with particle-image velocimetry of the influence of drag-reducing polymers on the structure of turbulence. *Experiments in Fluids* **31**, 474-483.

WEI, T. & WILLMARTH W. W. 1992 Modifying turbulent structure with drag-reducing polymer additives in turbulent channel flows. *J. Fluid Mech*. **245**, 619-641.

WELAFFE, F. 1997 On a self-sustaining process in shear flows. *Phys. Fluids* **9**, 883-900.

WHITE, C. M., SOMANDEPALLI, V. S. R. & MUNGAL, M. G. 2004 The turbulence structure of drag-reduced boundary layer flow. *Experiments in Fluids* **36**, 62-69.

WILLMARTH, W. W. & SHARMA, L. K. 1984 Study of turbulent structure with hot wires smaller than the viscous length. *J. Fluid Mech*. **142**, 121-149.

XU, J., MAXEY, M. R. & KARNIADAKIS, G. E. 2002 Numerical simulation of turbulent drag reduction using micro-bubbles. *J. Fluid Mech*. **468**, 271-281.

YAMAMOTO, Y., UEMURA, T. & KADOTA, S. 2002 Accelerated super-resolution PIV based on successive abandonment method. In *Proceedings of 11th International Symposium on Applications of Laser Techniques to Fluid Mechanics.* Paper 24-1 [CD-ROM], Lisbon.

ZHOU, J., ADRIAN, R. J. & BALANCHANDAR, S. 1996 Autogeneration of near-wall vertical structures in channel flow. *Phys. Fluids* **8**, 288-290.

ZHOU, J., ADRIAN, R. J., BALANCHANDAR, S. & KENDALL, T. M. 1999 Mechanisms for generating coherent packets of hairpin vortices in channel flow. *J. Fluid Mech*. **387**, 353-396.

APPENDIX A

To obtain the results presented in this work and perform basic turbulence statistics analysis on velocity fields obtained by PIV measurements, software was developed. The executable program TurbulencePIV.exe was developed following the mathematical formulation of the statistical tools discussed in this work. This computational program works on WINDOWS environment. The graphical interface of the main menu is shown in figure A-1.

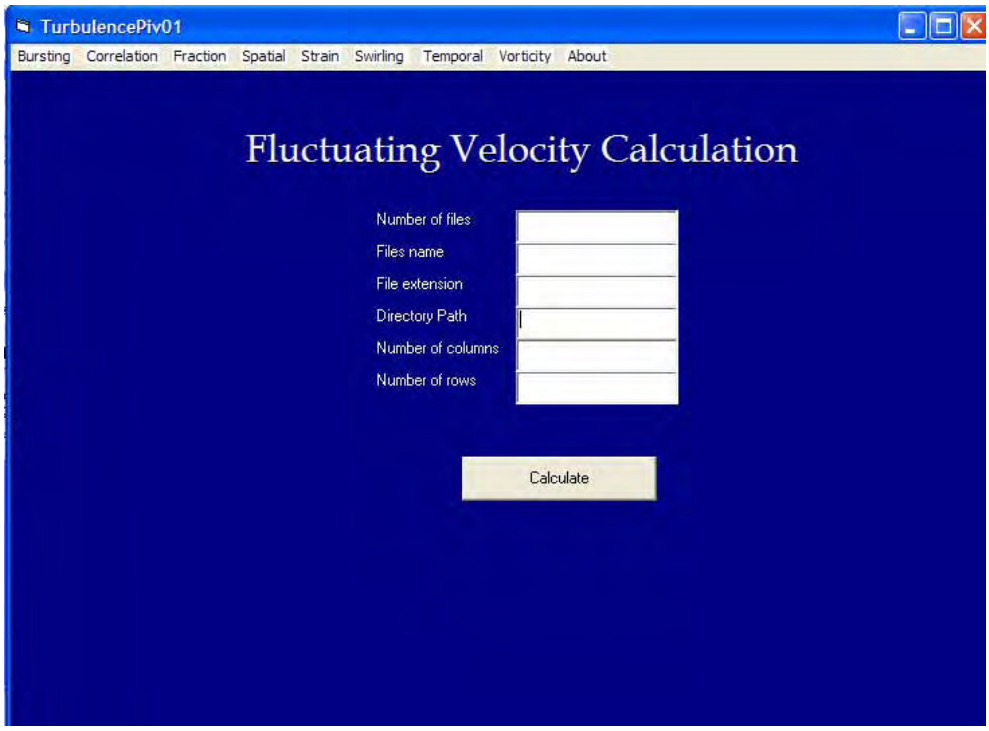

FIGURE A-1. Main menu of the software TurbulencePIV.exe.

VITA

Claudia del Carmen Gutierrez Torres was born on November 21, 1974, in Taxco, Gro., Mexico. She received a Bachelor of Science in mechanical and electrical engineering with honors and an undergraduate academic standing 1/110 from Acapulco Institute of Technology, Mexico in December 1996.

She received a Master of Science degree in mechanical engineering from the National Polytechnic Institute (Mexico) in March 2000. While attending the National Polytechnic Institute she received the Best Student in the Master of Science in the Mechanical Engineering Program Award for two consecutive years, 1998 and 1999, and her thesis work was recognized as the Best Thesis in Engineering in 2000 by the National Polytechnic Institute.

In January 2001, she joined the doctoral program in mechanical engineering at Texas A&M University under the sponsorship of the National Council of Science and Technology of Mexico (CONACyT).

Contact Information: Nuclear Engineering Department

Texas A&M University

College Station, TX. 77843-3133

(Dr. Yassin A. Hassan)

claudia2174@hotmail.com